

2003

Faculteit Wetenschappen

**Combined quantitative NMR imaging and relaxometry
on polymer materials: a fundamental study of rubbers
and water uptake in polyamide 46**

Proefschrift voorgelegd tot het behalen van de graad van
Doctor in de Wetenschappen, richting Scheikunde,
te verdedigen door

Anne POLLARIS

Promotoren : Prof. Dr. J. Gelan
Prof. Dr. P. Adriaensens

Voorzitter:

Prof. Dr. F. Dumortier (Vice-rector LUC)

Promotoren:

Prof. Dr. J. Gelan (LUC)

Prof. Dr. P. Adriaensens (LUC)

Leden van de jury:

Prof. Dr. R. Carleer (LUC)

Prof. Dr. F. De Schryver (KUL)

Prof. Dr. F. Du Prez (RUG)

Dr. M. Kelchtermans (ExxonMobil Research)

Dr. V. Litvinov (DSM Research)

Prof. Dr. J. Put (LUC, DSM Research)

Prof. Dr. D. Vanderzande (LUC)

Voorwoord

In tegenstelling tot wat de voorpagina doet vermoeden is dit doctoraatswerk zeker geen 'one-man job' geweest, maar eerder het resultaat van de gezamenlijke inzet van een groot aantal personen. Daarom zou ik dus eerst een aantal mensen willen bedanken die bewust (of onbewust) hun steentje (of heel rotsblok) hebben bijgedragen tot dit onderzoekswerk en deze thesis hebben gemaakt tot wat ze uiteindelijk geworden is.

Tijdens de oefeningen van spectroscopie in de tweede kandidatuur scheikunde, zei ooit een prof tegen me: "Jij wordt later spectroscopist!". Wie had toen kunnen denken dat ik tien jaar later mijn doctoraatsonderzoek zou afronden bij, jawel, diezelfde prof. Laat het dan wel geen zuivere spectroscopie geworden zijn, met MRI zit ik toch een beetje in de buurt. Prof. Dr. Jan Gelan, bedankt voor de mogelijkheid om te kunnen doctoreren aan het LUC en voor de blijvende steun, motivatie en interesse die je steeds hebt getoond tijdens dit hele onderzoekswerk.

Prof. Dr. Peter Adriaensens, bedankt voor je onvermoeibare gedrevenheid om me te laten kennismaken met de wondere wereld van NMR. Geen inspanning was je teveel om steeds weer op zoek te gaan naar een oplossing wanneer er een nieuw probleem de kop opstak en je kritische geest heeft zeker een positieve inbreng gehad in mijn doctoraatswerk.

Prof. Dr. Dirk Vanderzande heeft me, nadat ik een jaartje elders gewerkt had, toch kunnen overtuigen om te beginnen met een doctoraat aan het LUC. Dirk, ik heb er nog geen minuut spijt van gehad en bedankt voor alle steun. Ook de uitgebreide praktische kennis van Prof. Dr. Robert Carleer heeft ons dikwijls verder geholpen. Bedankt!

De samenwerking met de industrie heb ik altijd als zeer positief ervaren. Dr. Mauritz Kelchtermans van ExxonMobil Research heeft zeker een belangrijke bijdrage geleverd aan dit werk. Bedankt voor de boeiende en leerrijke samenwerking, je interesse in dit werk, het aanbrengen van de geschikte materialen en de talrijke wetenschappelijke discussies. I would also like to thank Dr. J. White for his support in this work and Dr. J. Dunsmuir for the XRMT measurements.

Ook de bijdrage van een enthousiaste groep mensen van DSM Research mag niet onderschat worden. Dr. Victor Litvinov, thank you very much for your support and enthusiastic interest in this work, the NMR measurements on the PA46 copolymers and the critical scientific discussions which have lead to nice results. Dr. Ruud Rulkens en Dr. Johan Tijssen zou ik willen bedanken voor het ter beschikking stellen van de materialen en hun gedrevenheid en hulp bij het zoeken naar oplossingen i.v.m. de polyamide problematiek.

Op onze twee 'handige Harry's', Koen en Jos, kon ik steeds een beroep doen als er eens iets aan de NMR haperde. Een aangepaste stretching device maken of zelfs een kapotte probe repareren is voor Jos geen probleem. Voor het oplossen van technische mankementen stond Koen steeds klaar. Bedankt allebei! Ook dank aan Christel, het SBG secretariaat en de mensen van didactiek voor allerhande (administratieve) ondersteuning en aan de ploeg van FTO, Hilde Pellaers en Jan D'Haen voor het uitvoeren van een aantal analyses.

Tijdens mijn doctoraat mocht ik deel uitmaken van een heel toffe onderzoeksgroep. Naast wetenschappelijke discussies kwamen er ook vaak andere onderwerpen ter sprake en was het er altijd fijn vertoeven. Het voordeel van 7 jaar doctoreren is dat je heel veel boeiende mensen leert kennen. Het nadeel is echter dat ik in de volgende opsomming dan ook niemand mag vergeten. Het NMR-team: Monique, Liesbet, Ben, Ingrid, Carla, Robby, Hilde, Roel, Henk V. en Maurice. Het 'oude' en 'nieuwe' synthese-team: Wim, Anne, Mik, Harald, Raf, Henk H., Miro, Laurence, Albert, Margreet, Dirk, Lieve, Veerle, Iris, Els, Stijn, Joachim, Anja, Iwona, Filip, Pawel, Wojcièch, Kristof, Lien, Ine, Sofie, Pierre-Henry en Huguette. Ook de groep van anorganische scheikunde en FTO zorgde steeds voor een aangename babbel tijdens de koffiepauzes. Olga en Elsy, bij deze zijn jullie eindelijk eens expliciet vermeld. Dank je wel allemaal voor de hulp en de bijzonder aangename sfeer. Het heeft me altijd enorm deugd gedaan.

Ma en pa, bedankt voor de kans die jullie me geboden hebben om te kunnen studeren en jullie steun en geloof in mijn doctoraat. Eveneens een welgemeend dankjewel voor mijn zussen en broer, mijn schoonfamilie en vrienden voor hun interesse in mijn werk. Ook al hebben jullie nooit helemaal begrepen waar ik nu eigenlijk mee bezig was ...

Tot slot zou ik nog de twee 'mannen' in mijn leven willen bedanken. Eric, bedankt voor je begrip en onvermoeibare steun die je me de voorbije jaren steeds hebt geboden. Zonder jou had ik deze klus nooit kunnen klaren. En Jarne ... gewoon om Jarne te zijn ...

Content

CHAPTER 1: GENERAL INTRODUCTION	1
1.1. MRI OF MATERIALS: A NEW WAY OF SEEING	1
1.2. MEDICAL AND BIOMEDICAL MRI APPLICATIONS	3
1.3. AIM AND OUTLINE OF THE THESIS	4
1.4. REFERENCES	5
CHAPTER 2: PRINCIPLES OF NMR AND MAGNETIC RESONANCE IMAGING (MRI)	7
2.1. INTRODUCTION	7
2.2. BASIC PRINCIPLES OF NMR	8
2.2.1. <i>Tissue magnetization</i>	8
2.2.2. <i>Creating an NMR signal</i>	10
2.2.3. <i>Relaxation processes</i>	10
2.2.3.1. T_1 : the spin-lattice relaxation time	11
2.2.3.2. T_2 : the spin-spin relaxation time	11
2.2.3.3. Contrast	14
2.2.3.4. Some theoretical background of relaxation: dipole-dipole interaction	17
2.3. MRI IMAGE GENERATION	19
2.3.1. <i>Slice selection</i>	19
2.3.2. <i>Phase and frequency encoding</i>	21
2.3.3. <i>Pulse sequences</i>	22
2.3.3.1. Hahn spin-echo pulse sequence	22
2.3.3.2. Multi-slice imaging	23
2.3.3.3. Chemical shift selective imaging	24
2.4. SOLID STATE NMR RELAXOMETRY	25
2.4.1. <i>High resolution ^{13}C CP/MAS solid state relaxometry</i>	25
2.4.2. <i>^1H wideline NMR</i>	25
2.5. REFERENCES	27

**CHAPTER 3: CRITICAL ANALYSIS OF NETWORK DEFECTS IN
CROSS-LINKED POLYISOBUTYLENE-BASED ELASTOMERS
(PIB ELASTOMERS) BY USING NMR IMAGING 31**

3.1. INTRODUCTION	31
3.1.1. <i>From natural rubber to the first synthetic elastomers</i>	31
3.1.2. <i>EXXPRO: A new generation of an polyisobutylene-based elastomer</i>	33
3.1.3. <i>Magnetic resonance imaging (MRI): a powerful technique to study elastomers</i>	34
3.1.4. <i>Aim and outline of this chapter</i>	38
3.2. OPTIMIZATION OF THE MRI PARAMETERS	41
3.2.1. <i>Introduction</i>	41
3.2.2. <i>Determination of the spin-spin T_2 relaxation decay time for cured unfilled PIB elastomers</i>	41
3.2.3. <i>1H spectra of swollen PIB elastomers</i>	42
3.2.4. <i>MRI images of swollen PIB elastomers</i>	44
3.2.5. <i>Conclusion</i>	46
3.3. INFLUENCE OF THE NATURE OF THE CURING AGENT ON THE NETWORK TOPOLOGY	47
3.4. MRI STUDY OF UNFILLED 1,6-HEXAMETHYLENE-DIAMINE CURED PIB ELASTOMERS WITH A DIFFERENT CROSS-LINK DENSITY	49
3.4.1. <i>Study of the cross-link density of elastomers by means of MRI rubber images</i>	49
3.4.1.1. <i>Introduction</i>	49
3.4.1.2. <i>Determination of the number-average molecular weight between the effective cross-links ($M_{n,eff}$) by using the Flory-Rehner equation</i>	49
3.4.1.3. <i>Determination of the volume-averaged T_2 relaxation times for unfilled 1,6-hexa- methylenediamine cured PIB elastomers with a different cross-link density</i>	52
3.4.1.4. <i>Image analysis: determination of the local T_2 relaxation times and correlation with the local cross-link density</i>	54
3.4.1.5. <i>Conclusion</i>	62
3.4.2. <i>MRI study of the diffusion of cyclohexane in unfilled 1,6-hexamethylene- diamine cured PIB elastomers with different cross-link density</i>	63
3.4.2.1. <i>Introduction</i>	63
3.4.2.2. <i>Determination of the diffusion kinetics by means of MRI and its correlation with the cross-link density for PIB elastomers</i>	65

3.4.2.3. Conclusion.....	71
3.4.3. <i>Conclusion and summary</i>	71
3.5. MRI STUDY OF A PIB-PMS/POLYBUTADIENE BLEND	73
3.5.1. <i>Introduction</i>	73
3.5.2. <i>MRI images of a swollen PIB/polybutadiene blend</i>	73
3.5.3. <i>Conclusion</i>	75
3.6. DEMONSTRATION AND ASSIGNMENT OF VOIDS IN CARBON-BLACK FILLED PIB ELASTOMERS.....	76
3.6.1. <i>Introduction</i>	76
3.6.2. <i>Solvent images of PIB elastomers</i>	76
3.6.2.1. Swelling and reswelling experiments of a carbon-black filled PIB elastomer.....	76
3.6.2.2. Solvent MRI images recorded with a short echo time and at a higher temperature	78
3.6.2.3. Three-dimensional reconstruction.....	79
3.6.3. <i>MRI images of unswollen PIB elastomers</i>	81
3.6.3.1. Comparison of MRI images of a PIB elastomer before and after swelling.....	81
3.6.3.2. MRI images of a native rubber at different stages of the production process	83
3.6.4. <i>Solid state NMR relaxometry study of PIB elastomers</i>	84
3.6.4.1. Introduction.....	84
3.6.4.2. High resolution ¹³ C CP/MAS solid state NMR relaxation time study.....	86
3.6.4.3. ¹ H wideline solid state NMR relaxation time study	88
3.6.4.4. Conclusions	91
3.6.5. <i>Combination of MRI, optical microscopy, SEM and XRMT experiments</i>	91
3.6.6. <i>Conclusions</i>	97
3.7. MRI STUDY OF COMMERCIAL CARBON-BLACK FILLED PIB ELASTOMERS WITH A DIFFERENT NUMBER OF VOIDS	99
3.7.1. <i>Introduction</i>	99
3.7.2. <i>Correlation of the mechanical properties of PIB elastomers with the number of voids: a statistical approach</i>	99
3.7.2.1. Introduction.....	99
3.7.2.2. Comparison of commercial carbon-black filled PIB elastomers with different mechanical performances	100
3.7.2.3. Solvent MRI images	101
3.7.2.4. Statistical image analysis.....	102
3.7.2.5. Conclusion.....	106

3.7.3.	<i>Determination of the volume-averaged relaxation times for filled PIB elastomers with different number of voids</i>	106
3.7.4.	<i>Determination of the diffusion parameters n and D for the diffusion of cyclohexane in filled PIB elastomers with different number of voids</i>	108
3.7.5.	<i>Stress-strain experiments on commercial carbon-black filled PIB elastomers with different number of voids: an MRI study</i>	111
3.7.5.1.	Introduction.....	111
3.7.5.2.	Introduction of stress-heat cycles	111
3.7.5.3.	MRI images of a solvent-swollen 'void-rich' PIB elastomer as a function of stress-heat cycles	113
3.7.5.4.	MRI images of a solvent-swollen 'void-poor' PIB elastomer as a function of stress-heat cycles	115
3.7.5.5.	Conclusion.....	116
3.8.	GENERAL CONCLUSIONS AND SUMMARY	117
3.9.	EXPERIMENTAL PART	118
3.9.1.	<i>Materials</i>	118
3.9.2.	<i>NMR imaging</i>	118
3.9.3.	<i>Solid state NMR relaxometry</i>	120
3.9.3.	<i>Scanning electron microscopy</i>	120
3.10.	REFERENCES	121

CHAPTER 4: NMR/MRI STUDY OF THE WATER INGRESS

	INTO POLYAMIDE 46 PLATES	131
4.1.	INTRODUCTION	131
4.1.1.	<i>Nylon: a new synthetic fiber</i>	131
4.1.2.	<i>Polyamide 46</i>	134
4.1.3.	<i>Water absorption by polyamides</i>	135
4.1.4.	<i>Aim and outline of this chapter</i>	137
4.2.	A GRAVIMETRIC STUDY OF THE WATER INGRESS INTO PA46 PLATES	139
4.2.1.	<i>Introduction</i>	139
4.2.2.	<i>Gravimetric study of the water ingress into native PA46 plates</i>	140
4.2.3.	<i>Gravimetric study of the water ingress into annealed PA46 plates</i>	142
4.2.4.	<i>Conclusion</i>	143
4.3.	QUANTITATIVE MRI AND NMR STUDY OF THE WATER UPTAKE BY PA46 PLATES	144
4.3.1.	<i>Introduction</i>	144

4.3.2.	<i>Determination of the state of water in swollen PA46 plates</i>	144
4.3.2.1.	Measurement of the volume-averaged ^1H T_2 relaxation times of the absorbed water molecules in saturated PA46 plates.....	144
4.3.2.2.	Quantitative determination of the amount of water in saturated PA46 plates ..	146
4.3.2.3.	Volume-averaged solid state deuterium NMR relaxation experiments	147
4.3.2.4.	Conclusions	150
4.3.3.	<i>Explanation of the horn shaped MRI intensity projection</i>	150
4.3.3.1.	MRI morphology of saturated PA46 plates	150
4.3.3.2.	A spatially resolved MRI relaxation analysis of saturated PA46 plates.....	152
4.3.3.3.	^1H wideline solid state relaxation time study of different locations of a dry PA46 plate	155
4.3.3.4.	Gravimetric and differential scanning calorimetry experiments.....	157
4.3.3.5.	Intensity calibrated MRI images and projections.....	158
4.3.4.	<i>Proposed model to explain the unexpected high amount of water sorption by PA46 and confirmation by density measurements</i>	160
4.3.5.	<i>Conclusions</i>	162
4.4.	POLYAMIDE 46-BASED COPOLYMERS: REDUCTION OF THE WATER ABSORPTION	163
4.4.1.	<i>Introduction</i>	163
4.4.2.	<i>The PA46-co-PA4n copolymer samples</i>	164
4.4.3.	<i>Study of the water ingress into PA46-co-PA4n by gravimetry</i>	165
4.4.4.	<i>NMR relaxometry of the native PA46-co-PA4n copolymers</i>	168
4.4.5.	<i>Spatially resolved MRI relaxometry of the water saturated PA46-co-PA4n copolymers</i>	170
4.4.6.	<i>Discussion with regard to the different physico-chemical parameters that determine the water uptake in PA46-co-PA4n copolymers</i>	174
4.4.6.1.	Influence of the hydrophobicity and the amount of crystallinity	174
4.4.6.2.	Annealing.....	175
4.4.6.3.	Crystallization rate and temperature-time history	176
4.4.6.4.	Chain mobility of the copolymer segments in PA46-co-PA4n	177
4.4.6.5.	Dependency of the mobility of water molecules on temperature	177
4.4.7.	<i>Conclusion</i>	178
4.5.	GENERAL CONCLUSIONS.....	179
4.6.	EXPERIMENTAL PART	180
4.6.1.	<i>Materials</i>	180
4.6.2.	<i>Gravimetric analysis</i>	181

4.6.3. <i>Volume-averaged NMR relaxation experiments</i>	181
4.6.4. <i>Imaging</i>	182
4.6.5. <i>DSC</i>	185
4.6.6. <i>WAXS and density measurements</i>	185
4.7. APPENDIX.....	186
4.7.1. <i>Water absorption data (Table 4.2)</i>	186
4.7.2. <i>Deuterium NMR relaxation experiments (section 4.3.2.3.)</i>	187
4.7.3. <i>Intensity calibrated MRI projections (section 4.3.3.5.)</i>	188
4.8. REFERENCES	189
Chapter 5: Summary	195
Hoofdstuk 6: Samenvatting	201
Chapter 7: List of abbreviations	207

Chapter 1

General introduction

1.1. MRI of materials: a new way of seeing

As the demand for high-performance materials increases, so does the need for an analytical method, which can provide spatially localized information on the internal structure of the substance. This is necessary since a polymer material can be microscopically heterogeneous for example due to processing and which can influence the material properties such as strength, toughness, elasticity, ...

Magnetic resonance imaging (MRI), first proposed by Lauterbur in 1973,¹ has proven to be a superior technique to characterize the materials' interior and to obtain more information on the local molecular dynamics. It is a unique, non-destructive and non-invasive technique, which does not require the use of ionizing radiation and enables one to obtain a three-dimensional reconstruction of the studied specimen. The different chemical components in a sample can be visualized individually by applying chemical shift selective MRI. By adjusting the experimental conditions, it is possible to manipulate the image contrast and to use the different relaxation parameters to emphasize local differences in molecular chain mobility. In the modern micro-MRI, where only objects of a few centimeters are studied, a resolution of $\pm 10 \mu\text{m}$ is attainable.

Extensive reviews on methods and applications of NMR imaging of materials have already been published.² For a number of materials, the molecular chain mobility is high enough to obtain MRI images of the native material. These applications include: study of liquid foam structures by means of 3-D NMR imaging,³ investigation into polymerization processes which generally results in solidification of the sample,⁴ chemical shift selective characterization of the displacement of water and oil in porous rocks,⁵ analysis of the aging process of natural rubber,⁶ study of toughened materials under load by MRI relaxometry,⁷ ...

However, the rather short T_2 decay time of a lot of materials prevents straightforward imaging by means of the conventional MRI techniques. The molecular chain mobility can be increased by swelling the specimens in the appropriate solvent. This allows to visualize heterogeneities in the polymer matrix and to study the diffusion of organic solvents into polymers.⁸ Local variations in cross-link density can be detected by using a non-protonated solvent or by looking at the polymer material only by means of chemical shift selective MRI.⁹

Although the traditional spin-echo techniques, as used in our laboratory, already allow visualization of some solid-like materials,⁷ more rigid systems with very short T_2 decay times require special solid state MRI methods. In this case, the broad line width due to strong anisotropic interactions is the limiting factor for image sensitivity and resolution. These problems can be overcome by using special solid state MRI pulse sequences and imaging methods including: the use of oscillating field gradients,¹⁰ stray field imaging (STRAFI),¹¹ multiple pulse methods¹² and magic angle spinning (MAS) imaging.¹³ While each method has been used successfully to image rigid materials, each also has major limitations ranging from special hardware requirements to restrictions on sample size and the number of dimensions that can be spatially imaged.

On the other hand, single point imaging (SPI), suggested as a solid imaging method by Cory in 1994,¹⁴ does not require specialized hardware. It allows direct imaging of rigid solids over a considerable sample size range and it can be applied to a large series of materials including concrete, polymers, composites and microporous solids.¹⁵ Another 'relatively simple' solid state MRI method is the back-projection technique. With this method, a number of radial projections are recorded and further processed by the appropriate algorithm to reconstruct the 2-D image.¹⁶

1.2. Medical and biomedical MRI applications

Before its use as an analytical tool in materials' research, NMR imaging has also been developed as probably the most flexible and powerful diagnostic imaging technique available to clinical medicine. MRI not only provides anatomical information complementary to the information supplied by a CT scan, but also the availability of different image contrast possibilities allows discriminating more accurately between different tissues. High resolution MRI head scans have been proven to represent the structure of the brain very faithfully. Moreover, the ability to distinguish between white and gray matter so effectively can be used as an important diagnostic tool, e.g. for the detection of multiple sclerosis lesions in the brain or spinal cord.¹⁷ Further medical applications include: MR angiography, cardiac imaging, MRI of the spinal cord, localization and diagnosis of cancer diseases and the monitoring of therapy responses,¹⁸ ...

The recent discovery that MRI can be used to map changes in brain hemodynamics that correspond to mental operations, extends the traditional anatomical imaging and allows obtaining maps of human brain function with high spatial resolution. The ability to observe both the brain structures and also which structures participate in specific functions is due to a new technique called functional magnetic resonance microscopy (fMRI). Various stimuli (visual, auditive, ...) can activate different areas in the brain which are accurately mapped. This new ability to directly observe brain functions opens an array of new opportunities to advance the understanding of brain organization, as well as to reduce the possible neurosurgical risks. Depending on the applied method, image contrast in fMRI is determined either by the oxygenation state of hemoglobin (BOLD) or by changes in cerebral blood flow (CBF) and blood volume (CBV) as a result of neuronal activity in the brain.¹⁹

1.3. Aim and outline of the thesis

The aim of the research presented in this work is the use of NMR imaging and NMR relaxometry to perform a fundamental study of commercial end products. This is applied to two different classes of polymers: an analysis of (network) defects in cross-linked isobutylene-based elastomers and a study of the water uptake in polyamide 46.

A general introduction of the applications of NMR imaging in materials' science is presented in chapter 1. Also a few (bio-)medical MRI implementations are briefly described.

A short explanation of the basic principles of NMR, NMR relaxometry and MRI imaging is given in chapter 2. The MRI pulse sequences, used in this work, are explained and the main principles of high resolution ^{13}C CP/MAS and ^1H wideline relaxometry are briefly outlined.

Chapter 3 presents an extensive analysis of network defects in cross-linked polyisobutylene-based (PIB) elastomers. After determination of the optimal experimental conditions for obtaining MRI images, a detailed investigation into local variations in cross-link density and the diffusion kinetics in unfilled 1,6-hexamethylenediamine PIB elastomers is performed. Also the presence of voids in filled and unfilled PIB elastomers is demonstrated and a relationship between the presence of voids and the mechanical performance of the commercial carbon-black filled material is determined. The last part of chapter 3 presents an MRI study of the commercial PIB elastomers under load.

Chapter 4 deals with a study of the water uptake in polyamide 46 (PA46). After a gravimetric study, more information on the ingress and distribution of the absorbed water in the PA46 matrix is obtained through MRI images and NMR and MRI relaxometry. A comparable study is performed on a set of new PA46-co-PA4n copolymers, which show a reduced water uptake compared with PA46.

A summary in English and Dutch is given in chapter 5 and 6, respectively. Chapter 7 presents a list of the most used abbreviations through this work.

1.4. References

1. Lauterbur, P.C. *Nature* **1973**, *242*, 190.
2. a) Komoroski, R.A. *Anal. Chem.* **1993**, *65*, 1068. b) Ritchey, W.M.; Maylish-Kogovsek, L. *Appl. Spectrosc. Rev.* **1994**, *29*, 233. c) Blümich, B.; Blümmler, P. *Macromol. Symp.* **1994**, *87*, 187. d) Gladden, L.F.; Alexander, P. *Meas. Sci. Technol.* **1996**, *7*, 423. e) Blümich, B.; Blümmler, P.; Gasper, L.; Guthausen, A.; Göbbels, V.; Laukemper-Ostendorf, Unseld, K.; Zimmer, G. *Macromol. Symp.* **1999**, *141*, 83.
3. a) Prause, B.A.; Glazier, J.A.; Gravina, S.J.; Montemagno, C.D. *J. Phys.: Condens. Matter* **1995**, *7*, L511. b) Kose, K. *J. Magn. Reson. A* **1996**, *118*, 195.
4. Günther, U.; Albert, K. *J. Magn. Reson.* **1992**, *98*, 593.
5. a) Hall, L.D.; Rajanayagam, V.; Hall, C. *J. Magn. Reson.* **1986**, *68*, 185. b) Majors, P.D.; Smith, J.L.; Kovari, F.S.; Fukushima, E. *J. Magn. Reson.* **1990**, *89*, 470.
6. a) Fülber, C.; Blümich, B.; Unseld, K.; Herrmann, V. *Kautsch. Gummi. Kunstst.* **1995**, *48*, 254. b) Kuhn, W.; Barth, P.; Denner, P.; Müller, R. *Solid State NMR* **1996**, *6*, 295. c) Knörigen, M.; Heuert, U.; Menge, H.; Schneider, H. *Angew. Makromol. Chem.* **1998**, *261/262*, 123.
7. a) Adriaensens, P.; Storme, L.; Carleer, R.; Vanderzande, D.; Gelan, J.; Litvinov, V.M.; Marissen, R. *Macromolecules* **2000**, *33*, 4836. b) Adriaensens, P.; Storme, L.; Carleer, R.; D'Haen, J.; Gelan, J.; Litvinov, V.M.; Marissen, R.; Crevecoeur, J. *Macromolecules* **2002**, *35*, 135.
8. a) Weisenberger, L.A.; Koenig, J.L. *Macromolecules* **1990**, *23*, 2445. b) Webb, A.G.; Hall, L.D. *Polymer* **1991**, *32*, 2926. c) Hyde, T.M.; Gladden, L.F.; Mackley, M.R.; Gao, P. *J. Polym. Sci. A: Polym. Chem.* **1995**, *33*, 1795. d) Ercken, M.; Adriaensens, P.; Reggers, G.; Carleer, R.; Vanderzande, D.; Gelan, J. *Macromolecules* **1996**, *29*, 5677.
9. a) Clough, R.S.; Koenig, J.L. *J. Polym. Sci. C: Polym. Lett.* **1989**, *27*, 451. b) Rana, M.A.; Koenig, J.L. *Macromolecules*, **1994**, *27*, 3727. c) Adriaensens, P.; Pollaris, A.; Vanderzande, D.; Gelan, J.; White, J.L.; Dias, A.J.; Kelchtermans, M. *Macromolecules*, **1999**, *32*, 4692.
10. a) Cottrell, S.P.; Halse, M.R.; Strange, J.H. *Meas. Sci. Technol.* **1990**, *1*, 624. b) Mallett, M.J.D.; Codd, S.L.; Halse, M.R.; Green, T.A.P.; Strange, J.H. *J. Magn. Reson. A* **1996**, *119*, 105. c) Star-Lack, J.M.; Roos, M.S.; Wong, S.T.S.; Schepkin, V.D.; Budinger, T.F. *J. Magn. Reson.* **1997**, *124*, 420.
11. McDonald, P.J. *Prog. NMR Spectrosc.* **1997**, *30*, 69.

Chapter 1

12. a) Chingas, G.C.; Miller, J.B.; Garroway, A.N. *J. Magn. Reson.* **1986**, *66*, 530. b) Miller, J.B.; Garroway, A.N. *J. Magn. Reson.* **1988**, *77*, 187. c) Cory, D.G.; Miller, J.B.; Turner, R.; Garroway, A.N. *Mol. Phys.* **1990**, *70*, 331.
13. a) Cory, D.G.; Van Os, J.W.M.; Veeman, W.S. *J. Magn. Reson.* **1988**, *76*, 543. b) Cory, D.G.; de Boer, J.C.; Veeman, W.S. *Macromolecules* **1989**, *22*, 1218.
14. Gravina, S.; Cory, D.G. *J. Magn. Reson. B* **1994**, *104*, 53.
15. a) Axelson, D.E.; Kantzas, A.; Eads, T. *Can. J. Appl. Spectrosc.* **1995**, *40*, 16. b) Prado, P.J.; Balcom, B.J.; Beyea, S.D.; Armstrong, R.L.; Bremner, T.W. *Solid State Nucl. Mag.* **1997**, *10*, 1. c) Kennedy, C.B.; Balcom, B.J.; Mastikhin, I.V. *Can. J. Chem.* **1998**, *76*, 1753. d) Balcom, B.J. in *'Spatially Resolved Magnetic Resonance'*, p75-86, edited by Blümmler, P.; Blümich, B.; Botto, R.; Fukushima, E.; Wiley-VCH, Weinheim, 1998. e) Prado, P.J.; Balcom, B.J.; Jama, M. *J. Magn. Reson.* **1999**, *137*, 59.
16. a) Zhou, X.; Lauterbur, P.C. in *'Magnetic Resonance Microscopy. Methods and Applications in Materials Science, Agriculture and Biomedicine'*, edited by Blümich, B.; Kuhn, W.; VCH Verlagsgesellschaft mbH, Weinheim, 1992. b) Quist, P.O. *J. Chem. Educ.* **1996**, *73*, 751.
17. a) Filippi, M.; Rocca, M.A.; Sormani, M.P.; Pereira, C.; Comi, G. *Magn. Reson. Imaging* **1999**, *17*, 979. b) Helms, G. *Magn. Reson. Med.* **2001**, *46*, 256.
18. a) Beuls, E.A.M.; Vandersteen, M.A.M.; Vanormelingen, L.M.; Adriaensens, P.J.; Freling, G.; Herpers, M.J.H.M.; Gelan, J. *J. Neurosurg.* **1996**, *85*, 701. b) Silva, A.C.; Kim, S.G.; Garwood, M. *Magn. Reson. Med.* **2000**, *44*, 169. c) Ogawa, S.; Ozaki, Y.; Sumi, Y.; Kyogoku, S.; Maehara, T. *Magn. Reson. Imaging* **2002**, *20*, 615. d) Cunningham, C.H.; Wright, G.A.; Wood, M.L. *Magn. Reson. Med.* **2002**, *48*, 689. e) Danet, I.A.; Semelka, R.C.; Braga, L.; Armao, D.; Woosley, J.T. *Magn. Reson. Imaging* **2003**, *21*, 95.
19. a) Dunn, J.F.; Wadghiri, Y.Z.; Meyerand, M.E. *Magn. Reson. Med.* **1999**, *41*, 850. b) Posse, S.; Kemna, L.J.; Elghahwagi, B.; Wiese, S.; Kiselev, V.G. *Magn. Reson. Med.* **2001**, *46*, 264. c) Duong, T.Q.; Yacoub, E.; Adriany, G.; Hu, X.; Ugurbil, K.; Vaughan, J.T.; Merkle, H.; Kim, S.G. *Magn. Reson. Med.* **2002**, *48*, 589. d) Windischberger, C.; Langenberger, H.; Sycha, T.; Tschernko, E.M.; Fuchsjäger-Mayerl, G.; Schmetterer, L.; Moser, E. *Magn. Reson. Imaging* **2002**, *20*, 575.

Chapter 2

Principles of NMR and magnetic resonance imaging (MRI)

2.1. Introduction

Since its introduction by Paul Lauterbur in the early 1970's,¹ nuclear magnetic resonance imaging (NMRI or MRI) has become the preferred technique for the medical diagnosis of many pathologies.² This success derives from the non-invasiveness, the use of non-ionizing radiation and from the availability of contrast features, which complement X-ray imaging. Since the mid 1980's, MRI has also been established as an important tool in materials' science. It provides non-destructive, three-dimensional information on the materials' interior and can yield information on local variations in molecular mobility (by means of the relaxation parameters) and chemical composition (chemical shift selective MRI).³ The wide range of applications includes: study of solvent uptake and distribution in materials,⁴ study of foam composites,⁵ aging⁶ and cross-link density distribution in elastomers,⁷ materials under load,⁸ polymerization reactions,⁹ ...

In this chapter, a short overview will be given about the basic principles of NMR and MRI. Also the MRI pulse sequences and solid state NMR techniques, used in this work, are briefly presented.

2.2. Basic principles of NMR

2.2.1. Tissue magnetization¹⁰

Nuclei with a spin quantum number $I \neq 0$ have a magnetic moment μ . This vector quantity expresses the strength and direction of the magnetic field surrounding the nucleus (Figure 2.1a) and is associated with the angular momentum P via:

$$\mu = \gamma P = \gamma \frac{h}{2\pi} [I(I+1)]^{1/2} \quad (2.1)$$

with γ the gyromagnetic ratio, which is specific for each kind of nucleus and h the Planck constant.

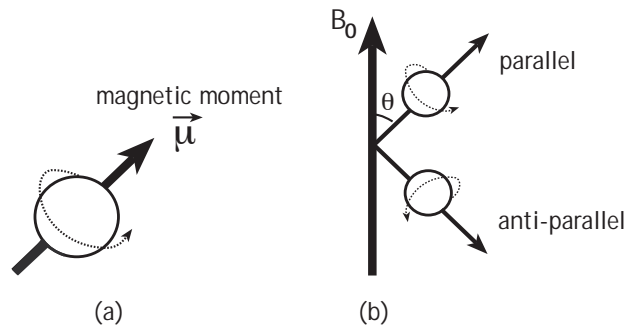


Figure 2.1: (a) Magnetic nuclei behave like microscopic magnets with a magnetic moment μ . (b) Orientations of the spins in an external magnetic field B_0 : parallel (spin-up) and anti-parallel (spin-down).

Nuclei with an odd mass number, like ^1H and ^{13}C , have a spin $I = 1/2$. If these spins are placed in an external magnetic field B_0 , they can take up two orientations as shown in Figure 2.1b: a low energy state, aligned with the applied field (spin-up or parallel) and a high energy orientation, opposed to B_0 (spin-down or anti-parallel). The difference in energy between the two orientations is given by:

$$\Delta E = \frac{h\gamma B_0}{2\pi} \quad (2.2)$$

In addition, the protons will precess around the external field vector with the Larmor frequency ω_L (Figure 2.2a), depending on the strength of the external magnetic field B_0 and the nucleus under study by:

$$\omega_L = \gamma B_0 \quad (2.3)$$

The arrangement of the proton spins over the two energy levels is given by the Boltzmann distribution:

$$\frac{N_h}{N_l} = \exp\left(-\frac{\Delta E}{kT}\right) \quad (2.4)$$

with N_h the number of nuclei in the high energy level, N_l the number of nuclei in the low energy level and k the Boltzmann constant. At equilibrium, $N_l > N_h$ and the joint alignment of the spin vectors results in a net magnetization M_0 , aligned parallel with B_0 (Figure 2.2b).

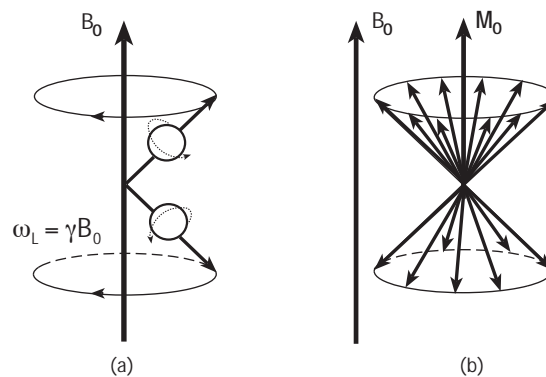


Figure 2.2: (a) The proton spins precess around B_0 with the Larmor frequency ω_L . (b) Distribution of the proton spins results in a net magnetization M_0 pointing along the axis of the external field.

2.2.2. Creating an NMR signal¹¹

To induce an NMR signal, the spins have to be flipped from the low to the high energy level by imposing a short radio frequency pulse (RF-pulse). This pulse, applied at the Larmor frequency, induces a B_1 field. If this field is oriented along the x' -direction (perpendicular to B_0 , which is positioned along the z -axis), the magnetization vector M_0 is tilted away from the z -axis over a certain angle by rotation around the B_1 field. If the strength and the duration of the RF-pulse are such that the net magnetization M_0 is rotated by an angle of 90° , the magnetization vector will become perpendicular to B_0 and will precess in the $x'y'$ -plane (transverse plane). The result of a 90° RF-pulse on the net magnetization vector M_0 is presented in Figure 2.3.

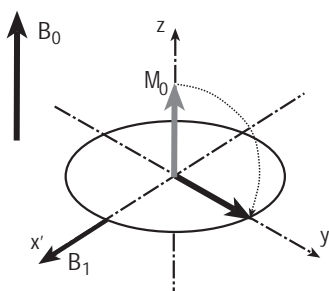


Figure 2.3: A 90° RF-pulse, applied along the x' -direction flips the magnetization vector M_0 towards the y' -axis. The $x'y'z$ -frame is the so-called rotating frame, which rotates with the Larmor frequency ω_L .

After the RF-pulse is turned off, the net magnetization will return to its original state as a result of a number of relaxation processes (see section 2.2.3.). During the detection period, the receiver coil will observe the precession in the $x'y'$ -plane or the free induction decay (FID), which is converted by a fast Fourier transformation into a frequency signal.

2.2.3. Relaxation processes¹²

During the precession after the 90° pulse, the magnetization relaxes by so-called relaxation processes, which are mainly characterized by the T_1 and T_2 time constants.

2.2.3.1. T_1 : the spin-lattice relaxation time

The restoration of the longitudinal magnetization (along the z-axis) following the 90° RF-pulse is determined by the spin-lattice or longitudinal relaxation time T_1 . Spin-lattice relaxation is associated with a change in energy of the spin system, since the absorbed energy of the RF-pulse is transferred from the spins to the direct surrounding: the lattice. The lattice represents the changing electromagnetic dipoles in the direct environment.

The recovery process is exponential as shown in Figure 2.4 and can be described by equation 2.5:

$$M_z = M_0 \left(1 - \exp\left(-t/T_1\right) \right) \quad (2.5)$$

After a period of T_1 seconds following the RF-pulse, the component of the magnetization vector along the z-axis (M_z) has recovered 63 % of its original value. In order to obtain quantitative results, a delay time of $5 \times T_1$ has to be respected between two successive pulse repetitions.

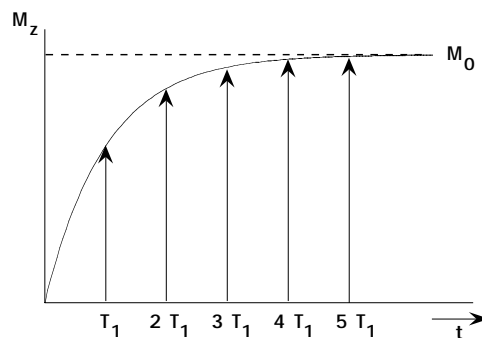


Figure 2.4: Recovery of the longitudinal magnetization M_z following a 90° pulse.

2.2.3.2. T_2 : the spin-spin relaxation time

The relaxation of the magnetization in the x'y'-plane is determined by the spin-spin or transverse decay time T_2 . The magnetization is transferred from one

spin to a neighboring spin without changing the net energy (flip-flop mechanism). If the magnetic field should be ideally homogeneous (i.e. if all nuclei experienced exactly the same field), the decay constant would be equal to T_2 . In comparison with T_1 , the T_2 relaxation time is defined as the time necessary to decay 63 % of the transverse signal intensity and the T_2 relaxation process can also be described by an exponential equation:

$$M = M_0 \exp\left(-t/T_2\right) \quad (2.6)$$

Due to T_2 relaxation, the magnetization vectors will gradually fan out or loose phase coherence as a function of time (Figure 2.5b-e), resulting in a decrease of the net transverse magnetization. Eventually, the total magnetization in the $x'y'$ -plane can become zero.

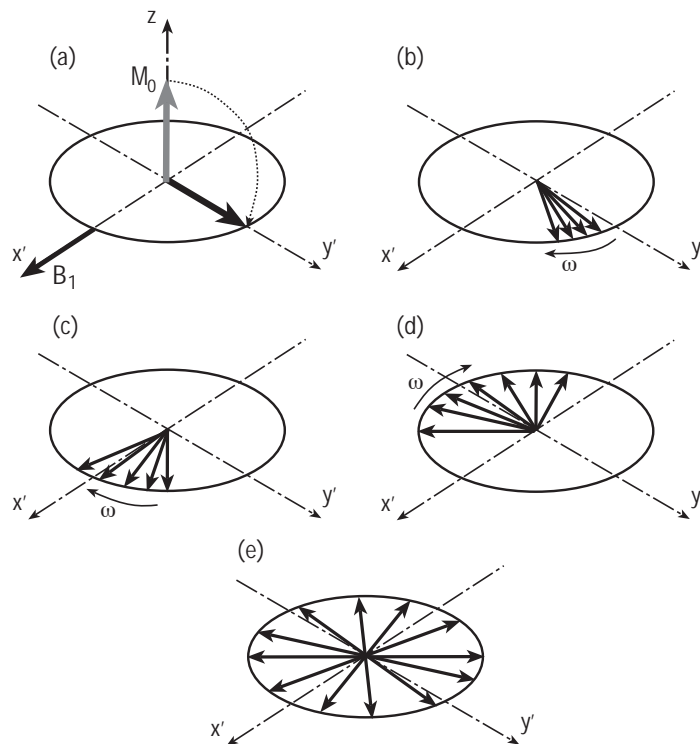


Figure 2.5: A 90° RF-pulse (a) and progressive dephasing of the precessing transverse magnetization (b-e) due to transverse relaxation.

In practice, however, the magnetic field always displays some degree of inhomogeneity. The effective time constant controlling the signal decay, T_2^* , is therefore always shorter than T_2 (Figure 2.6).

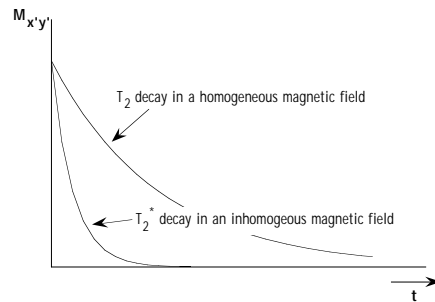


Figure 2.6: T_2 and T_2^* decay of signal intensity.

In order to eliminate the effect of the field inhomogeneities and to determine the intrinsic transverse T_2 decay time, a spin-echo pulse sequence can be used. In this experiment, a 180° RF-pulse (inversion pulse) is applied along the y' -axis, τ seconds after the initial 90° pulse (Figure 2.7). This will mirror the partially dephased magnetization vectors around the y' -axis. In this way, the fast vectors (labeled F) will catch up with the slow ones (labeled S) and finally will refocus at time $t = 2\tau$. So the 180° pulse causes the magnetization to rephase and produces a signal called a Hahn spin-echo.¹³ During the evolution time 2τ , T_2 relaxation will take place.

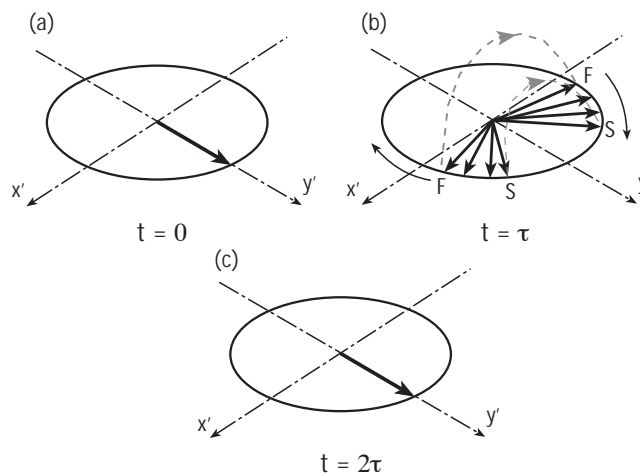


Figure 2.7: Principle of the formation of a spin-echo.

Chapter 2

The spin-echo pulse sequence is presented in Figure 2.8. T_2^* will cause a rapid decay of the signal after the initial 90° RF-pulse. Rephasing by a 180° pulse will result in an echo formation (spin-echo). The intensity of the echo signal, however, is reduced due to T_2 relaxation. The time from the 90° pulse to the detection of the spin-echo is called the echo time TE. By acquiring a series of such echo signals as a function of TE, the T_2 decay time can be determined. The time between two consecutive pulse sequence repetitions is labeled as the repetition time TR.

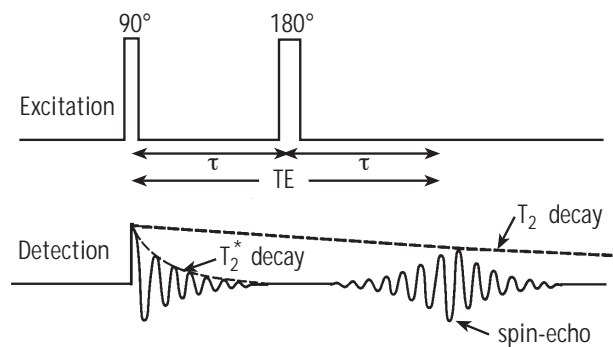


Figure 2.8: Pulse timing diagram of a spin-echo sequence: while the FID decays with a time constant T_2^* ($< T_2$), the echo amplitude decreases with the true spin-spin T_2 decay time.

2.2.3.3. Contrast

Compared with other image-forming techniques, the advantage of MRI lies in the variety of parameters that can be used to produce image contrast. Not only the proton concentration (spin density), but also the molecular relaxation behavior determined by the T_1 and T_2 relaxation times, control the intensity of the pixels in the image.¹⁴ By adjusting the experimental conditions, it is possible to obtain MRI images where the different contrast parameters are individually emphasized.

The different components in a specimen can show a different relaxation time behavior. By regulating the echo time TE, it is possible to obtain MRI images where the contrast can be mainly ascribed to differences in the T_2 decay times. TE must be chosen in such a way that the difference in transverse magnetization is maximal (Figure 2.9a) and the repetition time TR has to be long

(about $5 \times T_1$) so that the longitudinal magnetization is returned to its equilibrium value. This is also labeled as a ' T_2 -weighted' image.

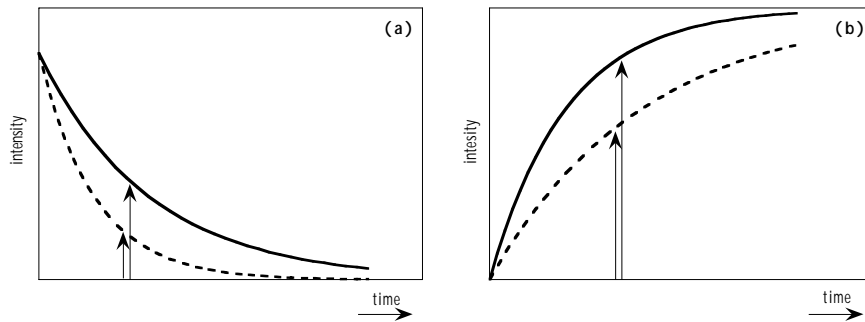


Figure 2.9: Relaxation time diagrams for two different components with indication of the optimal conditions to obtain (a) a ' T_2 -weighted' image and (b) a ' T_1 -weighted' image.

In order to obtain a spin density image where the contrast is mainly determined by local differences in proton concentration, TR must be chosen equal to $5 \times T_1$, while TE must be as short as possible to eliminate respectively the T_1 and T_2 effects as much as possible. The localized quantitative amount of proton spins can be determined by recording spin-echo MRI images (see later) as a function of TE and with a fixed repetition delay TR. The signal intensity in selected regions of interest (ROI's) as a function of TE can then be extrapolated to TE = 0 (e.g. by means of eq. 2.6) to obtain a pure spin density or concentration map.

If the repetition time TR between the successive pulse sequences is chosen in such a way that the differences in longitudinal magnetization recovery are as large as possible, a ' T_1 -weighted' MRI image can be obtained (Figure 2.9b). In these images, contrast is mainly determined by differences in the T_1 relaxation time behavior of the divers components. TE has to be as short as possible to reduce the T_2 effects as much as possible.

Another method to generate T_1 image contrast is the inversion recovery method. The equilibrium magnetization is first disturbed by a 180° RF-pulse instead of a 90° pulse (Figure 2.10). As a consequence, the magnetization is

Chapter 2

inverted along the longitudinal direction. Due to T_1 relaxation, the magnetization becomes smaller, passes through zero and starts to grow again. But since longitudinal magnetization can not be detected directly, a 90° pulse is applied after a certain evolution time to flip the longitudinal magnetization into the transverse plane.

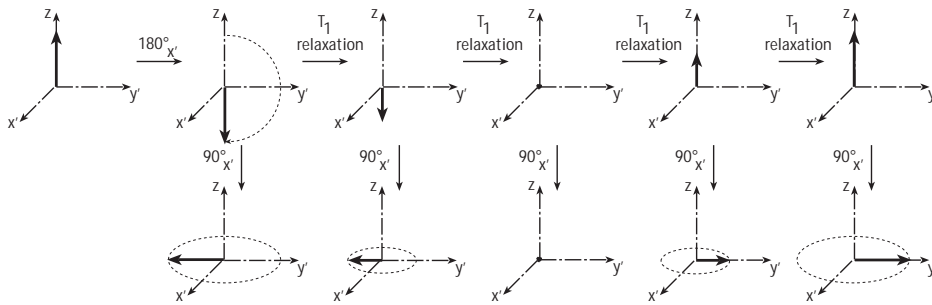


Figure 2.10: Inversion recovery experiment: evolution of the magnetization after a 180° pulse and the subsequent 90° detection pulse.

If the 90° pulse immediately follows the 180° pulse, a large negative signal is observed in the $x'y'$ -plane. In case the 90° pulse is applied when the magnetization becomes zero, no signal will be detected. At longer evolution times, a positive signal will be observed (Figure 2.11). The inversion recovery technique is very efficient to translate differences in the T_1 decay times into image contrast.¹⁵

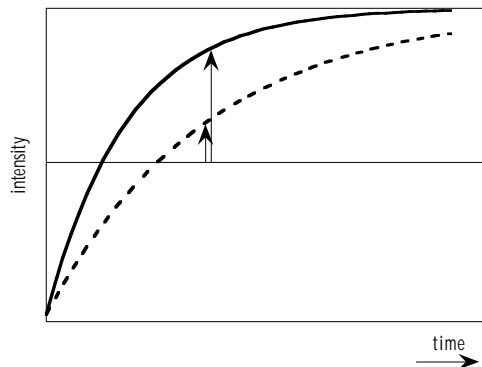


Figure 2.11: Effect of the inversion recovery evolution time on the image contrast.

2.2.3.4. Some theoretical background of relaxation: dipole-dipole interaction¹⁰

The different relaxation processes are influenced by the magnetic field, molecular motions and internuclear distances. The equations of Bloembergen, Purcell and Pound,¹⁶ present the dipolar relaxation rates for two equal spins at a distance r and with an isotropic rotational motion with correlation time τ_c :

$$\frac{1}{T_1} = \frac{3}{10} \gamma^4 \left(\frac{\hbar}{2\pi} \right)^2 r^{-6} [J(\omega_L) + 4J(2\omega_L)] \quad (2.7)$$

$$\frac{1}{T_2} = \frac{3}{20} \gamma^4 \left(\frac{\hbar}{2\pi} \right)^2 r^{-6} [3J(0) + 5J(\omega_L) + 2J(2\omega_L)] \quad (2.8)$$

with $J(\omega)$ the spectral density at the frequency ω :

$$J(\omega) = \frac{2\tau_c}{(1 + \omega^2\tau_c^2)} \quad (2.9)$$

State of aggregation, temperature, viscosity and molecular weight have an influence on the correlation time τ_c and as a consequence also on T_1 and T_2 . These equations demonstrate that molecular motions at the Larmor frequency ($J(\omega_L)$) and twice the Larmor frequency ($J(2\omega_L)$) influence both relaxation times, while the static term $J(0)$, describing the spin-spin interactions, only contributes to the transverse relaxation time.

Figure 2.12 displays the dependence of the T_1 and T_2 relaxation times on the correlation time τ_c for different strengths of the external magnetic field. Depending on the value of $\omega_L^2\tau_c^2$, different regions can be evaluated:

- a) $\omega_L^2\tau_c^2 \ll 1$: the spectral densities at ω_L are small and the relaxation processes are slow. T_1 and T_2 show a linear behavior as a function of τ_c . This region is called the 'extreme narrowing range' and is characteristic for mobile, liquid-like molecules.
- b) $\omega_L^2\tau_c^2 = 1$: the spectral densities are large at or near the Larmor frequency and the T_1 relaxation is most efficient. The minimum in the T_1

Chapter 2

curve, corresponding to $J(\omega_L) = \tau_c = 1/\omega_L$, will shift to shorter correlation times if ω_L increases (larger B_0 field).

c) $\omega_L^2 \tau_c^2 \gg 1$: the spectral densities around ω_L become small again and the T_1 relaxation becomes less efficient. The contribution to the T_2 relaxation becomes negligible as compared to the contribution of the static term $J(0)$. In this region, the T_2 relaxation is highly efficient while T_1 increases again, which is typical for immobile molecules in the solid state.

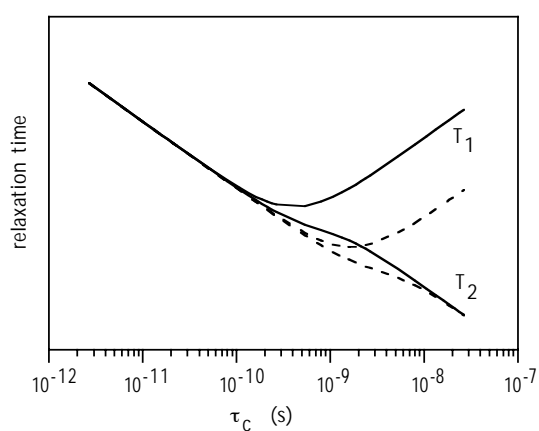


Figure 2.12: The T_1 and T_2 relaxation times as a function of the correlation time τ_c at different field strengths (— : 400 MHz, - - - : 100 MHz).

2.3. MRI image generation¹⁷

The bulk NMR techniques can be converted to ones that provide spatially dependent information by applying supplementary magnetic field gradients. Since the precession frequency of spins depends on the strength of the applied magnetic field which they 'feel', the presence of a magnetic gradient over the sample can make the spins precess at different frequencies, depending on their spatial position within the gradient field and so the magnitude of the magnetic field at that position. Thus the observed NMR signal becomes a function of spatial position and relaxation. By applying the magnetic field gradients in three orthogonal directions, the position of the proton spins can be mapped in three dimensions.¹⁸

2.3.1. Slice selection

In order to obtain images of only a selected plane through an object, a 90° RF-pulse is applied in the presence of a linear field gradient in the slice direction (in literature often referred to as ΔG_z). The only spins that will be excited are those that resonate within the bandwidth ($\Delta\omega$) of the RF-pulse. Thus only those spins, lying within the defined slice (Δz), are affected by the RF-pulse and will contribute to the MRI image. This is presented in Figure 2.13a: all the magnetization vectors in the selected slice will precess with an identical frequency, independent of their location within the slice. The position of the slice is controlled by the off-set frequency of the RF-transmitter and the orientation of the slice can be altered by applying the slice selective field gradient into another orthogonal direction.

Slice thickness is determined by two factors: the slope of the gradient and the width of the RF-pulse as demonstrated in Figure 2.14. If the frequency bandwidth of the RF-pulse, $\Delta\omega$, is kept constant and the gradient strength is varied from a low gradient (illustrated by the line B) to a steeper gradient (line A), the slice thickness is reduced from Δz_B to Δz_A (Figure 2.14a). If the gradient strength is kept constant, a thinner slice (Δz_A) is obtained by applying an RF-pulse with a smaller bandwidth $\Delta\omega$.

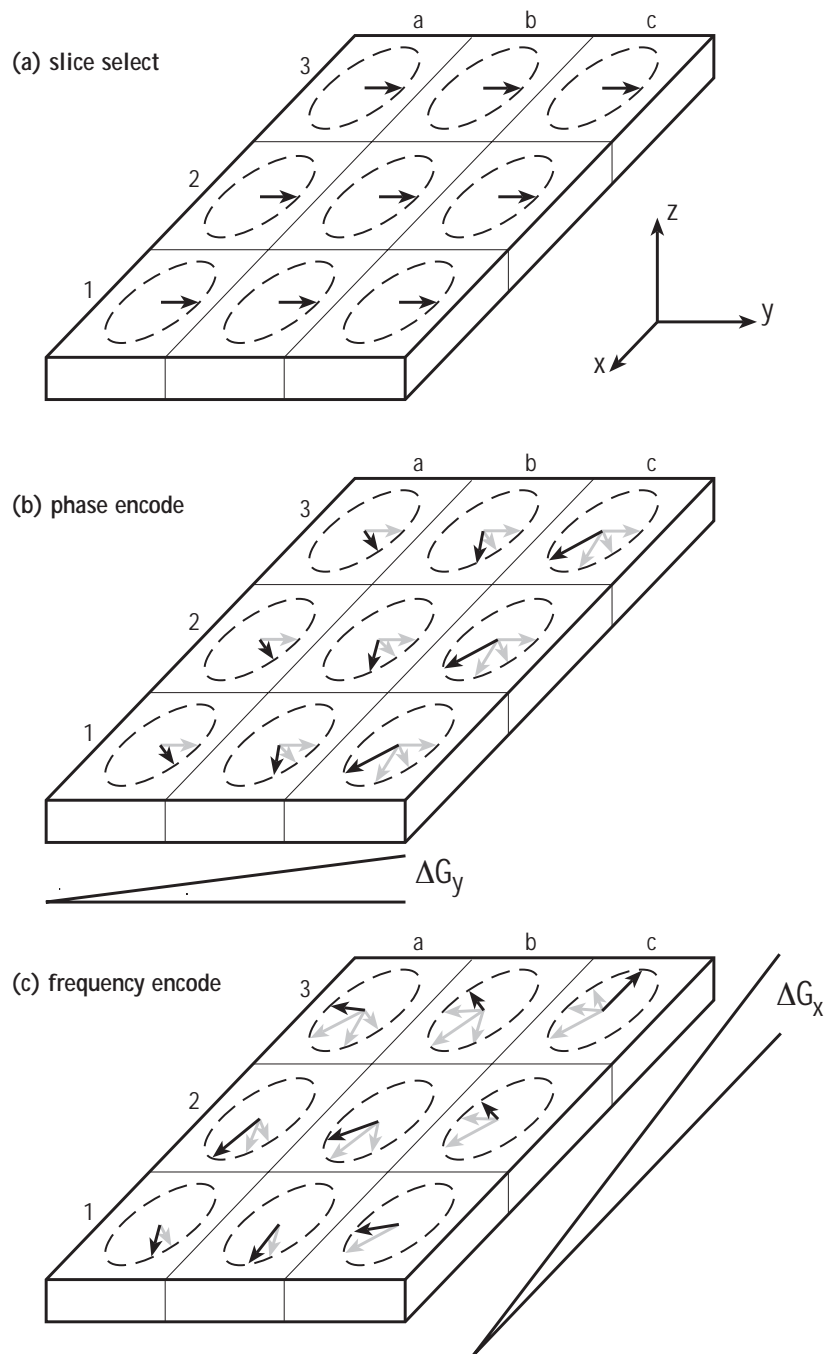


Figure 2.13: After selection of a slice (a), spatial encoding within the slice is accomplished by applying (b) a phase encoding gradient and (c) a frequency encoding gradient to the set of polarized spins in the slice.

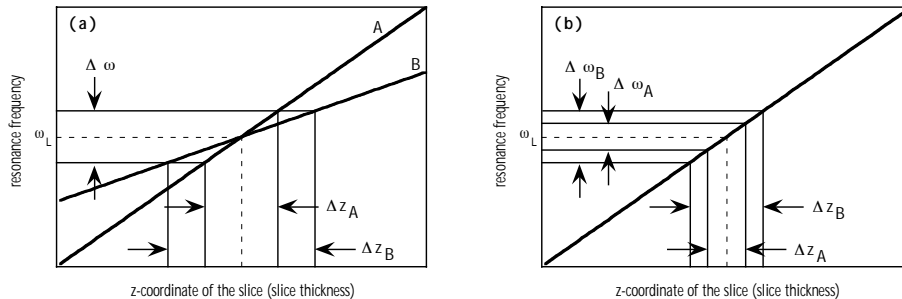


Figure 2.14: Influence of (a) variations in the strength of the magnetic field gradient and (b) bandwidth of the selective RF-pulse on the slice thickness.

2.3.2. Phase and frequency encoding

Once a slice is selected, wherein all the spins will precess with an identical frequency, spatial information within this slice can be accomplished by applying gradients in the x- and y-directions. If a second orthogonal gradient ΔG_y is implemented for a fixed time period, nuclei will precess at different frequencies, depending on their position relative to this second gradient direction. In the example in Figure 2.13b, all spins in column a have the same precession frequency and so the same phase angles after switching off the gradient. Spins in column b experience a stronger field and will evolve over a larger phase angle, etc. After this phase encoding gradient is turned off, all proton spins will again precess with their original frequency. As a consequence, the position of the proton spins in the phase direction (in our example the y-direction) can be determined based on the differences in phase angle. But there is still no differentiation in the x-direction.

In order to obtain a complete three-dimensional 'mapping' of the material, a third gradient (ΔG_x), which is orthogonal to the previous two, is turned on. The result is demonstrated in Figure 2.13c: the spins in row 1 move at a certain frequency, spins in row 2 move at a higher frequency, etc. After this frequency or read gradient is turned off, every pixel in the slice will emit an NMR signal, which allows determining the localized spin density and relaxation parameters within the selected slice.

Following a two-dimensional Fourier transformation, an MRI image is obtained in which the gray value is indicative for the signal intensity: white indicates a high intensity and black indicates a very low intensity. Resolution is, in practice, determined by the field of view (FOV) and the number of phase encoding steps. The sensitivity is determined by the number of scans.

2.3.3. Pulse sequences

2.3.3.1. Hahn spin-echo pulse sequence¹⁹

The spin-echo technique is one of the most commonly applied pulse sequences in MRI today and includes all pulse sequences, which are based on 180° refocusing pulses. These pulse sequences are insensitive towards inhomogeneities in the main magnetic field and provide images with an excellent signal to noise ratio. A typical spin-echo imaging pulse sequence is shown in Figure 2.15.^{19d}

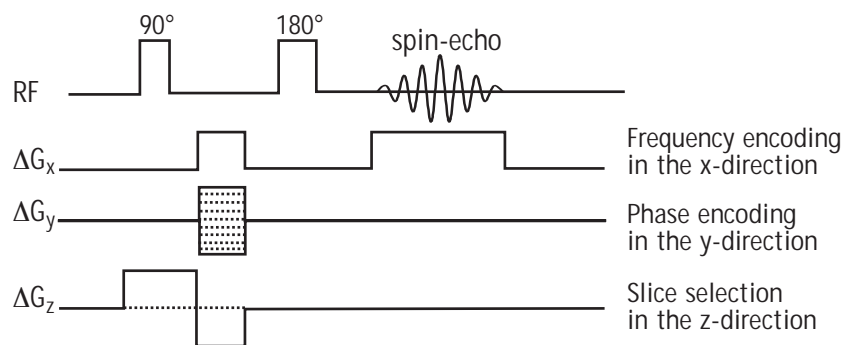


Figure 2.15: Timing diagram for a spin-echo imaging pulse sequence.

The RF-timing shows a 90° pulse, followed by a 180° pulse for the production of the spin-echo. The 90° pulse is applied in combination with the slice selection gradient ΔG_z to determine the position and thickness of the slice. Frequency encoding is in the x-direction and phase encoding is in the y-direction. The 90° pulse flips the magnetization into the transverse plane where the spins begin to dephase. After a certain time τ , the 180° pulse rotates the spins so that they begin to rephase. At a time 2τ from the 90° pulse, also known as the echo time TE, the spins refocus to form a spin-echo, but are frequency and

phase labeled. After this, the phase encoding gradient is incremented and the experiment repeated. The collection of echoes is then processed with a 2-D Fourier transformation to the desired image.

2.3.3.2. Multi-slice imaging¹⁷

For a usual spin-echo sequence, where only a single slice is being imaged, most of the time between two successive sequence repetitions is 'empty'. TE is quite short (mostly a few milliseconds) compared to TR (mostly a few seconds) and the time period between the spin-echo and the next 90° pulse is only occupied by magnetization relaxation (Figure 2.16a).

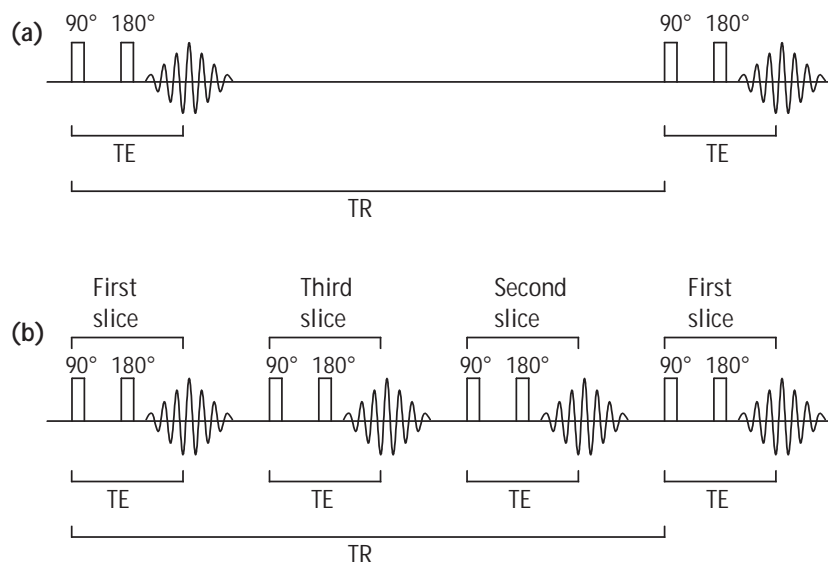


Figure 2.16: (a) Single slice and (b) multi-slice (three slices) spin-echo pulse sequence.

In order to make imaging more time-efficient, a multi-slice pulse sequence can be applied which allows recording images of several slices in the time taken to run one image in a single slice mode. The time, during which the spins of the first slice are recovering, is used to obtain data from a different slice location that is excited by a second sequence (Figure 2.16b). The multi-slice algorithm employs the 'odds and evens' rule to select the order in which the slices are

acquired. This rule is implemented to minimize the 'cross-talk' between slices as a result of pulse imperfections. The system first excites and acquires the odd slices 1, 3, 5, 7, ... skipping the even. The algorithm then instructs the system to return and collect the even slices 2, 4, 6, 8, ... Consequently, the multi-slice imaging technique is an extremely efficient way to examine a certain volume within a sample.

2.3.3.3. Chemical shift selective imaging

For some applications, it is necessary to obtain MRI images from only one specific chemical component in the sample. For example in biomedical applications, images can be recorded which show the spatial distribution of water or fat in a tissue sample. Moreover, if a chemical component displays more than one resonance signal in the proton spectrum, these chemical shift differences can cause a distortion in the image when the conventional spin-echo imaging techniques are used. By applying chemical shift selective imaging (CSSI), complementary MRI images can be acquired from the different components in a specimen, based on differences in their respective chemical shifts. However, a good separation of the spectral lines in question is a prerequisite.

The desired chemical component is selectively excited by a RF-pulse with a narrow bandwidth and only this component will then be detected. The subsequent course of the experiment is comparable with that of a normal spin-echo experiment as previously described. But in the case of CSSI, only magnetization, which is excited on the basis of the chemical shift, is further manipulated by the pulse sequence and detected by the receiver.²⁰

2.4. Solid state NMR relaxometry

In contrast with the MRI technique, which provides localized information, knowledge about the bulk molecular dynamics of polymers can be obtained by using solid state NMR relaxometry. The solid state NMR relaxometry techniques, used in this work, are briefly presented below.²¹

2.4.1. High resolution ^{13}C CP/MAS solid state relaxometry

A problem arising with solid state NMR is the rather broad line width of the spectral lines (some tens of kHz). The reasons for this line broadening can be found in the dipolar interactions of the ^{13}C nuclei with neighboring protons and in the chemical shift anisotropy. These problems are solved by applying a high-power proton decoupling and by spinning the sample physically around the 'magic angle' of 54.44° (MAS), respectively.

Besides the line broadening, solid state ^{13}C NMR also has to deal with a sensitivity problem since ^{13}C is a low abundance nucleus with a long spin-lattice relaxation time T_{1c} . The sensitivity can be improved by applying the cross polarization (CP) technique. During the CP time, a fraction of the proton magnetization is transferred to the carbon spin system, resulting in an increase of the carbon signal intensity. Moreover, the shorter proton spin-lattice relaxation times now determine the repetition time between two sequences, which also contributes to the increase of sensitivity.

The advantage of high resolution ^{13}C CP/MAS is the possibility to characterize the molecular motions of different chemical components in the sample based on the different chemical shifts.²²

2.4.2. ^1H wideline NMR

^1H wideline is also a very useful solid state NMR relaxometry technique to characterize the molecular chain mobility. No line narrowing techniques are applied, resulting in a single broad resonance signal (superposition of all proton resonances) without chemical shift information. Information on the molecular

Chapter 2

dynamics can be extracted by a multi decay time analysis. On the other hand, proton wide-line NMR has the big advantage of being very fast.

Powles introduced the solid echo pulse sequence to determine the short T_2 relaxation times for solids by means of wide-line NMR.²³ This pulse sequence circumvents the effect of the receiver dead time, allowing an accurate measurement of the short T_2 relaxation times. The Hahn echo pulse sequence²⁴ is better suited to determine the longer T_2 relaxation times since it eliminates the effect of magnetic field inhomogeneities. The longest spin-spin relaxation times are best measured by using the pulse sequence developed by Carr, Purcell, Meiboom and Gill (CPMG).²⁵

2.5. References

1. Lauterbur, P.C. *Nature* **1973**, *242*, 190.
2. a) Noth, I.; Hutter, J.J.; Meltzer, P.S.; Damiano, M.L.; Carter, L.P. *Am. J. Pediat. Hematol.* **1993**, *15*, 131. b) Smith, T.M.; Semelka, R.C.; Noone, T.C.; Balci, N.C.; Woosley, J.T. *Magn. Reson. Imaging* **1999**, *17*, 1093. c) Nelson, S.J. *Magn. Reson. Med.* **2001**, *46*, 228. d) Leonardou, P.; Semelka, R.C.; Mastropasqua, M.; Kanematsu, M.; Woosley, J.T. *Magn. Reson. Imaging* **2002**, *20*, 631. e) Steen, R.G.; Schroeder, J. *Magn. Reson. Imaging* **2003**, *21*, 9.
3. a) Mansfield, P. *J. Phys. E: Sci. Instrum.* **1988**, *21*, 18. b) Blümich, B.; Kuhn, W. 'Magnetic Resonance Microscopy. Methods and Applications in Materials Science, Agriculture and Biomedicine', VCH Verlagsgesellschaft mbH, Weinheim, 1992. c) Komoroski, R.A. *Anal. Chem.* **1993**, *65*, 1068. d) Blümmler, P.; Blümich, B. *Rubber Chem. Technol.* **1997**, *70*, 468. e) Narasimhan, B.; Snaar, J.E.M.; Bowtell, R.W.; Morgan, S.; Melia, C.D.; Peppas, N.A. *Macromolecules* **1999**, *32*, 704.
4. a) Rothwell, W.P.; Holecek, D.R.; Kershaw, J.A. *J. Polym. Sci.: Polym. Lett. Ed.* **1984**, *22*, 241. b) Weisenberger, L.A.; Koenig, J.L. *J. Polym. Sci. C: Polym. Lett.* **1989**, *27*, 55. c) Nieminen, A.O.K.; Koenig, J.L. *J. Adhesion* **1990**, *32*, 105. d) Hyde, T.M.; Gladden, L.F. *Polymer* **1998**, *39*, 811.
5. a) Jezzard, P.; Wiggins, C.J.; Carpenter, T.A.; Hall, L.D.; Jackson, P.; Clayden, N.J.; Walton, N.J. *Adv. Mater.* **1992**, *4*, 82. b) Blümich, B.; Blümmler, P. *Macromol. Symp.* **1994**, *87*, 187.
6. a) Blümmler, P.; Blümich, B. *Macromolecules* **1991**, *24*, 2183. b) Hafner, S.; Barth, P. *Magn. Reson. Imag.* **1995**, *13*, 739. c) Knörigen, M.; Heuert, U.; Schneider, H.; Heinrich, G. *J. Macromol. Sci. Phys.* **1999**, *38*, 1009.
7. a) Barth, P.; Hafner, S.; Denner, P. *Macromolecules* **1996**, *29*, 1655. b) Blümich, B.; Blümmler, P.; Gasper, L.; Guthausen, A.; Göbbels, V.; Laukemper-Ostendorf, Unseld, K.; Zimmer, G. *Macromol. Symp.* **1999**, *141*, 83. c) Prado, P.J.; Gasper, L.; Fink, G.; Blümich, B. *Appl. Magn. Reson.* **2000**, *18*, 177.
8. a) Adriaensens, P.; Storme, L.; Carleer, R.; Vanderzande, D.; Gelan, J.; Litvinov, V.M.; Marissen, R. *Macromolecules* **2000**, *33*, 4836. b) Adriaensens, P.; Storme, L.; Carleer, R.; D'Haen, J.; Gelan, J.; Litvinov, V.M.; Marissen, R.; Crevecoeur, J. *Macromolecules* **2002**, *35*, 135.

Chapter 2

9. a) Jackson, P.; Clayden, N.J.; Walton, N.J.; Carpenter, T.A.; Hall, L.D.; Jezzard, P. *Polym. Int.* **1991**, *24*, 139. b) Balcom, B.J.; Carpenter, T.A.; Hall, L.D. *Macromolecules* **1992**, *25*, 6818.
10. a) Harris, R.K. *'Nuclear Magnetic Resonance Spectroscopy. A Physicochemical View'*, Pitman Books Limited, London, 1983. b) Fyfe, C.A. *'Solid State NMR for Chemists'*, CFE Press, Ontario, Canada, 1984 .
11. Williams, D.H.; Fleming, I. *'Spectroscopic methods in organic chemistry'*, 4th edition, McGraw-Hill, London, 1989.
12. *'NMR. A perspective on imaging'*, General Electric Company, 1982.
13. a) Kuhn, W. *Angew. Chem. Int. Ed. Engl.* **1990**, *29*, 1. b) Hennig, J. *Conc. Magn. Reson.* **1991**, *3*, 125. c) Foster, M.A.; Haase, A. in *'Encyclopedia of Nuclear Magnetic Resonance'*, p4034-4041, edited by Grant, D.M.; Harris, R.K., Wiley Europe, 1996.
14. Blümich, B. *Concepts Magn. Reson.* **1998**, *10*, 19.
15. Blümich, B. *Concepts Magn. Reson.* **1999**, *11*, 71.
16. Bloembergen, N.; Purcell, E.M.; Pound, R.V. *Phys. Rev.* **1948**, *73*, 679.
17. a) Smith, S.L. *Anal. Chem.* **1985**, *57*, 595. b) Listerud, J.M.; Sinton, S.W.; Drobny, G.P. *Anal. Chem.* **1989**, *61*, 23. c) Schild, H.H. *'MRI made easy'*, Schering A.G., Berlin, 1990. d) Newhouse, J.H.; Wiener, J.I. *'Understanding MRI'*, Little Brown and Company, First Ed., Boston, 1991. e) Ercken, M. *'Kwalitatieve en kwantitatieve NMR beeldvorming bij het onderzoek van polymere materialen'*, PhD dissertation, LUC Diepenbeek, 1996.
18. Attard, J.; Hall, L.; Herrod, N.; Duce, S. *Phys. World* **1991**, *4*, 41.
19. a) Weisenberger, L.A.; Koenig, J.L. *Appl. Spectrosc.* **1989**, *43*, 1117. b) Chang, C.; Komoroski, R.A. *Macromolecules* **1989**, *22*, 600. c) Koenig, J.L. *Macromol. Symp.* **1994**, *86*, 283. d) Oh, S.J.; Koenig, J.L. *Polymer* **1999**, *40*, 4703.
20. a) Budinger, T.F.; Lauterbur, P.C. *Science* **1984**, *226*, 288. b) Ritchey, W.M.; Maylish-Kogovsek, L.; Wallner, A.S. *Appl. Spectrosc. Rev.* **1994**, *29*, 233. c) Ercken, M. *'Kwalitatieve en kwantitatieve NMR beeldvorming bij het onderzoek van polymere materialen'*, PhD dissertation, LUC Diepenbeek, 1996.
21. a) Pollers, I. *'Moleculaire structuur en dynamica van verschillende poly(vinyl formal) polymeren'*, PhD dissertation, LUC Diepenbeek, 1996. b) Jansen, C. *'NMR onderzoek naar de moleculaire structuur en dynamica van ethyleen-propyleen copolymeren'*, PhD dissertation, LUC Diepenbeek, 1998. c) Ottenbourgs, B. *'Phenol-formaldehyde resins: a*

quantitative NMR study of molecular structure and molecular dynamics, PhD dissertation, LUC Diepenbeek, 1998.

22. Silvestri, R.L.; Koenig, J.L. *Anal. Chim. Acta* **1993**, *283*, 997.
23. Powles, J.G.; Strange, J.H. *Proc. Phys. Soc.* **1963**, *82*, 6.
24. Hahn, E.L. *Phys. Rev.* **1950**, *80*, 580.
25. Meiboom, S.; Gill, D. *Rev. Sci. Instr.* **1958**, *29*, 688.

Chapter 3

Critical analysis of network defects in cross-linked polyisobutylene-based elastomers (PIB elastomers) by using NMR imaging

3.1. Introduction

3.1.1. From natural rubber to the first synthetic elastomers¹

The first 'rubber' material, also known as 'caoutchouc' (derived from the Indian word 'caa-o-chu' or 'weeping tree'), is polyisoprene recovered from the rubber tree *Hevea brasiliensis*.² Recent archaeological research showed that the ancient Meso-american people (Mayan and Aztecs) already processed this crude material to rubber balls, hollow rubber figurines and other rubbery objects of art.³ Today, this solid is referred to as natural rubber (NR), as opposed to the synthetically produced rubbers.

Crude rubbers, whether natural or synthetic, are plastic-like sticky materials that can be deformed at high temperatures and which are generally not

suitable for practical use in this state. A large improvement of the properties and, consequently, an expansion of the applicability has become possible by the (rather accidental) discovery of the vulcanization of rubber by Charles Goodyear in 1839 in the USA. He found that, when natural rubber was heated with sulfur, the undesired properties could be eliminated and the substance could be transformed into a highly elastic product.⁴ The process of vulcanization is also called curing or cross-linking.

Elastomers have the ability to deform substantially under the application of force and then snap back to almost their original shape when the force is removed. The vulcanization reaction involves the formation of interchain links, composed of two, three, or four sulfur atoms, between sites of unsaturation on adjacent chains. More improvement of the physical and mechanical properties was established by adding some vulcanizing agents such as accelerators and activators.⁵ This progress, together with the invention of the pneumatic tire (John Dunlop, 1888) and the growing car industry, resulted in a great demand for rubber and consequently an increase in the number of rubber plantations in South and Central America and Asia.

From the early 20th century, chemists have been attempting to synthesize materials whose properties duplicate or at least simulate those of natural rubber. The initial research advanced only with difficulty and the first synthetic rubber was a polymer of 2,3-dimethylbutadiene ('Methylkautschuk'), which was developed and produced in Germany during the First World War. The mechanical properties of this material were rather inferior. A breakthrough came in the Thirties with the synthesis of chloroprene in 1931 and the Buna rubbers (copolymer of butadiene with acrylonitrile (Buna-N) or with styrene (Buna-S) by using a sodium catalyst) in 1935.

But during the Second World War the import of natural rubber collapsed, which accelerated the development of synthetic rubbers. In 1952 the contribution of synthetic rubbers already exceeded 1 million ton and at present the annual consumption of synthetic rubber amounts to more than 9 million tons. About one third of the total global rubber usage is still natural rubber, produced mainly in plantations in Malaysia, Indonesia, West Africa and South and Central America. The remaining two thirds are produced synthetically by a great number of industrial companies, distributed throughout the world. Today's raw material for producing synthetic rubber is still mostly oil. More than half of the

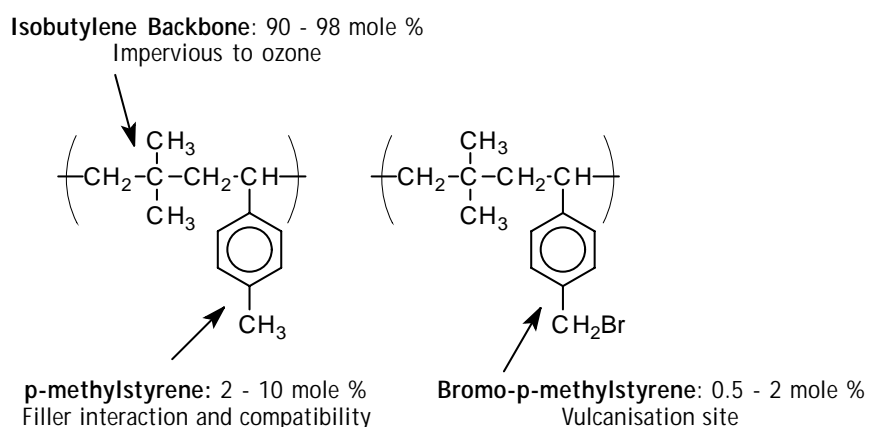
global production of natural and synthetic rubber is used in tires, and the remainder in a great variety of industrial and consumer products, ranging from motor mounts and fuel hoses over window profiles and heavy conveyor belts to household equipment and membranes for artificial kidneys.

3.1.2. EXXPRO: A new generation of an polyisobutylene-based elastomer

Polyisobutylene has been developed at the beginning of 1930 in Germany. Since this saturated rubber cannot be vulcanized, it was useless as a synthetic rubber.⁶ In the mid Thirties, Exxon Chemical (USA) succeeded in vulcanizing butyl rubber by copolymerization with a small amount of isoprene (0.6 - 2.5 mole %). During polymerization, a carbon-carbon double bond remains in the isoprene units and provides the vulcanization functionality with sulfur. One of the disadvantages of butyl rubber (or IIR: isobutylene-co-isoprene rubber) is the rather low vulcanization rate as compared with natural rubber. The IIR vulcanizates display a rather high damping (ability to absorb mechanical energy) and a very low gas and moisture permeability, making them very useful as tire inner tubes, vacuum seals and membranes. In order to improve the vulcanization behavior and the technical properties of butyl rubber, Exxon Chemical Co. developed chlorobutyl rubber. Chlorobutyl was launched at the beginning of the Sixties and displayed a faster curing rate and a better heat-resistance. Moreover, Exxon Chemical Co. introduced a bromobutyl rubber in 1980 with a much better quality than the aforementioned chlorobutyl rubber but with a higher market price. Bromobutyl's major application area is the tire industry, where it is mainly used in tubeless tire innerliners because of its low permeability to air, a fine heat-resistance and an excellent resistance to aging and to weathering due to atmospheric exposure.

In 1987, Exxon Chemical Co. developed a new generation of isobutylene elastomers: a terpolymer of isobutylene, p-methylstyrene and p-bromomethylstyrene. This poly(isobutylene-p-methylstyrene-p-bromomethylstyrene) (PIB-PMS/BrPMS) elastomer (Scheme 3.1) is brought on the market under the trade name Exxpro Specialty Elastomer in 1994. It offers promise as a second-generation butyl rubber, since the gas-barrier properties of regular butyl rubber are maintained, while the resistance to oxidative degradation is enhanced by the

saturated polymer backbone.⁷ The comonomer is paramethylstyrene, which provides improved interaction with fillers such as carbon-black and also improves the compatibility.⁸ Bromination occurs selectively on the PMS methyl group, supplying a reactive benzylic bromine functionality (about 0.5 - 2 mole %) which is the key to this elastomers' vulcanization and modification versatility.⁹



Scheme 3.1: Structure of the poly(isobutylene-p-methylstyrene-p-bromomethylstyrene) (PIB-PMS/BrPMS) elastomer.

Exxpro elastomers show an exceptional combination of low permeability and high damping (similar to butyl rubbers) with an excellent stability, heat-resistance and aging resistance (ozone/weathering), which makes them commercially valuable materials for applications in the tire industry. Blends of Exxpro Specialty Elastomers with other elastomers are used in several different sidewall applications. Sidewall tires must be designed to withstand extremes of tire services. Not only must a sidewall have an outstanding resistance to ozone cracking, but it must also resist catastrophic crack growth under severe service conditions.

3.1.3. Magnetic resonance imaging (MRI): a powerful technique to study elastomers

The mechanical properties and failure mechanisms of a cured elastomer are directly related to its physico-chemical and spatial microstructure. So the importance of obtaining a uniform cross-linked network without defects during

rubber vulcanization has considerable economic consequences. Defects (inhomogeneities) in the vulcanized network of tire sidewalls can cost manufacturers millions of dollars in lawsuits and consumers' lives.⁴ Therefore, the analysis of the structure-property relationship of tire materials is of importance, not only for the design of tires with improved functional properties, but also for the production of tires with an extended time of use. Increasing the time of use by a factor of two would reduce the annual rubber waste to about 75%.¹⁰ To achieve such goals, new techniques of analysis are explored which are more accurate, spatially specific and non-destructive, and which bear the potential of providing deeper and more detailed information, in particular on the network microstructure. A short overview of the different analysis techniques is given in the next part, combined with a more detailed overview of the widely dispersed applications of magnetic resonance imaging with respect to the study of elastomers.

Most techniques, available to study the spatial microstructure of elastomers, require sectioning the sample and analyzing the resulting slices by techniques such as scanning electron microscopy (SEM),¹¹ transmission electron microscopy (TEM),¹² infrared spectroscopy (IR),¹³ and electron spectroscopy for chemical analysis (ESCA). Dias et al.¹⁴ reported the use of time-of-flight secondary mass spectroscopy (TOF-SIMS) to simultaneously map polymer phase structure with detailed chemical information. Although TOF-SIMS is a powerful surface technique, it can be extended to microscopic bulk compound analysis. This is achieved by cryogenic sectioning of the elastomer compound, generating a sample surface, which is representative of the bulk. Other non-destructive techniques have been developed to study the physico-chemical and spatial microstructures resulting from cross-linking reactions. Atomic force microscopy (AFM) has been developed rapidly into a powerful tool, which can image the surface topography and determine the cross-link density, the modulus and the microdispersion of carbon-black on a fine scale.¹⁵ X-ray microtomography (XRMT) is a relatively new and effective technique for the non-destructive testing of polymers. It can provide very high spatial resolution images with a contrast mechanism that complements MRI and can be used for imaging foreign inclusions, the distribution of curative agent and other density contrast features in cured elastomer samples.¹⁶

Another evident approach for the molecular characterization of elastomers is certainly the direct investigation into chemical structures by means of high resolution ^1H or ^{13}C NMR spectroscopy and relaxation time experiments. Several authors already presented the use of high resolution solid state ^{13}C NMR as a powerful method for the chemical characterization of network structures.¹⁷ Buzaré¹⁸ and Somers¹⁹ used high resolution solid state ^{13}C NMR (CP/MAS) to investigate the effect of thermal oxidative aging on natural rubber vulcanizates without antioxidant. A detailed description of the morphology and molecular dynamics of the elastomers in bulk can also be performed by using solid state NMR relaxation experiments²⁰ and ^2H NMR lineshape analyses.²¹ Amongst the many applications are the quantitative determination of the cross-link density²² and the study of polymer-filler interactions.²³

Although NMR spectroscopy (especially ^{13}C CP/MAS spectroscopy) offers great insight into the chemical composition and the bulk morphology of elastomers, more answers about the (macroscopic) properties of rubbers are rather found in the spatial microstructure and morphology of the cross-linked network. Since the introduction by Lauterbur in 1973,²⁴ nuclear magnetic resonance imaging (MRI) has been developed as a modern approach, which is particularly suited for mapping the spatial morphology of elastomer samples. It is a unique, non-destructive and non-invasive technique for the three-dimensional analysis of materials.²⁵ Several thorough reviews on the subject of NMR imaging of elastomers have already been published.²⁶ These reviews and numerous previous reports on MRI of elastomers have focussed on the study of many different features in the field of elastomer networks such as aging, solvent diffusion, determination of the cross-link density and stress-strain studies.

Imaging of native elastomers by conventional hardware has proven to be often very difficult as a result of the rather broad natural line widths (tens of kHz). This results in images of low resolution and low signal-to-noise ratio. Swelling the elastomers in an appropriate solvent increases the molecular mobility (and so the T_2 relaxation time) and typically gives acceptable resolution in ^1H MRI (line narrowing).²⁷ Besides, the ability to swell elastomers to several times their original dimensions enables resolution of morphologically well defined features such as voids and cross-link density gradients.

An often-used application of MRI is the study of the swelling and diffusion behavior of organic solvents penetrating into elastomers. In MRI investigations of elastomers swollen in protonated solvents, the rubber itself often appears almost invisible due to its much shorter T_2 compared to that of the solvent, allowing a good discrimination between the swelling solvent and the rubber. This can be used to study the diffusion characteristics and to establish diffusion laws for the penetration of solvents into elastomers.²⁸ Chemical shift selective spin-echo techniques enable the investigation of the diffusion of individual components of bi-component solvent mixtures.²⁹

A very interesting aspect of MRI on cured elastomers, is the possibility to detect local differences in cross-link density.³⁰ Local distributions in cross-link density might originate from insufficient mixing and inhomogeneous temperature distributions during vulcanization, which can have a large influence on the performance of the elastomer. The degree of chemical and physical (entangled) cross-linking of the polymer chains is reflected by the molecular mobility of the chain segments, reflecting their position relative to the cross-links. Differences in molecular mobility are visualized in the MRI images by variations in the relaxation parameters: T_2 , T_1 and $T_{1\rho}$ and consequently variations in image contrast. The swelling behavior of rubber vulcanizates can also be used as a probe to detect inhomogeneities and spatial distributions in cross-link density. The domains of low solvent concentration can be correlated with higher cross-link density while similarly regions of high solvent concentration can be correlated with lower cross-link density.³¹

Closely related to the detection of local differences in cross-link density is the spatially resolved MRI study of elastomers in the course of thermal-oxidative and mechanical aging.³² Most elastomers remain reactive materials even after vulcanization due to their unsaturated nature. Depending on the type and the content of filler, various additives, temperature, chemical environment and time, a quite complex and spatially inhomogeneous aging process can be observed by means of MRI. This is most clearly shown by changes of the T_2 relaxation time.

Besides the detection of variations in cross-link density, MRI also makes it possible to visualize other defects such as voids, chunks of carbon-black (filler) or other foreign materials in cured elastomers based on differences in magnetic

susceptibility of the enclosed inhomogeneities in comparison to the surrounding rubber.³³

Another important application is the identification of stress distributions in rubber products under real working conditions. This is informative for polymer engineering since the spatial distribution of stress is often crucial for the functioning of the product. MRI provides a new probe to study the distribution of strain by probing either local molecular dynamics or chain orientation. Stretched rubber bands have been investigated by using T_2 parameter imaging: stress inhomogeneities in the sample could clearly be distinguished by local differences in molecular mobility.³⁴ A more advanced technique to detect stress in networks is the use of ^2H NMR imaging on deuterated elastomers.³⁵ Under uni-axially applied strain, the chain motion becomes anisotropic and the deuterium resonance is split into a doublet, which can be exploited to provide a quantitative characterization of the local stress. A complementary technique is the measurement of the residual proton dipolar coupling for stretched elastomers by using NMR filters based on spin multipoles,³⁶ resulting in two-dimensional ^1H parameter maps of stress in strained elastomer bands. The higher sensitivity of the proton nucleus and the avoidance of tedious synthesis of deuterated networks are some of the advantages of this technique as compared to ^2H MRI.

To image the rigid native elastomer, a number of solid state imaging sequences have been exploited, based on artificial line narrowing techniques or the use of larger field gradients and faster switching circuits. Both techniques require powerful radio frequency (RF) pulses and special hardware. Though the use of magic angle spinning (MAS) ^1H NMR imaging and other line narrowing techniques³⁷ have led to good quality images, the methods that use larger field gradients and other multiple-pulse methods³⁸ are more frequently used.

3.1.4. Aim and outline of this chapter

The aim of the research described in this chapter, is to make a contribution to the exploitation of the modern possibilities of micro-MRI for studying cross-linked isobutylene-based elastomers, used for the production of car tires. These

elastomers have to present excellent properties in connection to strength, heat-resistance and resistance against oxidative aging and consequently have to be chosen very carefully. In their practical use, these cross-linked elastomers are usually incorporated with highly reinforcing fillers such as carbon-black to enhance more than ten-fold the strength of the rubber matrix.³⁹ The analysis of the structure-property relationship of tire materials is of importance not only for the design of tires with improved functional properties, but also for the production of tires with an extended time of use. The mechanical properties of elastomers do not only depend on bulk parameters, such as physical and chemical cross-link densities, volume fraction of filler, or concentration of defects, but especially on a homogeneous, three-dimensional spatial distribution of these structures throughout the polymer network. MRI is the pre-eminent technique to study these properties of polyisobutylene elastomers because of its possibility to spatially detect defects and other inhomogeneities in the polymer network. MRI allows to observe the spatial distribution of the most important NMR parameters (M_0 , T_2 and T_1) and to correlate them with local differences in proton concentration and molecular mobility. Chemical shift selective MRI on the other hand, can be used to image selectively one particular chemical component of the network.

In section 3.2., it is demonstrated that the molecular chain mobility of the PIB-PMS/BrPMS elastomer is too small to obtain MRI images of the dry native rubber by means of the conventional MRI techniques. The mobility of the polymer network can be enhanced by increasing the temperature or by swelling the elastomers in an appropriate solvent. The optimal experimental conditions for obtaining images of the rubber matrix or of the swelling solvent are determined in section 3.3.. In section 3.4., a detailed analysis of local variations in cross-link density of unfilled 1,6-hexamethylene-diamine cured polyisobutylene elastomers is performed on MRI rubber images. Solvent MRI images on the other hand, reveal the diffusion kinetics of the ingress of cyclohexane in these elastomers.

Section 3.5. presents chemical shift selective rubber images to study the heterogeneity of mixing in a blend. The presence of voids, clearly resolved in solvent images of PIB elastomers, is confirmed in section 3.6. by MRI images of a dry unswollen isobutylene elastomer, a three-dimensional reconstruction, SEM

Chapter 3

and XRMT experiments and by a solid state NMR study. Section 3.7. deals with a statistical void density analysis to formulate a correlation between the number of voids and the mechanical properties of commercial carbon-black filled polyisobutylene elastomers. Also the influence of the filler and voids on the molecular chain mobility and diffusion characteristics of the carbon-black filled PIB elastomers is studied. Finally, an MRI imaging study of commercial PIB elastomers under mechanical load is presented in section 3.8..

3.2. Optimization of the MRI parameters *

3.2.1. Introduction

Although the molecular mobility of the chain segments of polyisoprene and polybutadiene rubber is large enough to directly record MRI images of the rubber matrix by using the conventional MRI techniques,⁴⁰ this is not the case for polyisobutylene. Even though the glass-transition temperature T_g of polyisobutylene is comparable to that of polybutadiene or polyisoprene, the chain dynamics are significantly reduced due to the steric constraints associated with interchain packing of the methyl groups (Scheme 3.1).⁴¹ This results in a short T_2 relaxation time of only 100 μ s for polyisobutylene at ambient temperature. Hence it is not possible to image native PIB elastomers by using the standard MRI techniques. As a consequence, MRI data for polyisobutylene and its derivatives are noticeably absent from the literature. One option to circumvent this issue is to enhance the molecular chain mobility by swelling the elastomer in the appropriate solvents and to record MRI images either of the swelling solvent or of the swollen rubber matrix.²⁷

3.2.2. Determination of the spin-spin T_2 relaxation decay time for cured unfilled PIB elastomers

The poly(isobutylene-p-methylstyrene-p-bromomethylstyrene) elastomer (PIB-PMS/BrPMS) contains about 90 - 98 mole % PIB, and as such the chain dynamics and relaxation properties are similar to neat polyisobutylene. For some unfilled cross-linked PIB-PMS/BrPMS elastomers used in this study, the ^1H T_2 relaxation times from static CPMG experiments are shown in Figure 3.1.

* A part of this section has been published: Adriaensens, P.; Pollaris, A.; Vanderzande, D.; Gelan, J.; White, J.L.; Dias, A.J.; Kelchtermans, M. *Macromolecules* **1999**, *32*, 4692.

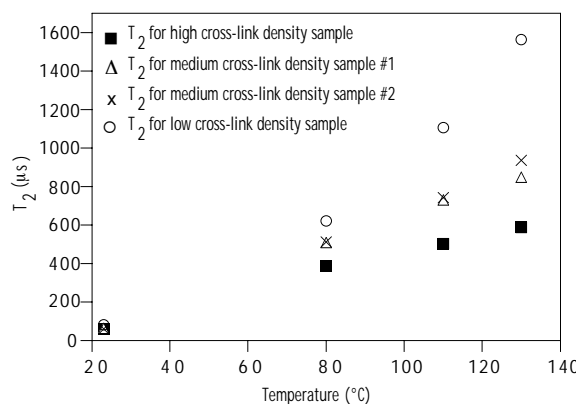


Figure 3.1: ^1H T_2 relaxation times as a function of temperature for four different cure states of PIB-PMS/BrPMS elastomers.

Figure 3.1 shows that at room temperature the relaxation properties are independent of cross-link density. However, at elevated temperatures, the T_2 relaxation times increase and this increase is larger for the low cross-link density sample as compared to the high cross-linked elastomer sample. So at higher temperatures, there is a significant dispersion in T_2 values due to differences in the overall cure state. These results already demonstrate that T_2 relaxation times, obtained from CPMG measurements, are very sensitive to small changes in cross-link density at elevated temperatures.

3.2.3. ^1H spectra of swollen PIB elastomers

Given that the ^1H T_2 relaxation time is too short to directly image the neat polyisobutylene elastomers at room temperature, swelling solvents can be used to facilitate image acquisition by using the standard spin-echo methods. The correlation time for chain mobility will be reduced by swelling the elastomers in appropriate solvents and the proton line width is reduced to an extent, acceptable for MRI.²⁷ The unfilled PIB-PMS/BrPMS elastomers were swollen in three different solvents: cyclohexane (C_6H_{12}), benzene (C_6H_6) and carbon tetrachloride (CCl_4) and the ^1H spectra are presented in Figure 3.2.

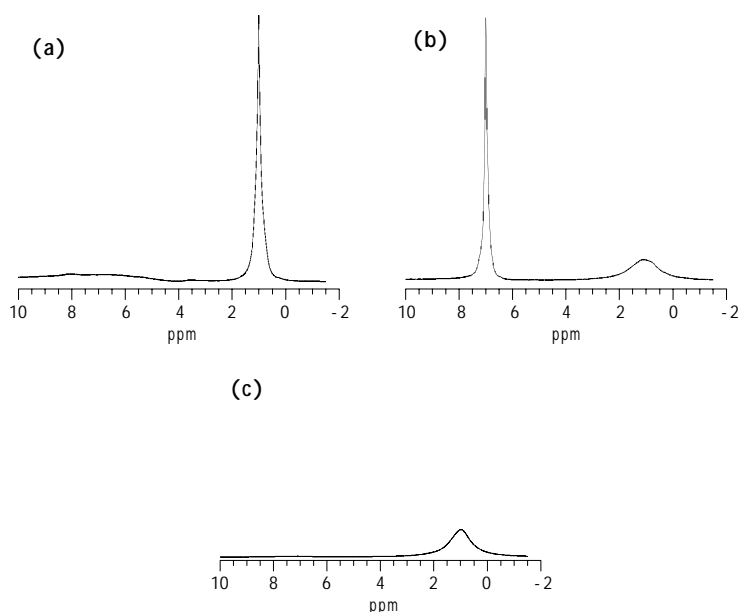


Figure 3.2: ^1H spectra of an unfilled PIB elastomer, swollen in (a) cyclohexane (b) benzene and (c) carbon tetrachloride.

The single proton signal at about 1 ppm in the ^1H spectrum of the cyclohexane-swollen elastomer (Figure 3.2a) results from the overlapping signals of both the solvent and the polymer. But the proton signal in the MRI image will mainly originate from the protonated solvent since the protons of the hydrocarbon chains are less mobile and hence do not significantly contribute to the NMR signal. A second reason is that the NMR receiver mainly detects the most dominant proton signal of the solvent.

When the elastomer is swollen in benzene, the solvent signal (at about 7 ppm) and the polymer signal (at about 1 ppm) are clearly resolved in the proton spectrum (Figure 3.2b). In this case, chemical shift selective excitation techniques can be used to edit the responses of the individual components, allowing to selectively image either the swelling solvent or the rubber matrix at exactly the same slice position.

The a-protic solvent CCl_4 enhances the molecular mobility of rubber segments, while giving no contribution to the intensity of the ^1H signal. Consequently, the NMR signal in the proton spectrum (Figure 3.2c) and the MRI image originates purely from the rubber spins.

3.2.4. MRI images of swollen PIB elastomers

An unfilled cross-linked PIB-PMS/BrPMS sample was swollen in the three solvents mentioned above. Circular samples of 15 mm in radius were punched out from the molded sheets by means of a sharp edged steel die and placed in the MRI sample tube. The MRI images, obtained by imaging either the solvent or the polymer are presented in Figure 3.3.

The MRI image in Figure 3.3a arises mainly from cyclohexane because of its more intense proton resonance (there is only a minor contribution of the polymer signal). The image clearly displays some dark circular spots, which contain no signal from the solvent nor from the polymer. These black spots cannot be attributed to the filler since it concerns an unfilled rubber. Moreover, because of their regular spherical shape, it is very unlikely that they result from highly cross-linked regions. Most of the spots are partially surrounded by a crescent-shaped bright intensity ring. These are magnetic susceptibility artifacts and appear along the readout direction, as was confirmed by imaging the object in different orientations. The appearance of such bright fringes is expected if the dark spots are voids in the polymer since severe magnetic susceptibility gradients exist at an air/polymer interface.⁴² However, there is still ambiguity in the literature about the assignment of these dark spots to the presence of voids and a detailed study about this void assignment is presented in section 3.6..

Figure 3.3b is obtained by using the a-protic solvent CCl_4 . The proton signals in this image necessarily arise from only the polymer, with no interference from the solvent. One can observe some light and dark polymer regions. The signal intensity in proton images depends on the proton concentration (M_0) and the T_1 and T_2 relaxation times. Differences in cure state strongly affect the swelling processes and hence the relaxation parameters that influence the image contrast of the swollen polymer.⁴³ For a fixed echo time (TE), the spin-echo signal intensity increases if T_2 increases (or if the molecular mobility of the polymer segments increases). So the clear regions in the MRI image indicate an increased mobility of the polymer chains due to a lower cross-link density or longer chain segments between the cross-links. Darker domains in the MRI image represent regions of less mobile polymer chains or highly cured material. Such inhomogeneities in cross-link density can arise from improper mixing, thermal gradients or variations in cross-linking chemistry.

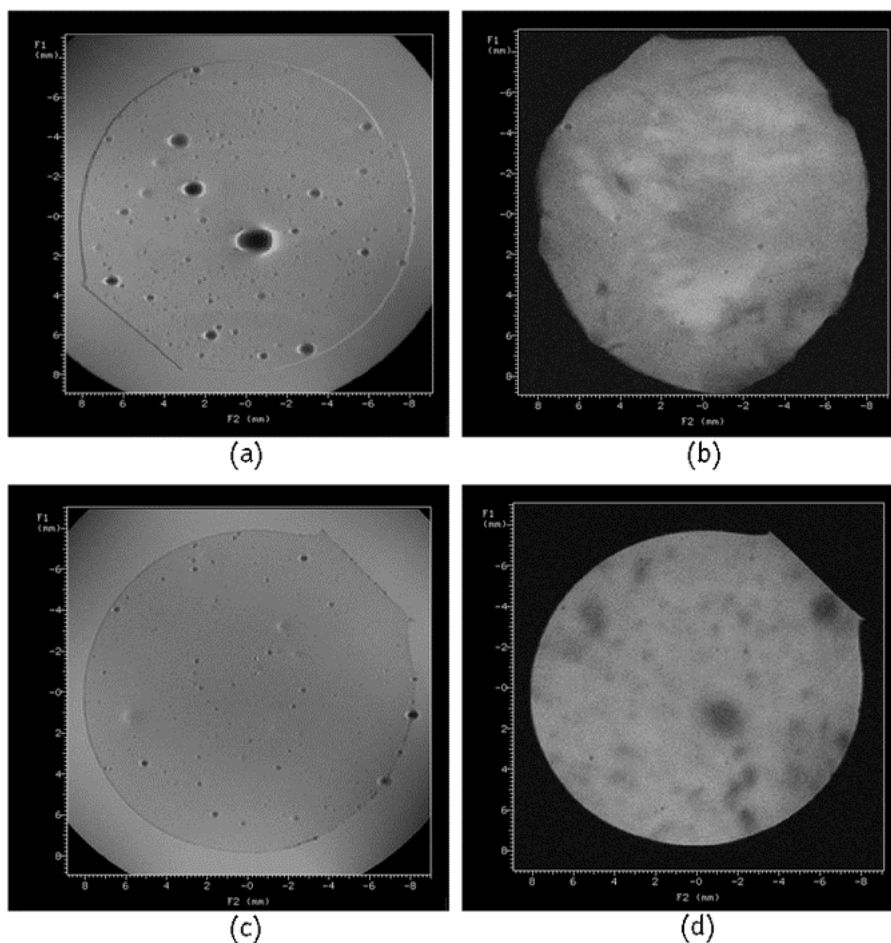


Figure 3.3: MRI images of unfilled PIB-PMS/BrPMS elastomers swollen in (a) cyclohexane, (b) CCl_4 , and (c-d) benzene: (c) solvent image, (d) polymer image.

Figure 3.3c and 3.3d represent a benzene-swollen sample in which either the solvent or the polymer is selectively imaged by using a chemical shift selective pulse sequence (aromatic versus aliphatic signal excitation). The dark circular spots, possibly assigned to voids, are more clearly resolved in the solvent image (Figure 3.3c), whereas the regions corresponding to local differences in cure state, are more easily distinguished in the aliphatic image (Figure 3.3d).

3.2.5. Conclusion

Because of the very low chain mobility of polyisobutylene at room temperature, it is impossible to obtain MRI images of the dry, unswollen material by using the conventional MRI techniques. To overcome this problem, the chain mobility of the PIB elastomers is increased by swelling in different organic solvents in order to obtain good quality NMR images. It is demonstrated that polymer images (of elastomers swollen in CCl_4 or in benzene) are preferred to visualize local differences in cross-link density as they are giving rise to intensity variations in the rubber image. Images of the swelling solvent, on the other hand, (cyclohexane or benzene) are superior towards the visualization of the dark spots (voids).

3.3. Influence of the nature of the curing agent on the network topology

The curing process of PIB-PMS/BrPMS is quite complex. Cross-linking can be performed in assistance of ZnO (classical) or by means of an 'organic' curative, 1,6-hexamethylenediamine. It is proposed that, in the presence of ZnO, the benzylic bromide functionality can react with the other aromatic moieties by an electrophilic aromatic substitution reaction.⁹ Figure 3.4 presents the chemical shift selective MRI images of an unfilled, ZnO-cured PIB-PMS/BrPMS elastomer, swollen in benzene.

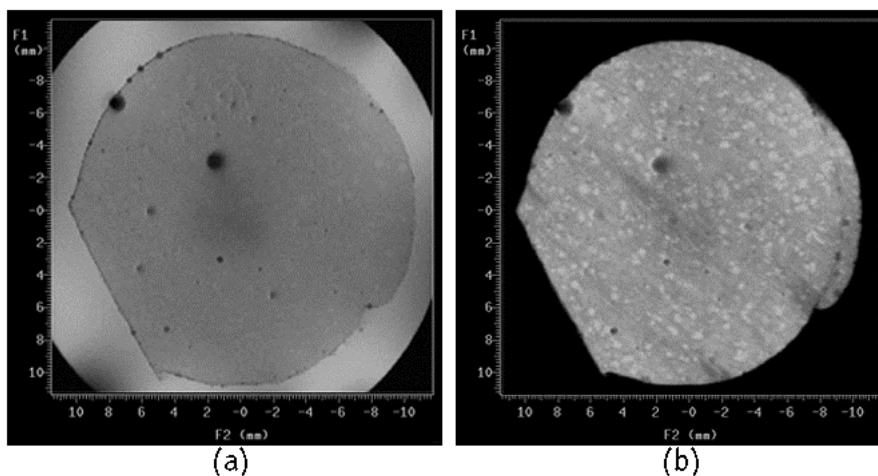


Figure 3.4: MRI images of an unfilled, ZnO-cured PIB-PMS/BrPMS elastomer swollen in benzene: (a) solvent image, (b) rubber image (TE=25 ms).

In the presence of 1,6-hexamethylenediamine, cross-linking is established by displacement of the benzylic bromide group by the diamine curative in a nucleophilic substitution reaction mechanism.⁴⁴ The chemical shift selective MRI images of an unfilled 1,6-hexamethylenediamine-cured PIB-PMS/BrPMS elastomer, swollen in benzene, are presented in Figure 3.5.

The solvent images in Figure 3.4a and 3.5a clearly reveal the dark circular spots (probably assignable to voids). These dark spots are also visible in the polymer images (Figure 3.4b and 3.5b) as they contain no signal from the elastomer. The rubber images are recorded with a longer echo time (TE) to enhance contrast between regions with a different cross-link density (i.e.

imposing a T_2 -filter). Variations in cross-link density are clearly observable in these polymer images.

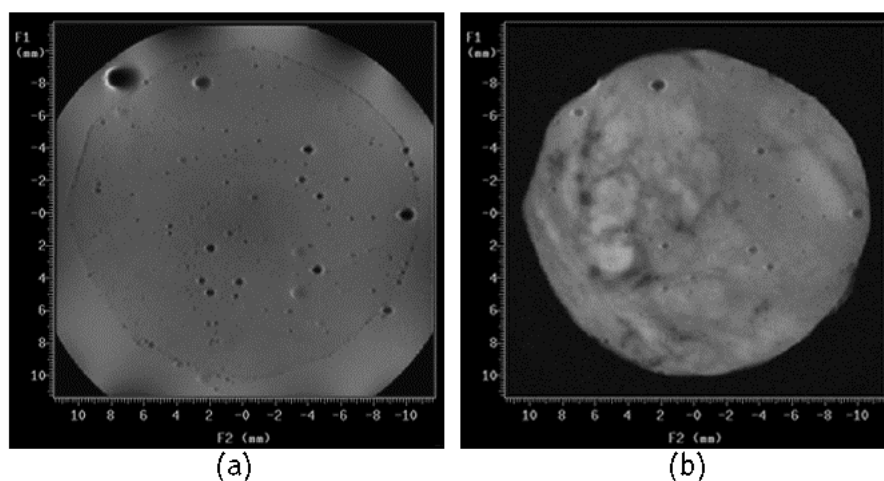


Figure 3.5: MRI images of an unfilled 1,6-hexamethylenediamine-cured PIB-PMS/BrPMS elastomer swollen in benzene:
(a) solvent image, (b) rubber image ($TE=25$ ms).

Comparing the polymer images of Figure 3.4b and 3.5b, it is obvious that the topology of the network heterogeneities is very different for the two elastomers. The rubber image of the ZnO-cured elastomer (Figure 3.4b) displays well-defined, circular regions of loosely cured polymer (increased intensity), while the diamine-cured elastomer (Figure 3.5b) exhibits irregular swirled density gradients. These differences are consistent with what one would expect for dispersing a solid (ZnO) versus a liquid (1,6-hexamethylenediamine) into a viscous medium. These results emphasize the need to optimize mixing procedures for adequate dispersion of the curative in the viscous polymer matrix. Obviously an inorganic solid like ZnO, requires a different mixing strategy than an organic liquid-like curative.

3.4. MRI study of unfilled 1,6-hexamethylene-diamine cured PIB elastomers with a different cross-link density *

3.4.1. Study of the cross-link density of elastomers by means of MRI rubber images

3.4.1.1. Introduction

The preceding results already demonstrated that NMR imaging of polymer spins can be used to probe the spatial distribution of the cross-link density: polymer regions with low signal intensity correlate with high cross-link density, while regions of high signal intensity correlate with a lower cross-link density. It is already stated in literature that measurement of the ^1H NMR relaxation time behavior is a successful method to study the dynamic motions in elastomeric systems at temperatures well above the glass transition temperature T_g . These motions are highly effected by cross-linking reactions and the dispersion of network junction points.⁴⁵ As a start, the bulk cross-link density of the unfilled 1,6-hexamethylenediamine cured PIB-PMS/BrPMS elastomers, determined by means of equilibrium swelling experiments and the Flory-Rehner equation, is correlated with the volume-averaged T_2 relaxation time. This correlation will be used to determine the local cross-link density by means of the spatially dependent T_2 decay times, determined via MRI.

3.4.1.2. Determination of the number-average molecular weight between the effective cross-links ($M_{n,eff}$) by using the Flory-Rehner equation

Equilibrium-swelling measurements are in literature frequently used to determine the cross-link density in elastomers.⁴⁶ The method is based on the fact that with a higher cross-link density, less solvent is penetrating in the system, which results in a lower degree of swelling and vice versa. The classical

* A part of this section has been published: Adriaensens, P.; Pollaris, A.; Vanderzande, D.; Gelan, J.; Kelchtermans, M. *Macromolecules* **2003**, *36*, 706.

Chapter 3

thermodynamics of binary polymer-solvent systems were developed by P. J. Flory and M. L. Huggins and take account for the effect of differences in molecular volume of solvent molecules on the entropy of mixing.⁴⁷ This has led to the deduction of the Flory-Rehner equation, which can be used to calculate the bulk number-average molecular weight between the effective cross-links (i.e. the sum of physical and chemical cross-links), $M_{n,eff}^b$:

$$\frac{1}{M_{n,eff}^b} = \nu = \frac{-[\ln(1 - V_r) + V_r + \chi V_r^2]}{\rho_r V_0 (V_r^{1/3} - V_r/2)} \quad (3.1)$$

with: ν = density of the network chains (in mole chains per gram rubber)

V_r = volume fraction of the rubber in the swollen vulcanizate

χ = Flory-Huggins polymer-solvent interaction parameter

ρ_r = density of the unswollen rubber (0.917 g/cm³ for PIB)

V_0 = molar volume of the swelling solvent (108 cm³/mol for cyclohexane).

Values of V_r were determined from the weight difference between the unswollen and swollen sample:

$$V_r = \left[\left(\frac{\rho_r}{\rho_s} \right) \left(\frac{W_{eq} - W_0}{W_0} \right) + 1 \right]^{-1} \quad (3.2)$$

with: ρ_s = density of the solvent (0.779 g/cm³ for cyclohexane)

W_{eq} = weight of the swollen rubber at equilibrium

W_0 = weight of the dry native rubber sample

Equilibrium swelling in cyclohexane was performed at ambient temperature for four unfilled 1,6-hexamethylenediamine cured PIB-PMS/BrPMS elastomers with a different cross-link density. The Flory-Huggins interaction parameter χ , being concentration dependent, can be obtained from the following power series:

$$\chi = \chi_0 + \chi_1 V_r + \chi_2 V_r^2 \quad (3.3)$$

with: $\chi_0 = 0.44$, $\chi_1 = -0.083$ and $\chi_2 = 0.068$ for the system PIB-cyclohexane.⁴⁸

The results for the different cure states are presented in Table 3.1. The torque values represent cross-link data measured by a mechanical oscillating disk rheometer. A plot of the bulk number-average molecular weight between the effective cross-links as a function of the rheometer torque is presented in Figure 3.6.

Table 3.1: The number-average molecular weight between the effective cross-links, calculated by means of the Flory-Rehner equation.

	elastomer 1	elastomer 2	elastomer 3	elastomer 4
V_r	8.45×10^{-2}	8.75×10^{-2}	11.95×10^{-2}	20.58×10^{-2}
χ	0.4335	0.4333	0.4311	0.4258
$M_{n,eff}^b$ (g/mole)	56954	52821	26641	7337
Torque (dNm)	4.4	9.1	14.9	28.8

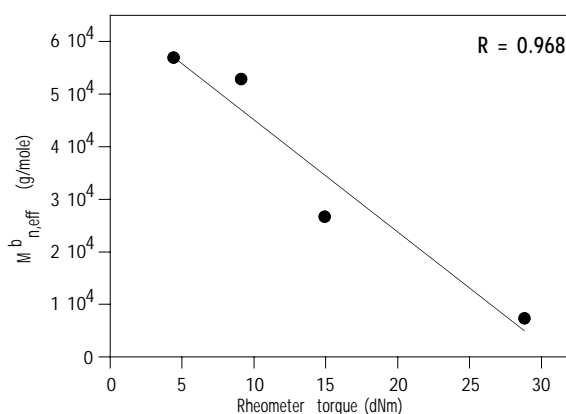


Figure 3.6: Bulk number-average molecular weight between the effective cross-links ($M_{n,eff}^b$) as a function of rheometer torque (R = correlation coefficient).

The degree of cure enhances from elastomer 1 towards elastomer 4 as is demonstrated by the torque values of the rheologic experiments. The plot shows an inverse linear correlation (correlation coefficient $R = 0.968$): the higher cross-link density (or higher torque) corresponds to a lower number-average molecular weight between effective cross-links. These gravimetric Flory-Rehner experiments confirm the appreciable variation in the bulk cross-link density for the different PIB elastomers.

3.4.1.3. Determination of the volume-averaged T_2 relaxation times for unfilled 1,6-hexamethylenediamine cured PIB elastomers with a different cross-link density

NMR relaxation experiments were performed at ambient temperature for the four unfilled 1,6-hexamethylenediamine cured elastomers, swollen in CCl_4 . By using the aprotic solvent CCl_4 , the proton resonances originate exclusively from the rubber methyl protons without interference of the swelling solvent. For each elastomer, the volume-averaged proton T_1 relaxation decay time was determined by analyzing the 1-D projection signal intensity vs. a variable repetition delay TR according to equation 3.4. The volume-averaged proton T_2 relaxation behavior was obtained by analyzing the intensity of the 1-D projections, obtained as a function of the echo time TE according to the following bi-exponential equation (eq. 3.5):

$$M_t = M_0 \left(1 - \exp\left(-\frac{TR}{T_1}\right) \right) \quad (3.4)$$

$$M_t = M_{0,s} \exp\left(-\frac{TE}{T_{2,s}}\right) + M_{0,l} \exp\left(-\frac{TE}{T_{2,l}}\right) \quad (3.5)$$

Table 3.2 presents the volume-averaged proton T_1 and T_2 relaxation decay times after equilibrium swelling in CCl_4 . While the T_1 decays were mono-exponential (eq. 3.4), the T_2 analysis (eq. 3.5) resulted in a short ($T_{2,s}$) and a long decay time ($T_{2,l}$). The short T_2 component can be assigned to the network chain segments that are constrained by surrounding cross-links and entanglements, while the long T_2 component represents mobile network chains, further removed from the cross-links and entanglements.⁴⁹ The molar fraction weighted volume-averaged T_2 decay time ($T_{2,mfw}$) is also presented in Table 3.2.⁵⁰

Table 3.2: Volume-averaged T_1 and T_2 relaxation decay times (and fractions $M_{0,i}$) of the unfilled 1,6-hexamethylenediamine cured PIB elastomers with different cross-link density, swollen to equilibrium in CCl_4 .

	elastomer 1	elastomer 2	elastomer 3	elastomer 4
$M_{n,eff}^b$ (g/mole)	56954	52821	26641	7337
T_1 (s)	0.18	0.17	0.18	0.17
$T_{2,s}$ (ms)	15.4	15.0	8.8	5.7
$M_{0,s}$ (%)	32.1	28.4	41.9	65.7
$T_{2,l}$ (ms)	86.3	70.8	48.7	23.8
$M_{0,l}$ (%)	67.9	71.6	58.1	34.3
$T_{2,mfw}$ (ms) ^a	63.6	54.9	32.0	12.0

^a $T_{2,mfw}$ represents the molar fraction weighted volume-averaged T_2 decay time.

From Table 3.2 it is clear that, in contrast to the comparable T_1 decay times, the T_2 decay times are clearly dependent on the degree of cross-linking of the elastomer. T_1 is mainly determined by the fast (MHz) rotations of the methyl groups, which are quasi independent of the cure state. Because the efficiency of the T_2 relaxation is highly sensitive to low-frequency motions like these of the backbone chains, the average chain length between effective cross-links will strongly impact on the T_2 decay time. Specially the long component $T_{2,l}$ as well as $T_{2,mfw}$ decrease with increasing degree of cross-linking. This behavior is less pronounced for the short component ($T_{2,s}$ is somewhat comparable for the different elastomers), since the molecular chain mobility in the close vicinity of the cross-links clearly is less dependent of the cure state.

The relationship between the bulk $M_{n,eff}^b$ and the volume-averaged T_2 decay times is presented in Figure 3.7. A linear correlation is observed between the T_2 decay times (representing the molecular chain mobility) and the bulk cross-link density $M_{n,eff}^b$, which can be expressed by the following equations (with the correlation coefficient for the curve fitting indicated). These results confirm that mainly $T_{2,l}$ and $T_{2,mfw}$ vary strongly with the bulk $M_{n,eff}^b$.

$$T_{2,l} = 16.10 + 11.49 \times 10^{-4} M_{n,eff}^b \quad (R = 0.986) \quad (3.6)$$

$$T_{2,mfw} = 4.83 + 9.95 \times 10^{-4} M_{n,eff}^b \quad (R = 0.997) \quad (3.7)$$

$$T_{2,s} = 3.96 + 2.02 \times 10^{-4} M_{n,eff}^b \quad (R = 0.996) \quad (3.8)$$

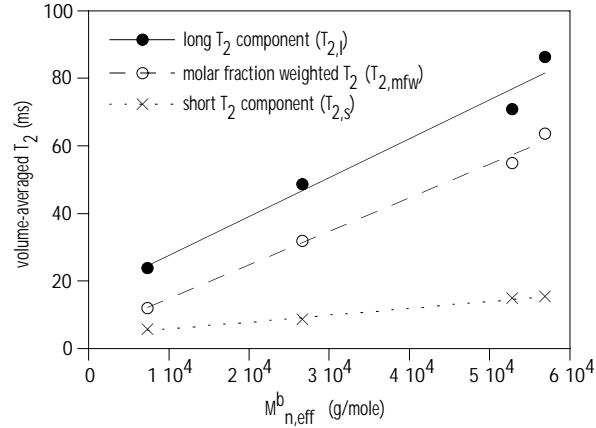


Figure 3.7: Volume-averaged T_2 relaxation decay times as a function of the bulk cross-link density ($M_{n,eff}^b$).

3.4.1.4. Image analysis: determination of the local T_2 relaxation times and correlation with the local cross-link density

a) Introduction

The equations 3.6 to 3.8 can be used to assign a local degree of cross-link density to specific regions in the rubber. Therefore, MRI rubber images were recorded at ambient temperature as a function of echo time TE for the four CCl_4 -swollen unfilled 1,6-hexamethylenediamine cured elastomers. Several regions of interest (ROI's) were selected in the images and the local T_2 relaxation times ($T_{2,s}$ and $T_{2,l}$) and corresponding fractions ($M_{0,s}$ and $M_{0,l}$) were obtained out of a bi-exponential analysis (eq. 3.5). Applying equation 3.7 on the spatially dependent molar fraction weighted T_2 value ($T_{2,mfw}^l$), allowed to deduce the local molecular weight between the effective cross-links $M_{n,eff}^l$ for each ROI in the MRI rubber images. This calculation was performed for the four elastomers. For each elastomer, a rubber image of the CCl_4 -swollen elastomer and an identical image, indicating the selected ROI's, are presented.

b) MRI images and spatially dependent cross-link density for the four unfilled 1,6-hexamethylenediamine cured PIB elastomers with different cure state

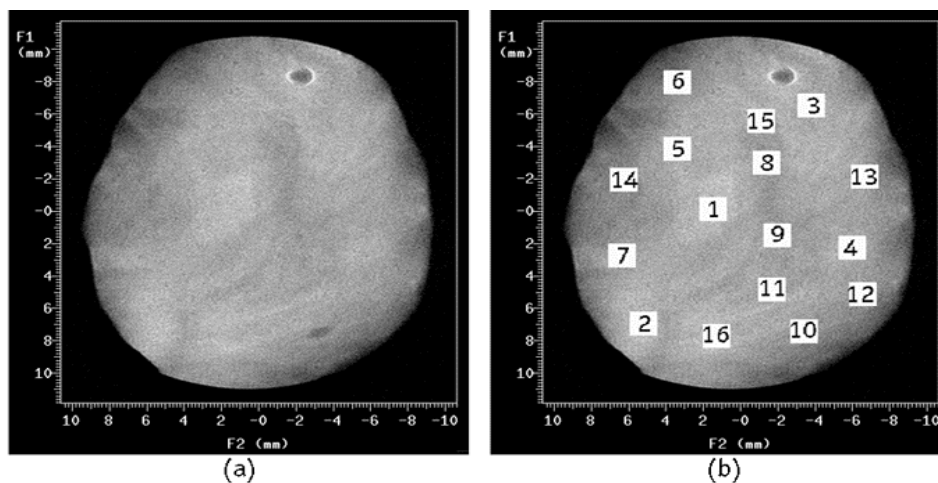


Figure 3.8: MRI rubber images of elastomer 1 ($M_{n,eff}^p = 56954$ g/mole), swollen in CCl_4 , with (b) indication of the ROI's used to determine the local T_2 relaxation decay times.

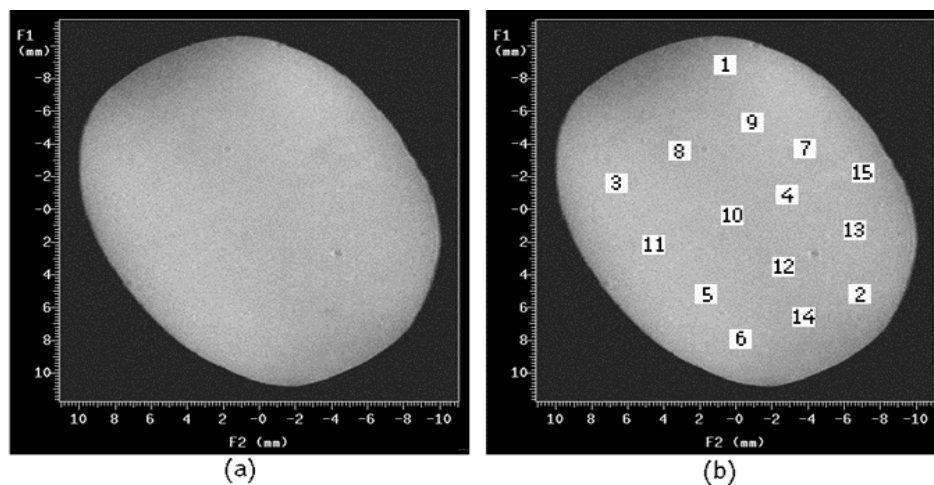


Figure 3.9: MRI rubber images of elastomer 2 ($M_{n,eff}^p = 52821$ g/mole), swollen in CCl_4 , with (b) indication of the ROI's used to determine the local T_2 relaxation decay times.

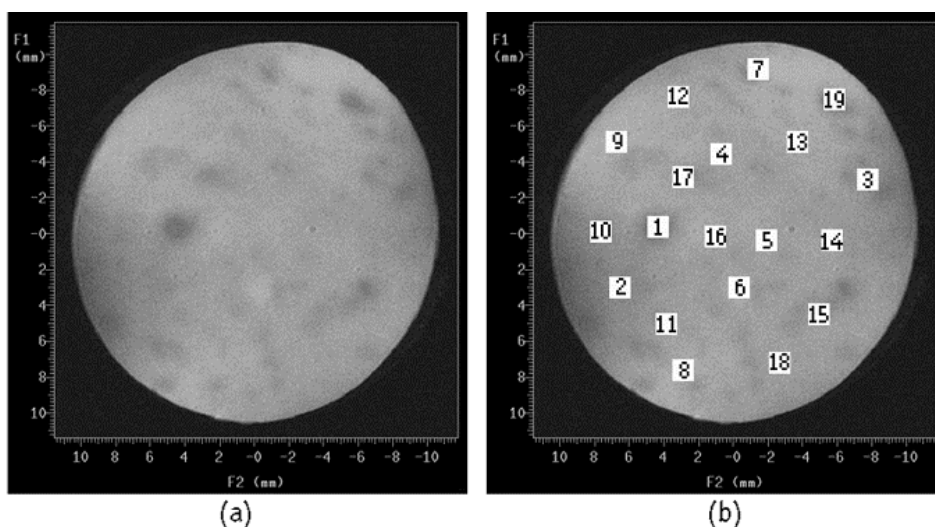


Figure 3.10: MRI rubber images of elastomer 3 ($M_{n,eff}^p = 26641$ g/mole), swollen in CCl_4 , with (b) indication of the ROI's used to determine the local T_2 relaxation decay times.

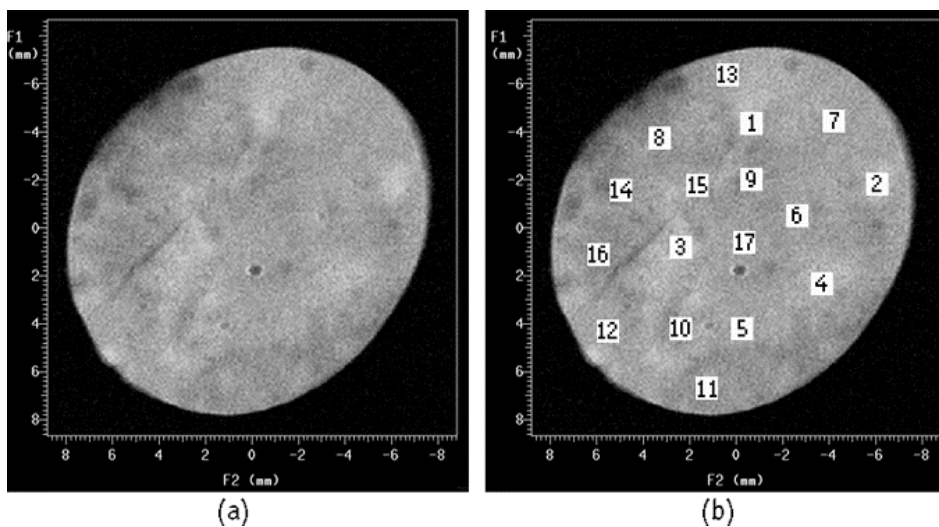


Figure 3.11: MRI rubber images of elastomer 4 ($M_{n,eff}^p = 7337$ g/mole), swollen in CCl_4 , with (b) indication of the ROI's used to determine the local T_2 relaxation decay times.

Table 3.3: Spatially dependent T_2 relaxation times and cross-link density for the unfilled 1,6-hexamethylenediamine cured PIB elastomer 1, swollen to equilibrium in CCl_4 .

	$T_{2,s}$ (ms)	$M_{0,s}$ (%)	$T_{2,l}$ (ms)	$M_{0,l}$ (%)	$T_{2,mfw}^I$ (ms)	$M_{n,eff}^I$ (g/mole)
ROI 1	20.1	14.4	112.6	85.6	99.3	94945
ROI 2	17.1	35.0	86.2	65.0	62.0	57457
ROI 3	25.7	29.3	104.7	70.7	81.6	77156
ROI 4	25.0	33.7	95.1	66.3	71.5	67005
ROI 5	24.2	20.5	107.1	79.5	90.1	85698
ROI 6	15.4	43.8	91.4	56.2	58.1	53538
ROI 7	28.3	27.8	111.3	72.2	88.2	83789
ROI 8	19.8	33.3	85.7	66.7	63.8	59266
ROI 9	12.8	27.5	76.2	72.5	58.8	54241
ROI 10	13.8	71.2	94.7	28.8	37.1	32432
ROI 11	24.7	48.7	102.4	51.3	64.6	60070
ROI 12	13.7	30.4	91.0	69.6	67.5	62985
ROI 13	19.1	41.7	94.8	58.3	63.2	58663
ROI 14	16.2	35.8	85.0	64.2	60.4	55849
ROI 15	15.2	43.4	69.8	56.6	46.1	41477
ROI 16	13.3	25.4	87.1	74.6	68.3	63789
mean $M_{n,eff}^I \pm \text{std. dev.} = 63022 \pm 16071$						

For a comparison, the volume-averaged results are: $M_{n,eff}^0 = 56954$ g/mole
 $T_{2,mfw} = 63.6$ ms

Table 3.4: Spatially dependent T_2 relaxation times and cross-link density for the unfilled 1,6-hexamethylenediamine cured PIB elastomer 2, swollen to equilibrium in CCl_4 .

	$T_{2,s}$ (ms)	$M_{0,s}$ (%)	$T_{2,l}$ (ms)	$M_{0,l}$ (%)	$T_{2,mfw}^l$ (ms)	$M_{n,eff}^l$ (g/mole)
ROI 1	19.6	32.1	84.2	67.9	63.5	58965
ROI 2	8.4	24.8	72.7	75.2	56.8	52231
ROI 3	13.1	30.0	73.5	70.0	55.4	50824
ROI 4	10.5	28.1	70.6	71.9	53.7	49116
ROI 5	8.9	27.2	73.8	72.8	56.1	51528
ROI 6	13.2	26.4	77.4	73.6	60.5	55950
ROI 7	11.4	38.0	64.4	62.0	44.3	39668
ROI 8	19.4	29.0	78.6	71.0	61.4	56854
ROI 9	14.4	29.5	77.4	70.5	58.8	54241
ROI 10	18.0	26.8	76.0	73.2	60.5	55950
ROI 11	13.7	23.7	73.9	76.3	59.6	55045
ROI 12	9.4	23.9	72.4	76.1	57.3	52734
ROI 13	9.6	25.5	73.3	74.5	57.1	52533
ROI 14	10.9	25.8	74.3	74.2	57.9	53337
ROI 15	12.9	26.0	76.3	74.0	59.8	55246
mean $M_{n,eff}^l \pm \text{std. dev.} = 52948 \pm 4448$						

For a comparison, the volume-averaged results are: $M_{n,eff}^b = 52821$ g/mole
 $T_{2,mfw} = 54.9$ ms

Table 3.5: Spatially dependent T_2 relaxation times and cross-link density for the unfilled 1,6-hexamethylenediamine cured PIB elastomer 3, swollen to equilibrium in CCl_4 .

	$T_{2,s}$ (ms)	$M_{0,s}$ (%)	$T_{2,l}$ (ms)	$M_{0,l}$ (%)	$T_{2,mfw}^l$ (ms)	$M_{n,eff}^l$ (g/mole)
ROI 1	12.9	76.8	74.2	23.2	27.1	22382
ROI 2	17.5	60.2	74.1	39.8	40.0	35347
ROI 3	17.1	61.9	71.3	38.1	37.8	33136
ROI 4	11.9	47.5	57.1	52.5	35.6	30925
ROI 5	7.4	42.2	53.3	57.8	33.9	29216
ROI 6	11.3	32.4	67.5	67.6	49.3	44693
ROI 7	8.4	51.9	51.4	48.1	29.1	24392
ROI 8	13.7	42.7	64.9	57.3	43.0	38362
ROI 9	14.0	46.7	65.1	53.3	41.2	36553
ROI 10	4.9	41.6	53.4	58.4	33.2	28513
ROI 11	16.1	70.4	86.8	29.6	37.0	32332
ROI 12	13.4	42.0	61.5	58.0	41.3	36653
ROI 13	9.5	47.7	59.7	52.3	35.8	31126
ROI 14	9.1	41.8	56.1	58.2	36.5	31829
ROI 15	11.7	50.9	57.1	49.1	34.0	29317
ROI 16	8.7	36.6	57.6	63.4	39.7	35045
ROI 17	6.4	52.4	50.0	47.6	27.2	22482
ROI 18	15.0	46.2	69.5	53.8	44.3	39668
ROI 19	8.5	44.8	51.3	55.2	32.1	27407
mean $M_{n,eff}^l \pm \text{std. dev.} = 32073 \pm 5837$						

For a comparison, the volume-averaged results are: $M_{n,eff}^b = 26641$ g/mole
 $T_{2,mfw} = 32.0$ ms

Table 3.6: Spatially dependent T_2 relaxation times and cross-link density for the unfilled 1,6-hexamethylenediamine cured PIB elastomer 4, swollen to equilibrium in CCl_4 .

	$T_{2,s}$ (ms)	$M_{0,s}$ (%)	$T_{2,l}$ (ms)	$M_{0,l}$ (%)	$T_{2,mfw}^l$ (ms)	$M_{n,eff}^l$ (g/mole)
ROI 1	6.4	68.7	29.7	31.3	13.7	8915
ROI 2	5.5	71.3	27.7	28.7	11.9	7106
ROI 3	6.9	66.5	28.2	33.5	14.0	9216
ROI 4	6.5	64.5	26.8	35.5	13.7	8915
ROI 5	6.2	70.4	28.0	29.6	12.7	7910
ROI 6	5.9	69.3	26.8	30.7	12.3	7508
ROI 7	7.2	75.8	31.8	24.2	13.2	8412
ROI 8	5.8	74.0	27.4	26.0	11.4	6603
ROI 9	5.8	67.8	26.2	32.2	12.4	7608
ROI 10	6.8	77.5	31.7	22.5	12.4	7608
ROI 11	5.5	75.6	27.3	24.4	10.8	6000
ROI 12	5.8	69.2	27.6	30.8	12.5	7709
ROI 13	7.4	74.9	33.0	25.1	13.8	9015
ROI 14	4.6	70.0	23.2	30.0	10.2	5397
ROI 15	6.8	69.0	28.6	31.0	13.6	8814
ROI 16	4.4	67.4	24.3	32.6	10.9	6101
ROI 17	5.3	65.1	26.0	34.9	12.5	7709
mean $M_{n,eff}^l \pm \text{std. dev.} = 7679 \pm 1152$						

For a comparison, the volume-averaged results are: $M_{n,eff}^b = 7337$ g/mole
 $T_{2,mfw} = 12.0$ ms

c) Discussion

The rubber image of elastomer 1 in Figure 3.8 clearly shows a very heterogeneous network structure, as is also illustrated by the rather large variation in the localized $M_{n,eff}^I$ of the ROI's (Table 3.3). This indicates an unfavorable mixing procedure for this rubber type, resulting in rather large local differences in cross-link density. This is in strong contrast to the MRI rubber image of elastomer 2, showing a rather homogeneous network structure (Figure 3.9). This is also confirmed by the small variations in $M_{n,eff}^I$ (Table 3.4) and indicates a good homogeneous mixing, resulting in a uniform degree of curing. The homogeneity of mixing of the two remaining elastomers (elastomer 3 and 4) is somewhere in between. Tables 3.3 to 3.6 also demonstrate that the mean value of $M_{n,eff}^I$ approaches the bulk cross-link density obtained by gravimetry.

The complete set of results of the spatially dependent T_2 analysis (decay times and the corresponding fractions) as a function of $M_{n,eff}^I$ for all ROI's is graphically displayed in Figure 3.12. It can be observed that, for all ROI's of the four investigated elastomers, the value of the short decaying component $T_{2,s}$, increases only slightly with decreasing cross-link density.

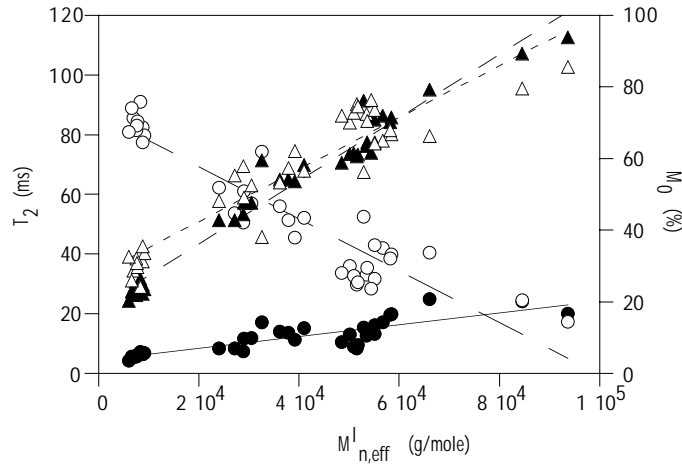


Figure 3.12: Spatially dependent T_2 decay times ($T_{2,s}$: ● and $T_{2,l}$: ▲) and their relative fractions ($M_{0,s}$: ○ and $M_{0,l}$: △) of the ROI's presented in the MRI images of all four elastomers (Figure 3.8 to 3.11) as a function of $M_{n,eff}^I$.

This short component was earlier assigned to the constrained regions of the network segments around the cross-links. Indeed, the mobility of these regions closely around the cross-links does not change very much by decreasing the cross-link density. But the fraction of $T_{2,s}$, of course, varies directly with the cure state since the concentration of the cross-links increases with increasing cross-link density. The long T_2 component ($T_{2,l}$), previously assigned to the relatively less constrained regions of the network chains further removed from the cross-links (intercross-link chains), as well as its fraction ($M_{0,l}$) clearly increase with decreasing cross-link density. In the low cross-link density regions, the intercross-link chains become longer, resulting in a larger mobility of these chain parts.

3.4.1.5. Conclusion

The obtained results clearly demonstrate that MRI is a useful technique to study the homogeneity of mixing and the curing of PIB-based elastomers. The importance of homogeneous mixing procedures with respect to the final mechanical properties needs no further comment. Combined with complementary gravimetric data from macroscopic equilibrium swelling experiments (Flory-Rehner), MRI offers detailed information on the dynamical behavior of the rubber chain segments at the molecular level (cross-link density). Although NMR imaging allows the visualization of inhomogeneities at a mesoscopic level (tens of micrometers), its strength is mainly situated in the ability to probe the underlying dynamical events at the nanometer level via T_2 relaxometry. More specific, on the basis of the linear relationship between the bulk T_2 decay times and the bulk degree of cross-linking, the spatially dependent T_2 decay times, determined on rubber MRI images of the CCl_4 -swollen elastomers, make it possible to establish the local $M_{n,\text{eff}}^l$ in inhomogeneously cured elastomers.

Although this method for determining the spatial variations in cross-link density is very time-consuming (requires swelling of the elastomers, gravimetry and image acquisition as a function of TE), fairly good results are obtained in contrast with the rather new multiple-quantum methods (described in literature),⁵¹ which suffer from intrinsic low signal-to-noise ratio.

3.4.2. MRI study of the diffusion of cyclohexane in unfilled 1,6-hexamethylenediamine cured PIB elastomers with different cross-link density

3.4.2.1. Introduction

The diffusion of solvents in polymer systems covers a wide range of transport regimes, depending primarily on the nature of the polymer⁵² and on the diffusing species.⁵³ The specific features observed during the diffusion process, vary greatly depending on whether the polymer is in the rubbery or (semi-) crystalline state at the imposed conditions of temperature and pressure.⁵⁴ The range of diffusion phenomena for polymer-solvent systems is going from common Fickian diffusion to Case II diffusion.⁵⁵ Alfrey et al.⁵⁶ proposed a classification of the diffusion behavior of solvents into polymers in three categories:

- Case I or Fickian diffusion is characterized by an increase in solvent concentration going from the inside of the polymer to the fully swollen regions at the outside of the sample. The rate of diffusion is much less than that of the polymer segmental relaxation rates. This behavior is also called diffusion-controlled and commonly applies to polymers in the rubbery state. In this case, the distance diffused by the solvent is proportional to the square root of diffusion time and the NMR T_2 relaxation time is relatively constant throughout the swollen part;
- Case II or relaxation-controlled diffusion, in which the rate of diffusion is much faster than that of the polymer segmental relaxation. This applies to polymers in the glassy state and the diffusion distance is now directly proportional to time. The T_2 decay time drops from the outer part towards the unswollen core;
- Non-Fickian or anomalous diffusion, which occurs when the rates of diffusion and segmental relaxation are comparable. In this case, the diffusion distance is proportional to time raised to a power between 0.5 and 1.

Evaluation of the diffusion process for a given polymer/solvent system will provide important information on the ingress kinetics, the homogeneity of the polymer matrix, possible phase transformations (e.g. solvent induced

crystallization) and eventually degradation.⁵⁷ Existing experimental methods for determining diffusion kinetics can be broadly classified into two approaches: those monitoring the mass uptake of the solvent as a time variable (gravimetric techniques)⁵⁸ and those measuring the concentration profile of the solvent within the polymer as a function of time. The latter include X-ray methods, radioactive tracer studies and FT-IR imaging spectroscopy.⁵⁹ But all these methods have their disadvantages. For example, with X-rays, differentiation of solid and penetrant can be difficult. Penetrant mass uptake relies on a model for the diffusion process and it yields no information on the concentration profile of the penetrant. Radioactive tracer studies, on the other hand, require slicing of the sample. Recently the determination of the diffusion coefficients by using gas chromatographic measurements is introduced, but this technique is mainly restricted to the absorption of small amounts of solvents.⁶⁰

Previous results already showed that nuclear magnetic resonance imaging (MRI) can be used to detect inhomogeneities in elastomer samples indirectly via ingress of a chemically inert solvent. In addition, MRI has been extensively described in literature as an excellent method to monitor the diffusion of penetrants into polymers in a non-destructive and non-invasive manner so avoiding the experimental limitations of the aforementioned techniques.⁶¹ One of the major advantages as compared with weight gain measurements and optical microscopy, is the ability to provide a visual presentation of the spatial distribution of solvent in the polymer without interrupting the diffusion process or destroying the sample. Another benefit is the possibility to separate diffusion, being a molecular process and hence specimen shape-independent, from matrix swelling, being a macroscopic and hence shape-dependent process. Since elastomers in all their application areas may come into contact with organic solvents, it is very useful to analyze the solvent ingress. In the next contribution, we will evaluate the use of MRI to study the diffusion of cyclohexane into unfilled 1,6-hexamethylenediamine cured polyisobutylene elastomers with a different cross-link density.

3.4.2.2. Determination of the diffusion kinetics by means of MRI and its correlation with the cross-link density for PIB elastomers

a) Theoretical background^{29d,62}

Since the glass transition temperature of polyisobutylene is about $-80\text{ }^{\circ}\text{C}$ and all MRI experiments are carried out at ambient temperature, the elastomer will be in the rubbery state during the diffusion experiments. According to the above stated classification, the diffusion kinetics of the ingressing solvents are expected to be Case I or Fickian. Under these circumstances, the diffusion kinetics are described by Fick's first law:

$$J = -D \frac{\partial C}{\partial x} \quad (3.9)$$

where J is the flux i.e. the mass passing through unit area per unit time, D is the diffusion coefficient and x is the diffusion distance. In the case of one-dimensional diffusion, this can be converted into a time-dependent differential equation, Fick's second law:

$$\frac{\partial C}{\partial t} = D \frac{\partial^2 C}{\partial x^2} \quad (3.10)$$

In the ideal case of a semi-infinite sheet and assuming that D is independent of concentration, the solution is obtained by Crank:⁶³

$$C = C_0 \operatorname{erfc} \frac{x}{2(Dt)^{1/2}} \quad (3.11)$$

where C_0 is the surface concentration and $\operatorname{erfc}(x)$ is the error function complement. Lapcik et al.⁶⁴ obtained an expression for the distance x of the diffusion front to the 'original' surface of the polymer:

$$x = \sqrt{2Dt} \quad (3.12)$$

Chapter 3

In general, however, the diffusion coefficient for polymer-solvent systems can be concentration-dependent due to the plasticizing effect and usually has the form:

$$D = D_0 \exp(\gamma C) \quad (3.13)$$

where D_0 is the diffusion coefficient corresponding to the maximum surface concentration C_0 and γ the concentration coefficient related to the fractional volume (or molecular mobility) and the polymer-penetrant system.⁶⁵ However, it is generally accepted in literature that the concentration-dependence of the diffusion coefficient is rather low at temperatures above T_g ^{53a,64} and, as a consequence, that the diffusion coefficient can be considered as a constant value (ideal Fickian diffusion).

The time dependence of the diffusion distance can be expressed as:

$$\text{diffusion distance} \sim (\text{time})^n \quad (3.14)$$

or

$$\log(\text{diffusion distance}) \sim n * \log(\text{time}) \quad (3.15)$$

where n theoretically lies between 0.5 for pure Fickian diffusion and 1.0 for pure Case II diffusion. The anomalous diffusion shows an intermediate n value.

b) Experimental determination of the diffusion parameters n and D

The diffusion of cyclohexane into the polyisobutylene-based elastomers with a different cross-link density is studied by means of MRI. For this purpose, cylindrical samples with a diameter of 9.5 mm and a height of 2 mm were cut out of a rubber sheet, placed in the MRI tube and immersed in cyclohexane at ambient temperature. The cylindrical axis was laid along the direction of the main magnetic field (z-direction) so that the radial diffusion into the cylinder (xy-plane) could be imaged. A Teflon stopper was placed on top of the cylinder to avoid longitudinal solvent ingress. Figure 3.13 presents some MRI images of the diffusion of cyclohexane in an unfilled 1,6-hexamethylenediamine cured PIB cylinder as a function of time. The surrounding free solvent, having a different

relaxation time than the imbibed solvent, can be easily distinguished from the ingressed solvent. Two different processes can clearly be discriminated: solvent penetration into the rod and polymer matrix swelling. The diffusion front of the ingressing solvent can easily be distinguished from the unswollen inner core. Some dark circular spots, which can be assigned to voids, are also visible in these solvent MRI images. These diffusion experiments are performed for all four unfilled 1,6-hexamethylenediamine cured elastomers having a different degree of cure.

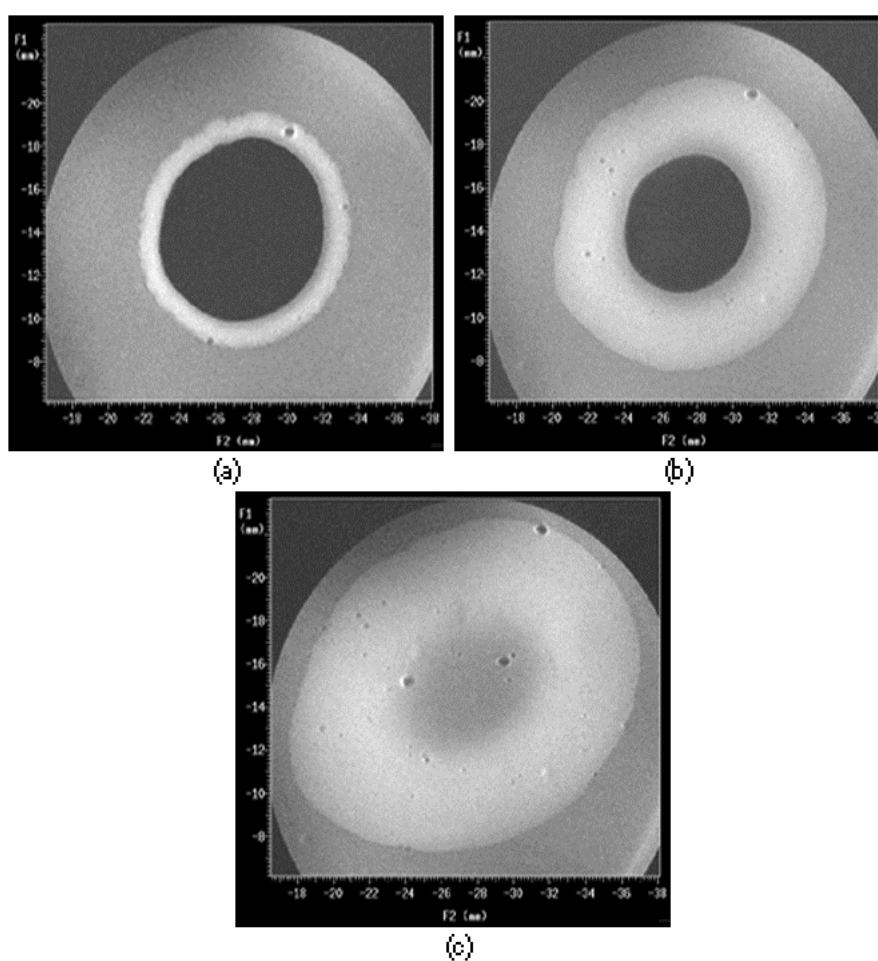


Figure 3.13: MRI images of the diffusion of cyclohexane in the unfilled 1,6-hexamethylenediamine cured PIB elastomer 2 as a function of time: (a) after 45 min, (b) after 6 h 16 min and (c) after 18 h 40 min.

Chapter 3

Since the solvent swells the polymer, the distance covered by the penetrant or moved by the diffusion front is calculated based on the unswollen dimensions of the sample and the remaining core by means of equation 3.16 (schematic presentation of the diffusion process in Figure 3.14). The diameter of the core presents the diameter of the unswollen remaining central part. Because of the inhomogeneous swelling of these elastomer samples, the mean core diameter was calculated out of the area (πr^2) of the central unswollen core. This was obtained by using the public domain 'NIH-image' program (developed at the U.S. National Institutes of Health) on a Macintosh computer.

$$\text{diffusion distance} = \frac{\text{original diameter} - \text{diameter core}}{2} \quad (3.16)$$

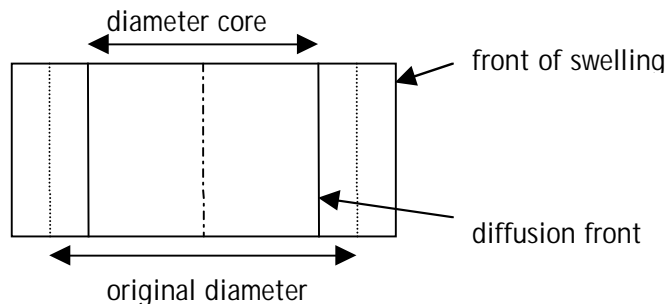


Figure 3.14: Schematic presentation of the diffusion process in a cylinder.

By plotting the logarithm of the diffusion distance (eq. 3.16) as a function of the logarithm of time, the parameter n is obtained (eq. 3.15). The value of n lies, within experimental error, close to the theoretical value of 0.5 indicating a quasi Fickian diffusion behavior for all four elastomers. Indeed, since the diffusion experiments are performed above the T_g of polyisobutylene, the polymer is in the rubbery state and the solvent ingress is under diffusion control (Case I or Fickian) instead of under relaxation control (Case II).^{56,63} This permits to extract the diffusion coefficients by plotting the diffusion distance as a function of square root of time (Figure 3.15) and by using equation 3.12. The results are presented in Table 3.7.

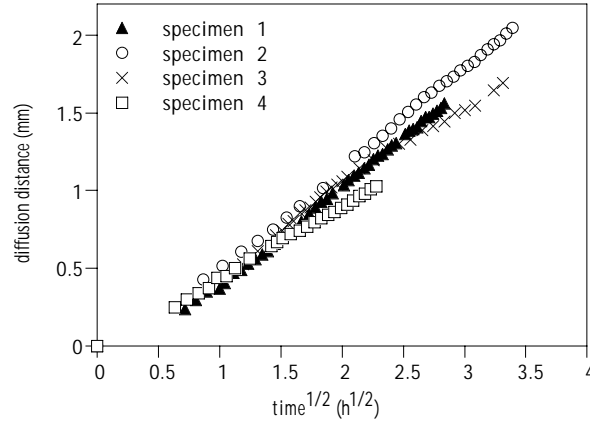


Figure 3.15: Diffusion distance as a function of square root of time for unfilled 1,6-hexamethylenediamine cured PIB elastomers with different cure state.

Table 3.7: Diffusion kinetic parameters for the diffusion of cyclohexane in the unfilled 1,6-hexamethylenediamine cured PIB elastomers.

	elastomer 1	elastomer 2	elastomer 3	elastomer 4
$M_{n,eff}^b$ (g/mole)	56954	52821	26641	7337
$T_{2,mfw}$ (ms) ^a	63.6	54.9	32.0	12.0
n	0.56	0.56	0.52	0.54
D (cm ² /s)	5.29×10^{-7}	5.54×10^{-7}	3.76×10^{-7}	2.95×10^{-7}
Q_{∞} (mole %)	10.96	10.54	7.45	3.90

^a $T_{2,mfw}$ represents the molar fraction weighted volume-averaged T_2 decay time.

Another method to evaluate a sorption experiment can be found in the mass gain, expressed as the number of moles of solvent sorbed by 100 g of polymer at time t (i.e. Q_t in mole %) and presented by equation 3.17.⁴⁶ⁱ

$$Q_t = \frac{\Delta W(t)/M_r(s)}{W_0} \times 100 \quad (3.17)$$

where $\Delta W(t)$ is the mass of the absorbed solvent at time t , $M_r(s)$ is the relative molecular mass of the solvent and W_0 is the initial mass of the dry polymer

sample. At equilibrium, Q_t is taken as Q_∞ i.e. the mole % uptake at infinite time. The results are presented in Table 3.7 for the different elastomers.

c) Correlation with the cross-link density

The sorption behavior of rubbery polymers is controlled by the polymer structure, cross-link density, type of solvent and temperature.^{46k} Since all experiments are performed on the same type of elastomer (unfilled 1,6-hexamethylenediamine cured PIB elastomers), at ambient temperature and with the same solvent (cyclohexane), the variations in sorption behavior will only depend on differences in degree of curing of the elastomers. The results in Table 3.7 already indicate a decreasing ingress rate with increasing cross-link density. Also the equilibrium solvent mass uptake decreases with increasing cure state.

Figure 3.16 shows a plot of the volume-averaged molar fraction weighted T_2 decay time ($T_{2,mfw}$) versus the diffusion coefficient D for the different PIB elastomers. It is clear that the diffusion coefficient increases quasi linearly with increasing $T_{2,mfw}$ or decreasing cure state and this linear relation is expressed by equation 3.18 (R = correlation coefficient):

$$T_{2,mfw} = -38.03 + 17.93 \times 10^7 D \quad (R = 0.956) \quad (3.18)$$

This is in agreement with literature where it is generally accepted that the diffusion coefficient increases approximately linearly with decreasing cross-link density for non-crystalline polymers.⁶⁶ The results demonstrate that this even seems to be the case for rather inhomogeneous elastomers as in our study. On the other hand, the diffusion coefficient obtained for elastomer 1 is somewhat smaller than expected on the basis of the volume-averaged $T_{2,mfw}$ and $M_{n,eff}^b$. This is probably because of an unfavorable mixing process, resulting in the rather pronounced heterogeneous network structure (Figure 3.8). The strength of MRI lies in the possibility to visualize these inhomogeneities.

Furthermore, the linear relationship between the bulk $T_{2,mfw}$ and the diffusion coefficient (Figure 3.16 and eq. 3.18) can also be used to estimate the spatially dependent values of the diffusion coefficient in inhomogeneous elastomers based on the local $T_{2,mfw}^l$ decay times presented in Tables 3.3 to 3.6 (results not shown).

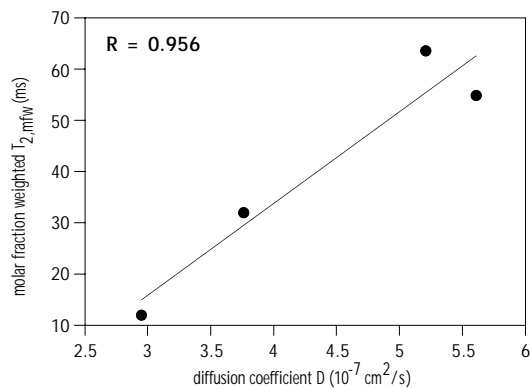


Figure 3.16: Plot of the volume-averaged molar fraction weighted T_2 relaxation time ($T_{2,mfw}$) as a function of the diffusion coefficient D ($R =$ correlation coefficient).

3.4.2.3. Conclusion

MRI images, recorded as a function of time, are used to follow the ingress of cyclohexane in four unfilled 1,6-hexamethylenediamine cured PIB elastomers, all having a different cross-link density. An analysis of these MRI images by using the computer program 'NIH image', results in a value of n of about 0.5, indicating a Fickian diffusion regime. It is observed that both the diffusion coefficient and the equilibrium amount of solvent uptake are inversely proportionate to the cure state: diffusion is much faster in an elastomer sample with a lower cross-link density. Indeed, the higher number of effective cross-links in the higher cure states hinders the molecular motion of the ingressing solvent molecules. Consequently, the penetration rate of the solvent is delayed and the amount of absorbed solvent is reduced.

3.4.3. Conclusion and summary

In this section, a combination of gravimetric Flory-Rehner results and MRI experiments is used to study the spatially dependent degree of cross-linking in unfilled 1,6-hexamethylenediamine cured PIB-based elastomers. MRI relaxometry reveals two proton T_2 relaxation decay times in CCl_4 -swollen

Chapter 3

elastomers: a fast decaying component $T_{2,s}$, reflecting the constrained chain segments near the cross-links and entanglements, and a slow decaying component $T_{2,l}$, originating from less constrained chains further removed from the cross-links. Furthermore, on the basis of the linear relation between the bulk Flory-Rehner cross-link density $M_{n,eff}^b$ and the volume-averaged T_2 decay times, MRI allows the determination of the local cross-link density in inhomogeneously cross-linked elastomers by means of the spatially dependent T_2 decay times.

MRI solvent diffusion experiments reveal a quasi Fickian ingress kinetics of cyclohexane in the unfilled 1,6-hexamethylenediamine cured elastomers and an inverse linear relation between the cross-link density and the diffusion coefficient D as well as with the equilibrium mass uptake.

These results clearly demonstrate that the MRI imaging method is applicable for studying the volume-averaged as well as the local molecular mobility of elastomer networks and for the swelling behavior of (unfilled) elastomers with different cure states. It complements the results of the macroscopic swelling measurements with more detailed information on the rubber-solvent interactions at the molecular level.

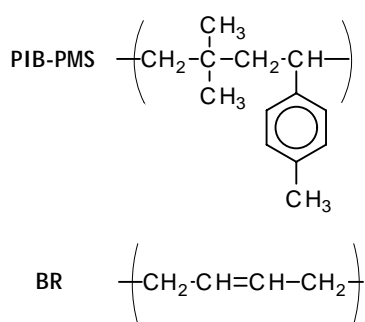
3.5. MRI study of a PIB-PMS/polybutadiene blend

3.5.1. Introduction

The PIB-PMS/BrPMS elastomer can also be used as a component in a blend with polybutadiene (BR). Upon blending these two rubbers, a superior network is formed that exhibits improved mechanical properties with respect to those of the constituting components. These blends are commonly used in sidewall applications, imparting an excellent ozone and flex cracking resistance, as well as non-staining characteristics. A decisive processing step involves the homogeneous mixing of the polymeric blend components, since this has a direct effect on the properties of the blend. Chemical shift selective imaging provides an avenue for selectively interrogating the nature and distribution of defects and mixing inhomogeneities in these blends by either imaging aliphatic hydrogenous of the PIB-PMS component or olefinic hydrogen's of the polybutadiene fraction.^{32c}

3.5.2. MRI images of a swollen PIB/polybutadiene blend

The chemical structure of the two constitutive rubber components of the PIB/BR blend are presented in Scheme 3.2, while the ¹H spectrum acquired with the imaging probe of a CCl₄-swollen carbon-black filled blend is shown in Figure 3.17.



Scheme 3.2: Composition of the PIB/polybutadiene blend.

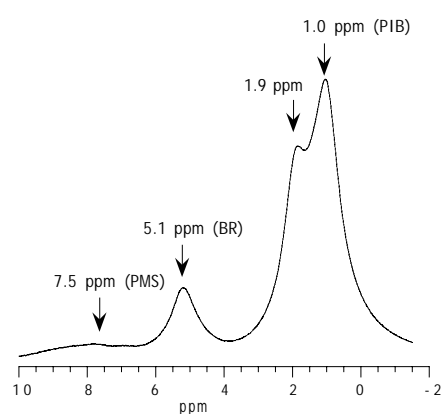


Figure 3.17: ¹H spectrum, of a PIB/polybutadiene blend, swollen in CCl₄.

Chapter 3

The aliphatic signals of the PIB are detected at 1.0 ppm (Me: $T_2 = 0.2$ s) and 1.9 ppm (CH_2 : $T_2 = 0.5$ s). The latter overlaps with the aliphatic signal of BR. The olefinic hydrogen's of BR are resolved at 5.1 ppm ($T_2 = 1.1$ s). The intensity of the aliphatic signals of PMS can be neglected with respect to the aliphatic signals of PIB and BR. Applying chemical shift selective MRI makes it possible to selectively image either the PIB-PMS component or the polybutadiene component and the images are presented in Figure 3.18.

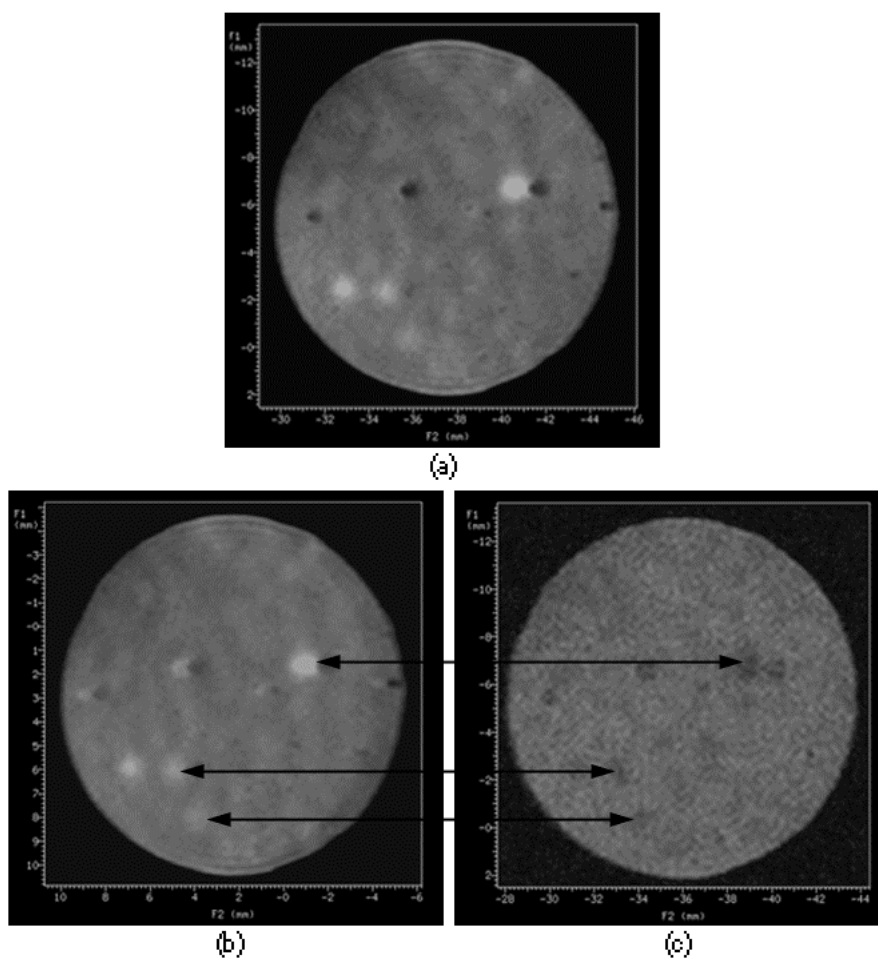


Figure 3.18: MRI polymer images of a cured and carbon-black filled PIB-PMS/polybutadiene blend, swollen in CCl_4 : (a) total ^1H image, (b) chemical shift selective image of the aliphatic components, (c) chemical shift selective image of the olefinic component.

Figure 3.18a shows the total ^1H image of the PIB-PMS/polybutadiene blend, which is cured and filled with carbon-black. In this image, the overall resolution and contrast are necessarily poor due to multiple signal excitation. Shown in Figure 3.18b is the aliphatic image (selective excitation around 1.5 ppm) of both components in the blend. A significant observation is the presence of several clear regions, which appear as dark regions in the olefinic image (Figure 3.18c) of polybutadiene (selective excitation around 5.1 ppm). Given that these regions exhibit a strong signal in the aliphatic image and a weak signal in the olefinic image, we can conclude that these regions arise from badly mixed and thus, consequently, undercured highly mobile PIB-PMS chains.

We rule out oil (present at a level of 9-11 wt%) as the cause of these clear domains in the aliphatic image since no sharp peak is observed in the ^1H spectrum and furthermore, the image is unchanged after a cycle of swelling, drying, and reswelling. This would certainly lead to an extraction of the dispersed oil. The mixing procedure used to prepare this compound clearly does not result in a homogeneous distribution of the polymer components in the blend.

3.5.3. Conclusion

The previous results show that chemical shift selective MRI images of the polymer spins can be used to selectively visualize the different components in a polymer blend. A prerequisite is that the chemical shift dispersion between the signals of the different components is large enough to allow selective excitation. In the example presented above, the chemical shift selective polymer images show that the mixing procedure with the production of the blend was not optimal.

3.6. Demonstration and assignment of voids in carbon-black filled PIB elastomers

3.6.1. Introduction

In the previous sections, the solvent MRI images clearly revealed the presence of some dark circular spots, containing no signal from the solvent nor from the polymer. These black spots are not originating from the filler (inhomogeneous dispersion of carbon-black) nor from poorly dispersed regions of ZnO (e.g. ZnO agglomerates) because they appear both in unfilled elastomers cured with an organic curative (1,6-hexamethylenediamine) and in an unfilled ZnO cured PIB elastomer. Since the amount of curative or catalyst is too small to account for the area occupied by these spots and due to the regular spherical shape of the spots, it is very unlikely that they arise from regions of higher cross-link density (T_2 too short to detect). So these spots can be assigned to voids and are probably incorporated in the polymer matrix during processing as a result from the low inherent diffusivity of gases in PIB. Surface tension prevents the solvent from entering the void. Although the presence of voids in elastomers has already been quoted in literature,³³ there is still need for a straightforward assignment of the presence of voids in PIB elastomers.

In the next section, MRI experiments on dry and swollen (carbon-black filled) PIB elastomers, solid state NMR relaxation data, SEM measurements and XRMT images are presented to assign the dark circular spots in the MRI images to voids in the PIB elastomers.

3.6.2. Solvent images of PIB elastomers

3.6.2.1. Swelling and reswelling experiments of a carbon-black filled PIB elastomer

Figure 3.19a shows the chemical shift selective solvent image for a cured carbon-black filled PIB-PMS/BrPMS elastomer swollen in benzene. Despite the carbon-black filling, it is still possible to obtain good quality images. This particular sample exhibits a large number of dark circular spots, the larger of

which are partially surrounded by a crescent-shaped bright intensity ring. This is due to magnetic susceptibility artifacts in the readout direction, which originate at an interface. E.g. at the air/polymer interface, this susceptibility gradient is rather large.⁴²

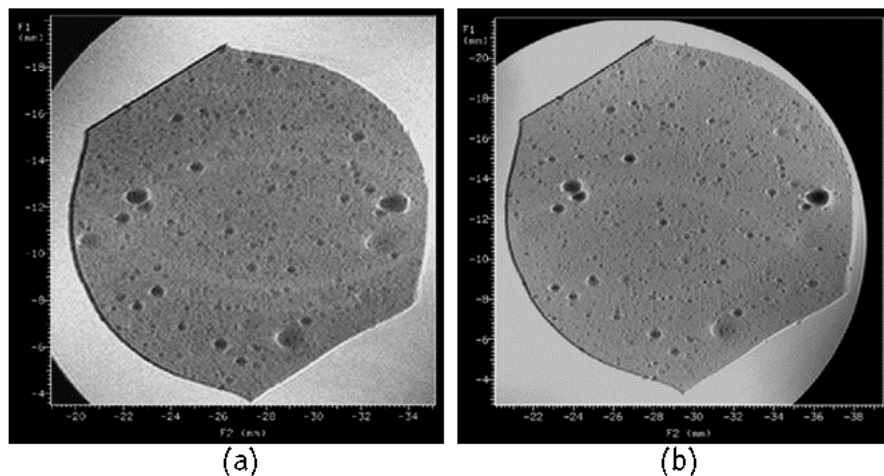


Figure 3.19: Solvent MRI images of a cured carbon-black filled PIB-PMS/BrPMS elastomer swollen in (a) benzene and (b) cyclohexane.

The image in Figure 3.19b was obtained after the solvent was removed from the slice shown in Figure 3.19a. The sample was dried and reswollen in cyclohexane. Both images are quasi identical: the cyclohexane solvent image shows the same voids at the same positions and of the same dimensions as in the original benzene image. This confirms that the voids are inherent in the polymer matrix and do not arise as an artifact from the swelling process (e.g. entrapped air in the solvent). This is further confirmed by an MRI diffusion study of cyclohexane and CCl_4 in an unfilled PIB elastomer: the voids, visible in the solvent and polymer images, respectively, do not migrate together with the solvent but remain stationary in the polymer matrix.

3.6.2.2. Solvent MRI images recorded with a short echo time and at higher temperature

MRI images were recorded with a short echo time (TE) in order to eliminate the possibility that the dark circular spots originate from local regions of higher cross-link density. The previous T_2 relaxation time measurements (section 3.4.1.) already showed that the shortest T_2 value (i.e. corresponding to the most restricted chain segments) for a CCl_4 -swollen elastomer is about 6 ms at room temperature. MRI rubber images, recorded with a short echo time of 4.75 ms, must visualize about 45% of the proton signal of these highly restricted chains (eq. 3.19).

$$M_t/M_0 = \exp\left(-TE/T_2\right) \quad (3.19)$$

Furthermore, when such MRI images are obtained at elevated temperature, the mobility of the polymer chains is increased even more and a higher percentage of the proton spins should be detected.

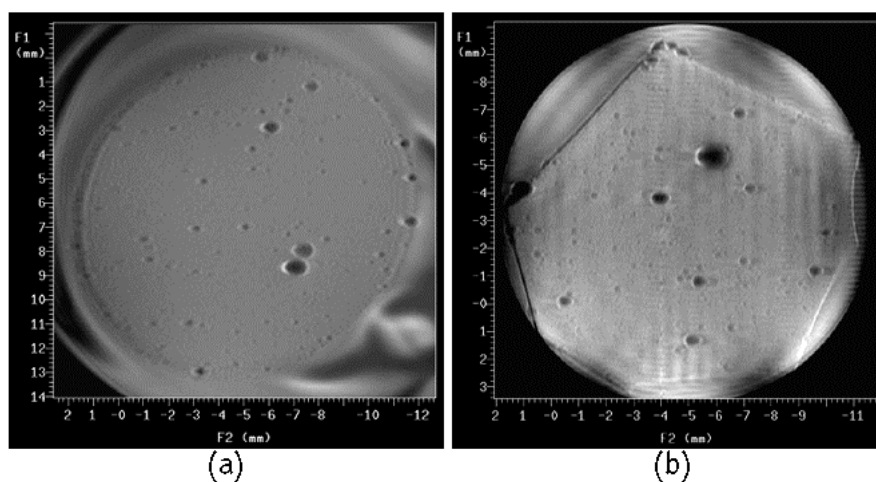


Figure 3.20: Solvent MRI images of unfilled PIB elastomers swollen in cyclohexane: (a) recorded with $TE = 4.75$ ms at 50 °C, (b) recorded with $TE = 1.9$ ms at room temperature (different sample).

Figure 3.20a presents the MRI image of a cyclohexane-swollen PIB elastomer, acquired with TE = 4.75 ms at 50 °C. Under these experimental conditions, higher cross-linked elastomer chains must certainly be detectable. However, the dark circular spots clearly remain present with the same shape and at the same locations. When MRI images are recorded with an even shorter echo time of 1.9 ms for which about 73% of the restricted chains should be detected, the black spots still remain present (Figure 3.20b).

Also when swelling is performed at ambient temperature in THF with chromium(III)acetylacetonate ($\text{Cr}(\text{acac})_3$ is added to shorten the T_1 relaxation time of the possible highly immobilized chains and consequently to increase its signal intensity), the black spots clearly remain present.

3.6.2.3. Three-dimensional reconstruction

In order to verify the spherical shape of the voids, a three-dimensional image reconstruction was performed. For this purpose, several consecutive transverse slices with a thickness of 150 μm were recorded of a cyclohexane-swollen, carbon-black filled PIB elastomer cylinder by means a multi-slice pulse sequence. Parts a, b and c in the left part of Figure 3.21 show a top, central and bottom 150 μm slice, respectively. All transverse images were stacked on top of each other to reconstruct the three-dimensional cylinder by using the imaging analysis computer program obtained from the National Institute of Health ('NIH-image'). This program further allows visualizing slices in any direction of the reconstructed cylinder. Some longitudinal slices (from top to bottom in the transverse images) derived from the reconstructed cylinder are presented at the right part (d) of Figure 3.21.

The combination of transverse slices (Figure 3.21a-c) and longitudinal slices (Figure 3.21d) further confirms that the black spots are indeed spherically shaped, excluding the possibility that they can be ascribed to regions with a high cross-link density. Consequently, these spots are assigned to voids or 'air bubbles', occluded in the polymer matrix during processing. This three-dimensional reconstruction also illustrates the power of MRI to acquire very accurately consecutive slices of a three-dimensional object.

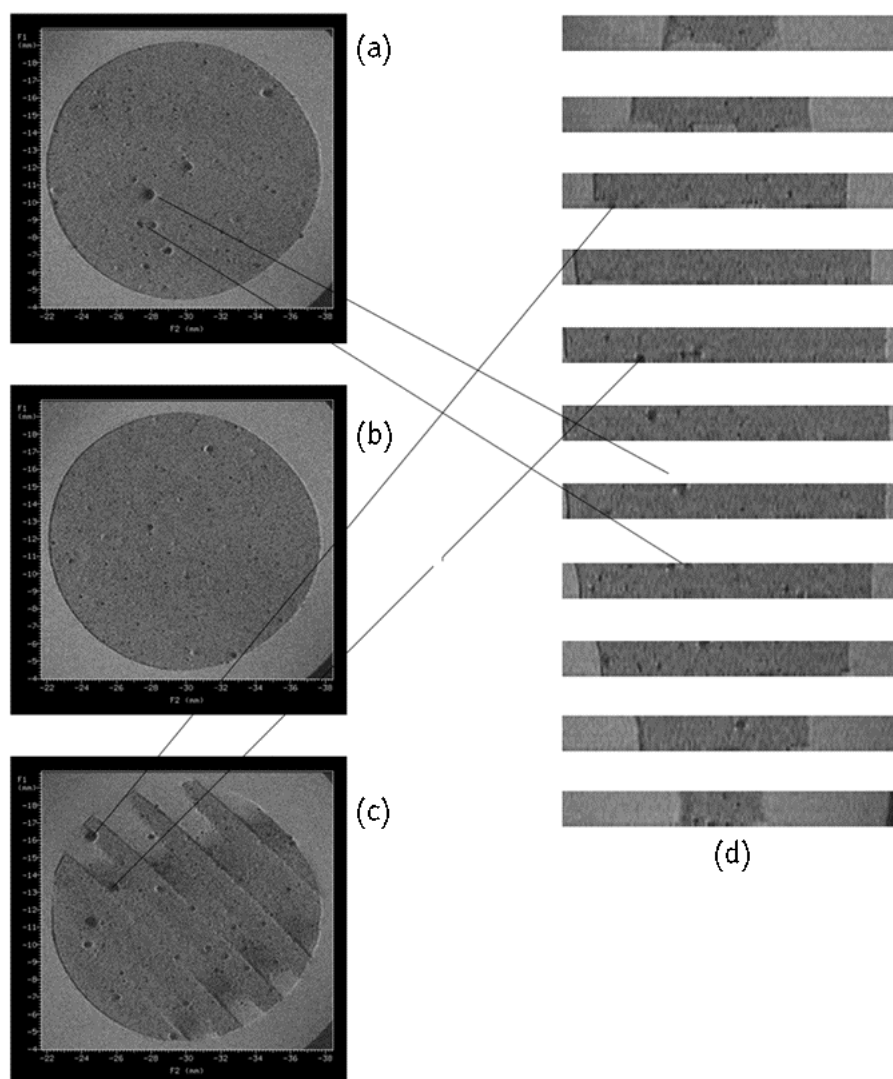


Figure 3.21: Three-dimensional reconstruction of a carbon-black filled PIB-PMS/BrPMS elastomer swollen in cyclohexane. Transverse 150 μm slices are shown of (a) a top slice, (b) a central slice and (c) a bottom slice. All transverse slices are stacked to reconstruct a 3-D matrix from which the longitudinal slices, of which some are presented in (d), are derived.

3.6.3. MRI images of unswollen PIB elastomers

3.6.3.1. Comparison of MRI images of a PIB elastomer before and after swelling

As previously mentioned, the chain dynamics for polyisobutylene are significantly reduced due to the steric constraints associated with interchain packing of the methyl groups.⁴¹ So imaging of the solid-like material at ambient temperature becomes difficult with the classical MRI hardware because of the broad line width, caused by strong proton-proton dipolar interactions and non-averaged by molecular dynamics. One option to circumvent this issue is previously presented, namely a reduction of the correlation time for chain reorientation by swelling the sample in appropriate solvents. A second procedure to increase the chain dynamics (and T_2) is to perform MRI experiments at higher temperature (see also Figure 3.1). Increasing the temperature (far) above the T_g results in a proton NMR line width, which allows imaging by using the standard MRI techniques and hardware.

Applying this procedure, direct proton images of the polymer spins (in the absence of any swelling solvent) of an unswollen carbon-black filled PIB elastomer were obtained with a short echo time ($TE = 2.15$ ms) and at a temperature of 60 °C (Figure 3.22a). This image unambiguously confirms that the voids are inherent in these elastomers and do not arise from the swelling process.

Figure 3.22b shows a solvent image of the same specimen after swelling in cyclohexane. Though both the solvent and the rubber resonances are imaged simultaneously (resonances of C_6H_{12} and rubber aliphatics overlap in the 1H spectrum), the black spots appear at exactly the same positions (Figure 3.22b) as in the image of the dry rubber (Figure 3.22a). The figure further shows that the dimensions of the spots increase by swelling, which again is an indication that they are not caused by filler or curative. The larger voids are partially surrounded by bright crescent-shaped intensity rings, ascribed to differences in magnetic susceptibility at the air/polymer interface.⁴² These results demonstrate that, for elastomers with T_2 relaxation times too short to prohibit straightforward acquisition, representative data may be extracted after solvent swelling.

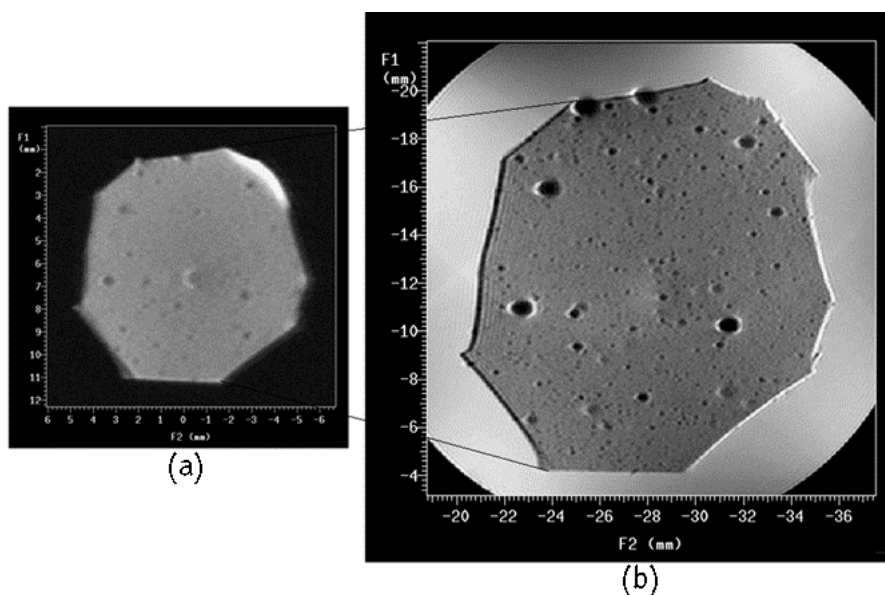


Figure 3.22: MRI images of a commercial carbon-black filled PIB elastomer: (a) dry native state at 60 °C and (b) after swelling in cyclohexane.

Voids can also be detected in native unfilled PIB elastomers. Figure 3.23 presents the MRI image of an unfilled 1,6-hexamethylenediamine cured PIB elastomer, recorded with TE = 1.5 ms and at 70 °C. This image again confirms that the voids also appear in dry unfilled rubbers and that they cannot be attributed to the solvent or filler.

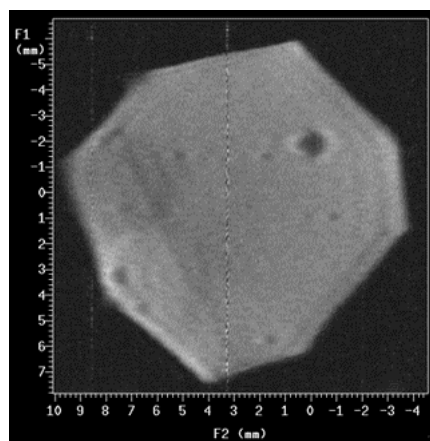


Figure 3.23: MRI image of a native unfilled PIB elastomer (TE = 1.5 ms and at 70 °C).

3.6.3.2. MRI images of a native rubber at different stages of the production process

It was already stated that voids or 'air bubbles' are enclosed in the polymer matrix during processing. Trying to find out in which stage of the rubber production process the voids are induced, an MRI study was performed on carbon-black filled rubber specimens, abstracted from different stages of the production process. Three rubber samples have been studied:

- a. uncured, from the mixer
- b. uncured, after extrusion
- c. after curing

Because the uncured elastomers (a and b) completely crumble by swelling in cyclohexane, it was impossible to obtain solvent MRI images. Therefore MRI images were acquired in the native unswollen state with TE = 2.15 ms and at 60 °C (Figure 3.24a-c). Figure 3.24d presents the solvent MRI image of the cured cyclohexane-swollen elastomer in Figure 3.24c.

Voids are clearly present in the cured elastomers as shown by the native rubber image in Figure 3.24c as well as by the solvent image in Figure 3.24d. Figure 3.24b and 3.24a demonstrate that the voids are already present in the rubber matrix before curing (after extrusion) and even before extrusion (after mixing), respectively. These results indicate that the voids are not induced during the vulcanization process, but that they are already present in the rubber matrix after the mixing process. These results allow presuming that the voids can be considered as 'air bubbles', which are entrapped in the rubber matrix during the mixing process in the mill.

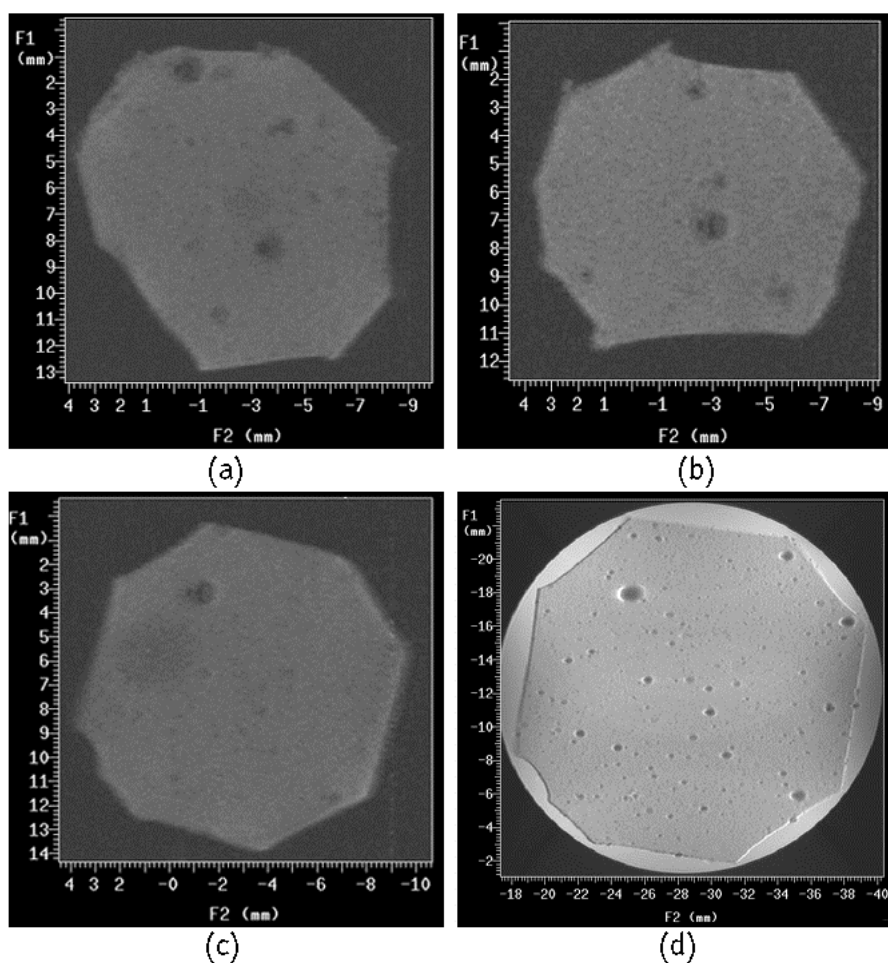


Figure 3.24: MRI images ($TE=2.15\text{ms}$, $60\text{ }^\circ\text{C}$) of a native rubber at different stages of the production process: (a) uncured from the mixer, (b) uncured after extrusion and (c) after curing. For the cured elastomer, a solvent MRI image (C_6H_{12}) is obtained (d).

3.6.4. Solid state NMR relaxometry study of PIB elastomers

3.6.4.1. Introduction

Solid state NMR relaxation experiments were performed to confirm that the dark circular spots in the MRI images could not be ascribed to regions with restricted chain dynamics. As already shown in literature, solid state NMR relaxation time studies can provide unique information concerning the chain

dynamics of polyisobutylene-based copolymers.^{20c} Restrictions of chain motions can result from local chain order stiffening (i.e. regions of higher cure state).^{20a,67} If the dark spots in the MRI images do arise from local sites of higher cross-linking, one should expect differences in the relaxation time behavior of elastomers displaying a different amount of voids.

In this section, two commercial carbon-black filled PIB elastomers were studied which are extreme with respect to the amount of voids. Figure 3.25 shows the solvent MRI images of the cyclohexane-swollen elastomer CB-30 (Figure 3.25a) and CB-330 (Figure 3.25b). The CB-30 elastomer contains a lot more dark spots than CB-330 (CB denotes that the PIB elastomers are filled with carbon-black). The average % area of the slice taken by voids is even 3.5 times larger for CB-30 than for CB-330. The cross-link density of these two elastomers, determined by means of the Flory-Rehner method (section 3.4.1.2.), is in the same range: $M_{n,eff}^b = 3150$ g/mole for CB-30 and 2510 g/mole for CB-330. These rubbers were analyzed by using different solid state NMR relaxation techniques. High resolution ^{13}C CP/MAS and MAS (cross polarization – magic angle spinning) NMR is a useful tool to identify the molecular structure and to characterize the molecular motions based on the different chemical shifts.¹⁹ ^1H wideline NMR on the other hand, is much faster but lacks the chemical shift differentiation.

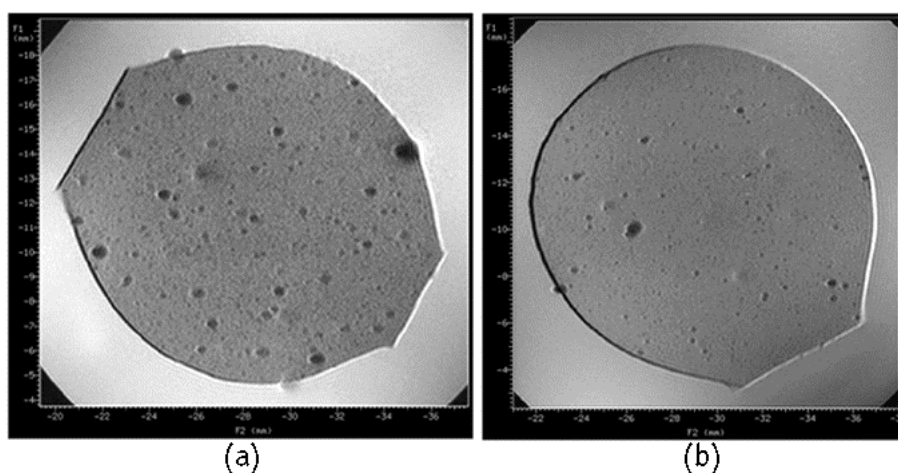


Figure 3.25: Solvent MRI images of carbon-black filled PIB elastomers: (a) elastomer CB-30 and (b) elastomer CB-330, swollen in cyclohexane.

3.6.4.2. High resolution ^{13}C CP/MAS solid state NMR relaxation time study⁶⁸

A direct approach for the molecular characterization of elastomers is the investigation into the chemical structures by means of high resolution solid state ^1H or ^{13}C NMR spectroscopy and relaxometry.²⁰ Since the molecular chain motions are influenced to a great extent by cross-links, the relaxation time behavior should be highly sensitive towards the cross-link density.

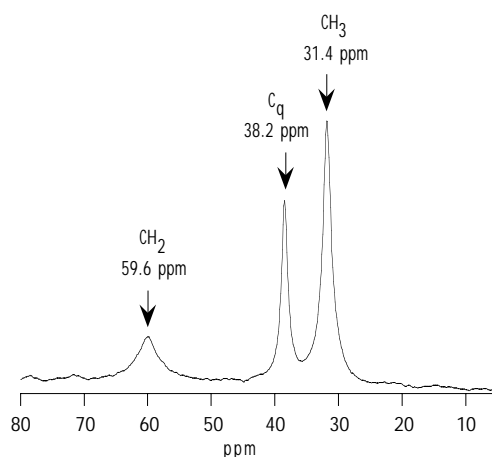


Figure 3.26: ^{13}C NMR MAS spectrum of PIB elastomer CB-30.

Figure 3.26 shows a typical ^{13}C MAS (magic angle spinning) solid state NMR spectrum with the chemical shift assignment of the aliphatic carbon atoms of the carbon-black filled PIB elastomer CB-30.⁶⁹ The amount of p-methylstyrene is rather small (2-3%) and is not further discussed. The carbon spin-lattice relaxation time T_{1c} , which is sensitive to motions in the MHz region, was determined by using the inversion recovery pulse sequence.⁷⁰ The experimental data were analyzed mono-exponentially by means of equation 3.20 and the results are shown in Table 3.8. The short T_{1c} relaxation time of the methyl group can be clearly resolved from the backbone methylene and quaternary carbons due to its high rotational mobility. The T_{1c} results already indicate that the differences between elastomer CB-30 and CB-330 are small and within experimental error.

$$M_t = M_0 \left(1 - 2 \exp\left(-t/T_1\right) \right) + Cte \quad (3.20)$$

The proton spin-lattice relaxation time T_{1H} was determined via a CP/MAS experiment by means of the inversion recovery pulse sequence and equation 3.20. Also the T_{1H} results are comparable for both carbon-black filled elastomers.

The proton spin-lattice relaxation time in the rotating frame $T_{1\rho H}$ (sensitive to motions in the kHz region) and the cross polarization time T_{CH} (time to transfer magnetization from the 1H to the ^{13}C spins) were measured in a contact time study by varying the contact time (T_{CT}) and analyzing the signal intensity by means of equation 3.21. During the contact time, two opposite processes occur simultaneously: a build up of ^{13}C magnetization, characterized by the time constant T_{CH} and a decrease of proton magnetization, typified by $T_{1\rho H}$.

$$M_t = M_0 \left[1 - \exp\left(-T_{CT}/T_{CH}\right) \right] \exp\left(-T_{CT}/T_{1\rho H}\right) \quad (3.21)$$

Table 3.8: ^{13}C MAS and CP/MAS solid state NMR relaxation time results.^a

		elastomer CB-30	elastomer CB-330
T_{1C}	CH_2	$T_{1C} = 0.49 \text{ s} \pm 0.08$	$T_{1C} = 0.59 \text{ s} \pm 0.06$
	C_q	$T_{1C} = 1.95 \text{ s} \pm 0.29$	$T_{1C} = 1.80 \text{ s} \pm 0.25$
	CH_3	$T_{1C} = 0.14 \text{ s} \pm 0.01$	$T_{1C} = 0.14 \text{ s} \pm 0.01$
T_{1H}	CH_2	$T_{1H} = 0.36 \text{ s} \pm 0.03$	$T_{1H} = 0.34 \text{ s} \pm 0.04$
	C_q	$T_{1H} = 0.34 \text{ s} \pm 0.03$	$T_{1H} = 0.35 \text{ s} \pm 0.02$
	CH_3	$T_{1H} = 0.38 \text{ s} \pm 0.02$	$T_{1H} = 0.34 \text{ s} \pm 0.02$
T_{CH}	CH_2	$T_{CH} = 0.20 \text{ ms} \pm 0.01$	$T_{CH} = 0.19 \text{ ms} \pm 0.01$
	C_q	$T_{CH} = 0.36 \text{ ms} \pm 0.02$	$T_{CH} = 0.35 \text{ ms} \pm 0.02$
	CH_3	$T_{CH} = 0.24 \text{ ms} \pm 0.01$	$T_{CH} = 0.25 \text{ ms} \pm 0.01$
$T_{1\rho H}$	CH_2	$T_{1\rho H} = 0.69 \text{ ms} \pm 0.04$	$T_{1\rho H} = 0.71 \text{ ms} \pm 0.05$
	C_q	$T_{1\rho H} = 5.87 \text{ ms} \pm 0.13$	$T_{1\rho H} = 5.33 \text{ ms} \pm 0.15$
	CH_3	$T_{1\rho H} = 3.74 \text{ ms} \pm 0.08$	$T_{1\rho H} = 3.94 \text{ ms} \pm 0.07$

^a Errors indicate the 95% confidence interval of the least squares analyses.

Both T_{CH} and $T_{1\rho H}$ are dependent on the characteristic proton environment, making them different for most of the carbon resonances.⁷¹ If the dark spots in the MRI images should arise from locations with a higher cross-link density, one should expect different T_{CH} and $T_{1\rho H}$ decay times for the CB-30 elastomer compared to CB-330 because of the larger amount of dark spots observed in its MRI image (Figure 3.25a). A comparison of the relaxation times, however, reveals no significant differences between CB-30 and CB-330. As a conclusion, it can be stated that high resolution ^{13}C solid state relaxation results confirm that the dark spots in the MRI images do not result from local sites of higher cross-link density.

3.6.4.3. 1H wideline solid state NMR relaxation time study

1H wideline relaxometry is another valuable solid state NMR technique to study the molecular chain dynamics of the PIB elastomers. No line narrowing techniques are applied, resulting in single broad proton resonance. The disadvantage is that in the broad proton signal all chemical shift information is lost and mostly a multi decay time analysis is required. The advantage of wideline NMR compared to high resolution ^{13}C solid state NMR is that it is a fast technique. For example, a T_2 experiment takes only a few minutes while many hours are needed for a ^{13}C CP/MAS experiment.

1H wideline relaxation experiments were performed on small pieces of dry rubber at 25 °C and 100 °C. The proton spin-lattice relaxation time T_1 is determined with the inversion recovery method⁷⁰ and the evolution of magnetization as a function of the variable time t can be described with equation 3.20. The proton spin-spin relaxation time T_2 is determined by using the solid echo, the Hahn echo and the CPMG pulse sequences. The solid echo (SE) pulse sequence, introduced by Powles et al.,⁷² reduces the effect of the receiver dead time so that short T_2 relaxation times can precisely be measured. To measure the somewhat longer T_2 relaxation times, the Hahn echo pulse sequence⁷³ is better suited. The data were analyzed by using a Weibull function at 25 °C as well as at 100 °C (equation 3.22) and the results are presented in Table 3.9.

$$M_t = M_0 \exp\left[-\left(\frac{t}{T_2}\right)^\alpha\right] \quad (3.22)$$

with $\alpha = 1.01$ at $25\text{ }^\circ\text{C}$ and $\alpha = 1.33$ at $100\text{ }^\circ\text{C}$

The results in Table 3.9 show only minor differences between the relaxation time behavior of both elastomers. There is even some indication that the molecular mobility of the elastomer CB-30 is somewhat higher, which contradicts the presumption that the dark spots in the MRI images result from local regions of higher cross-link density. This is probably related to the somewhat higher value of $M_{n,\text{eff}}^p$. At $100\text{ }^\circ\text{C}$, the T_2 relaxation times increase to such an extent, that we can exclude the possibility that the voids might be ascribed to very high cross-link density regions.

Table 3.9: ^1H wideline solid state NMR relaxation results at $25\text{ }^\circ\text{C}$ and $100\text{ }^\circ\text{C}$.^a

	elastomer CB-30	elastomer CB-330
T = 25 °C		
	$T_1 = 0.34\text{ s}$	$T_1 = 0.33\text{ s}$
SE	$T_2 = 0.08\text{ ms}$	$T_2 = 0.07\text{ ms}$
Hahn	$T_2 = 0.04\text{ ms}$	$T_2 = 0.03\text{ ms}$
T = 100 °C		
	$T_1 = 0.35\text{ s}$	$T_1 = 0.33\text{ s}$
SE	$T_2 = 0.29\text{ ms}$	$T_2 = 0.28\text{ ms}$
Hahn	$T_2 = 0.81\text{ ms}$	$T_2 = 0.72\text{ ms}$

^a The averaged 95% confidence limit is 0.01 s for T_1 and about 0.03 ms for T_2 .

To study the relaxation times of the most mobile parts of the polymer, the pulse sequence of Carr Purcell Meiboom and Gill (CPMG) can be used.⁷⁴ Variable temperature CPMG measurements were already used in literature to demonstrate that PIB elastomers exhibit ^1H T_2 relaxation time behavior, which is sensitive to cure state.^{21a} As a consequence, if the black spots arise from regions of higher cross-link density, the presence of a large number of these spots must have an influence on the T_2 relaxation time behavior. The experiments were performed on small pieces of dry rubber at $25\text{ }^\circ\text{C}$ and at $100\text{ }^\circ\text{C}$. Afterwards, the parts were

Chapter 3

swollen in CCl_4 , excess of solvent was removed and the T_2 decay times were determined. The T_2 magnetization decays were analyzed bi-exponentially according to equation 3.23. The T_1 relaxation times were determined by means of the inversion recovery pulse sequence and the results were analyzed mono-exponentially (eq. 3.20).

$$M_t = M_1 \exp\left(-t/T_{2,s}\right) + M_2 \exp\left(-t/T_{2,l}\right) \quad (3.23)$$

Table 3.10: ^1H CPMG relaxation time results.^a

	elastomer CB-30	elastomer CB-330
T = 25 °C		
	$T_1 = 0.26 \text{ s}$	$T_1 = 0.26 \text{ s}$
	$T_{2,s} = 0.14 \text{ ms}$ (85%)	$T_{2,s} = 0.13 \text{ ms}$ (87%)
	$T_{2,l} = 0.55 \text{ ms}$ (15%)	$T_{2,l} = 0.48 \text{ ms}$ (13%)
T = 100 °C		
	$T_1 = 0.26 \text{ s}$	$T_1 = 0.25 \text{ s}$
	$T_{2,s} = 2.97 \text{ ms}$ (23%)	$T_{2,s} = 2.58 \text{ ms}$ (25%)
	$T_{2,l} = 8.58 \text{ ms}$ (77%)	$T_{2,l} = 7.22 \text{ ms}$ (75%)
After swelling in CCl_4		
	$T_1 = 0.18 \text{ s}$	$T_1 = 0.19 \text{ s}$
	$T_{2,s} = 27.14 \text{ ms}$ (57%)	$T_{2,s} = 29.99 \text{ ms}$ (60%)
	$T_{2,l} = 72.45 \text{ ms}$ (43%)	$T_{2,l} = 70.93 \text{ ms}$ (40%)

^a The averaged 95% confidence limit is 0.01 s for T_1 , 0.01-0.02 ms for T_2 at 25 °C, 0.07-0.12 ms for T_2 at 100 °C and 0.7-5.4 ms for T_2 of the CCl_4 -swollen PIB.

Table 3.10 clearly demonstrates that the T_1 relaxation times as well as the T_2 decay times are comparable within experimental error for both elastomers. It is confirmed that the molecular mobility of the CB-30 elastomer is somewhat higher compared to CB-330, which is probably due to the higher $M_{n,\text{eff}}^b$. Swelling the elastomers augments the molecular chain mobility to such an extent that the T_2

relaxation times are increased even more than by raising the temperature to 100 °C.

For all three experiments, it can be noticed that the T_2 relaxation time for the elastomer CB-30 is even somewhat higher than for CB-330, which rules out the possibility that the dark spots in the MRI images correspond to high cross-link density sites.

3.6.4.4. Conclusions

Different solid state NMR relaxation experiments are performed to verify that the dark circular spots, observed in the MRI images, can not be attributed to high cross-link density regions. In the broad range of molecular motions, covered by the different relaxation decay times, the differences in molecular mobility between the two elastomers are rather small, which allows to conclude that the dark circular spots indeed may be assigned to voids.

3.6.5. Combination of MRI, optical microscopy, SEM and XRMT experiments

To obtain extra confirmation about the presence of voids in the PIB elastomers, some sectioning experiments were performed although it was predicted in literature that this would be difficult, probably because of the elasticity of the rubber matrix.^{30g} Figure 3.27a shows the MRI image of a cyclohexane-swollen carbon-black filled PIB elastomer. A large void is clearly visible at the right top of the image. This sample was cut into two pieces and the large void was split into two parts as could be seen by the naked eye. This is also displayed in the MRI image of Figure 3.27b, showing that the large void is split up into two parts. Although the void is split into two parts, it is surprisingly that the MRI image still demonstrates two almost circular spots on both sides of the sectioned rubber. This is probably caused by the magnetic susceptibility artifacts at the rubber/air interphase.

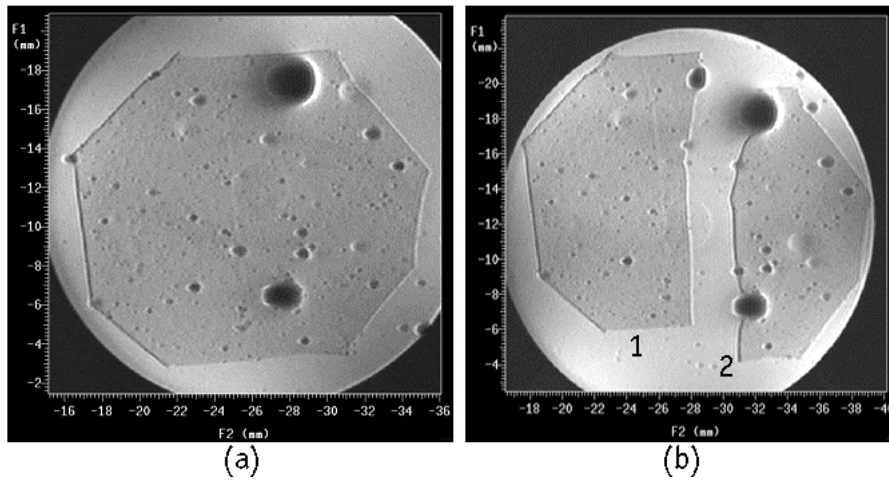


Figure 3.27: MRI images of a cyclohexane-swollen carbon-black filled PIB elastomer (a) before and (b) after cutting the elastomer in two parts.

Figure 3.28a and 3.28b present some optical microscopy images for the rubber parts 1 and 2, respectively. These images confirm that the void is not split proportionally: the cavity in the first rubber part is somewhat smaller and seems less profound than in the second rubber part. The presence of a cavity is also established by means of a profilometer. The accurate depth of the crater, however, could not be measured because of the non-appropriate dimensions of the scanning needle. At higher magnification, some bright spots in the rubber matrix become visible (indicated by arrows in Figure 3.28a), which do not correspond with voids in the MRI images of Figure 3.27.

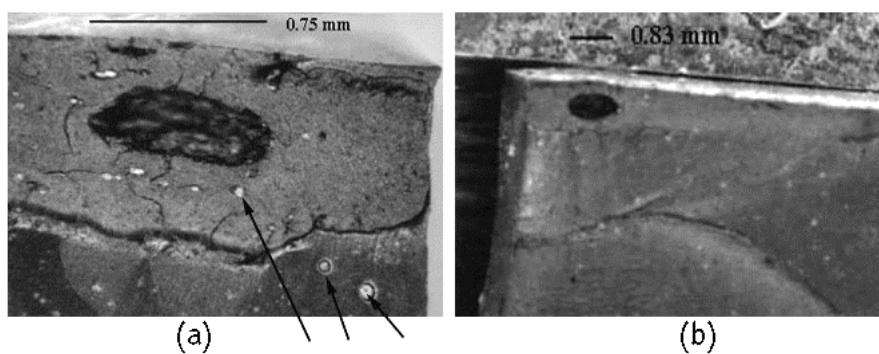


Figure 3.28: Optical microscopy images of (a) the rubber part 1, indicating the left side of the void (magnification 70 \times) and (b) the rubber part 2, indicating the right side of the void (magnification 11 \times).

In order to obtain more information on the chemical composition of the bright spots observed with optical microscopy, scanning electron microscopy (SEM) experiments were performed on both rubber parts. The samples were dried at room temperature to remove the cyclohexane and the surface was coated with carbon. Some SE (scattering electron) and BSE (back scattering electron) images are shown in Figure 3.29 and the elemental analysis is indicated. Since the rubber is completely dried, the dimensions are reduced. These experiments demonstrate that the rubber matrix is mainly composed out of carbon, oxygen, magnesium, silicon, aluminum, and sulfur. The bright spots in the light microscopy and SEM images are caused by larger silicon particles, probably originating from the filler material.

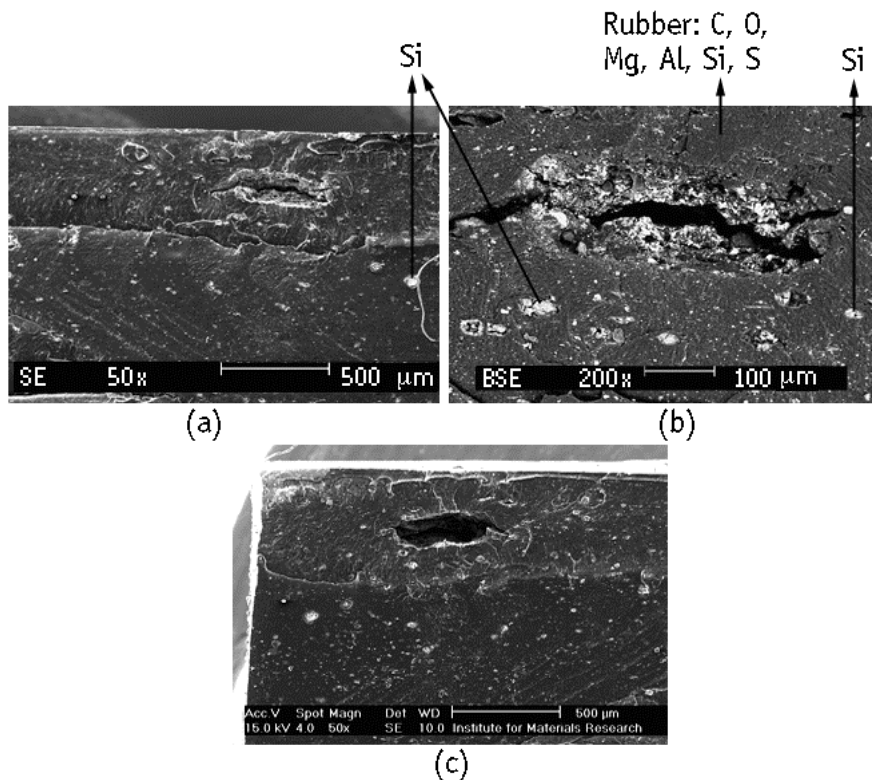


Figure 3.29: SEM micrographs of the dried rubber pieces: (a) SE image of the rubber part 1 (magnification 50×), (b) BSE image of the rubber part 1 (magnification 200×) and (c) SE image of the rubber part 2 (magnification 50×).

Chapter 3

Furthermore, preliminary density experiments were performed on the two carbon-black filled PIB elastomers with a large difference in the number of voids. The results, as the average of ten measurements, are presented in Table 3.11. The elastomer CB-30, containing the largest number of dark spots, displays a somewhat lower rubber density as compared to the CB-330 elastomer.

Table 3.11: Results of the density measurements for the carbon-black filled PIB elastomers with a different number of voids.^a

	CB-30	CB-330
av. no. of voids per cm ² in a 200 μm slice ^a	135 \pm 17	38 \pm 14
M _{n,eff} ^b (g/mole)	3150	2510
density ρ (g/cm ³)	1.1202 \pm 0.0022	1.1299 \pm 0.0045

^a See section 3.7..

Another method to obtain information on the elastomer's interior microstructure is X-ray microtomography or XRMT.¹⁶ X-ray microtomography measures the 3-D profile of the X-ray absorption by recording hundreds of radiographs at small angular increments (total of 180 degrees) by sample rotation. A back-projection computer algorithm converts the data in a 3-D absorption map or image. Conventional X-ray computed tomography, e.g. CAT-scans in medical applications, achieve a spatial resolution in the order of hundreds of microns. Microtomography, on the other hand, obtains a resolution of 20 microns and lower by combining synchrotron radiation with a high resolution X-ray detector.⁷⁵

A comparison between MRI imaging and X-ray microtomography was performed in order to try locating voids and to obtain more information on the material composition. A rubber sample of the CB-30 and CB-330 elastomers were swollen in cyclohexane and solvent MRI images were recorded with a slice thickness of 200 μm . XRMT images were recorded of these samples by Dr. J. H. Dunsmuir (ExxonMobil Research and Engineering, Clinton, New Jersey, USA). Some MRI images and the corresponding high resolution XRMT tomographs (13.6 keV, 200 μm slice thickness) for the CB-30 elastomer are presented in Figure 3.30.

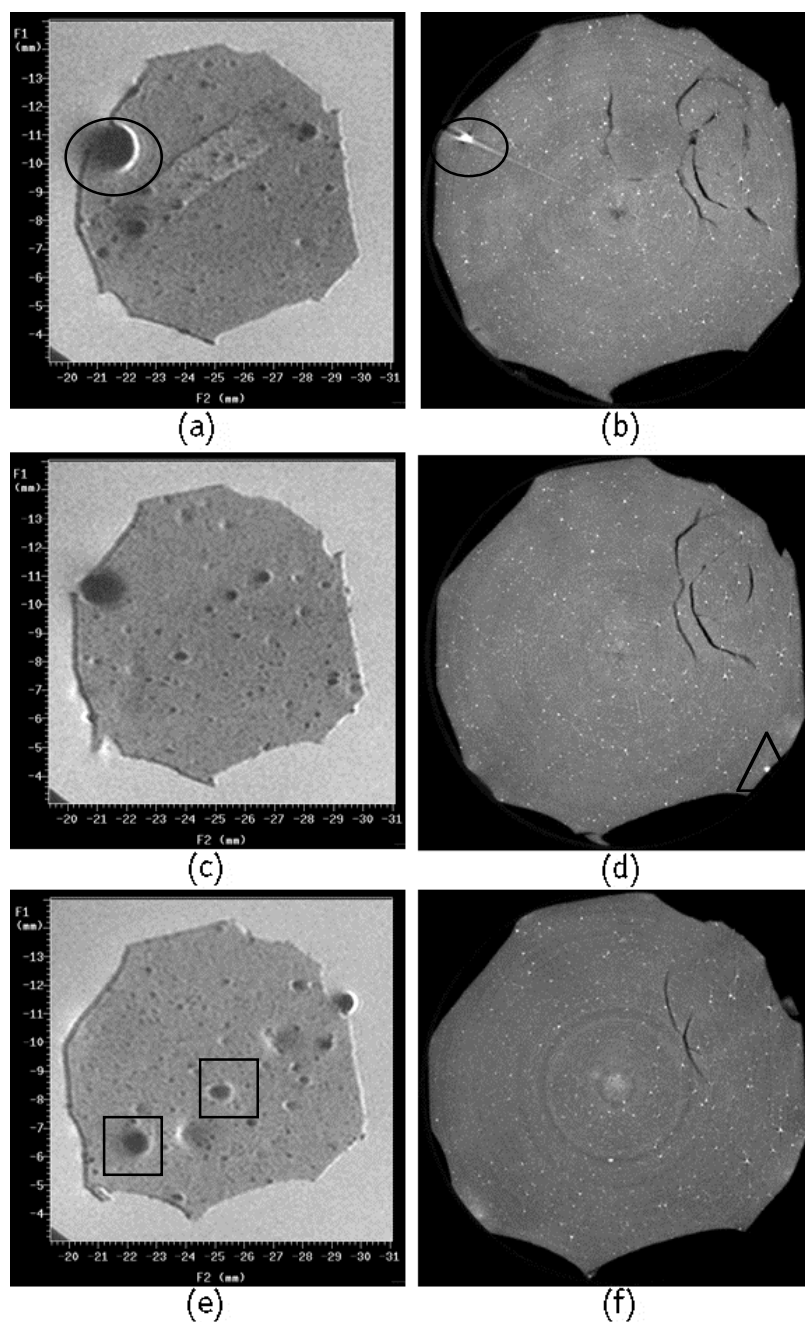


Figure 3.30: Comparison between MRI (a, c and e) and XRMT images (b, d and f) of the elastomer CB-30. Spots marked by a circle appear in both MRI and XRMT pictures, spots marked by a triangle are only visible in the X-ray images and spots marked by a rectangle only appear in the MRI images.

The X-ray images show no spherical voids but a lot of small particles of different sizes (hard particles appear as bright features in the XRMT tomographs). The cracks at the right top of the XRMT images are caused by deterioration of the swollen elastomer during manipulation. Comparing Figure 3.30a and 3.30b, the defects in the XRMT image correspond to a void in the MRI picture. Figure 3.30d shows a feature in the XRMT image (marked by a triangle) but no void in the MRI image of Figure 3.30c. Figure 3.30e on the other hand, presents some voids in the MRI picture (indicated by rectangles) but no corresponding features in the XRMT image (Figure 3.30f). These results demonstrate that only some of the largest voids correlate with features observed in XRMT. However, not all voids detected by MRI correspond to defects in the X-rays tomographs and vice versa. Moreover, XRMT also detects the silicon (Figure 3.29) and other hard particles that are not detected by MRI.

A similar experiment is performed by Dr. J.H. Dunsmuir on the CB-330 elastomer, which contains only a small amount of voids. In this experiment, a low resolution XRMT instrument is used and the comparing MRI and X-ray images are presented in Figure 3.31 (the intensity of the X-ray images is inverted as compared to Figure 3.30). Again there is no significant correlation between the dark circular regions of the MRI images and the features observed in XRMT.

Also these XRMT experiments show that only the larger MRI spots correlate with a defect in the XRMT pictures, so the correlation between MRI and XRMT is not unambiguous. The most spots in the XRMT pictures are probably caused by the presence of the silicon particles or other inorganic material. These results nicely demonstrate that XRMT is a very powerful technique, which is complementary with MRI and which is superior towards the visualization of small and hard inclusions.

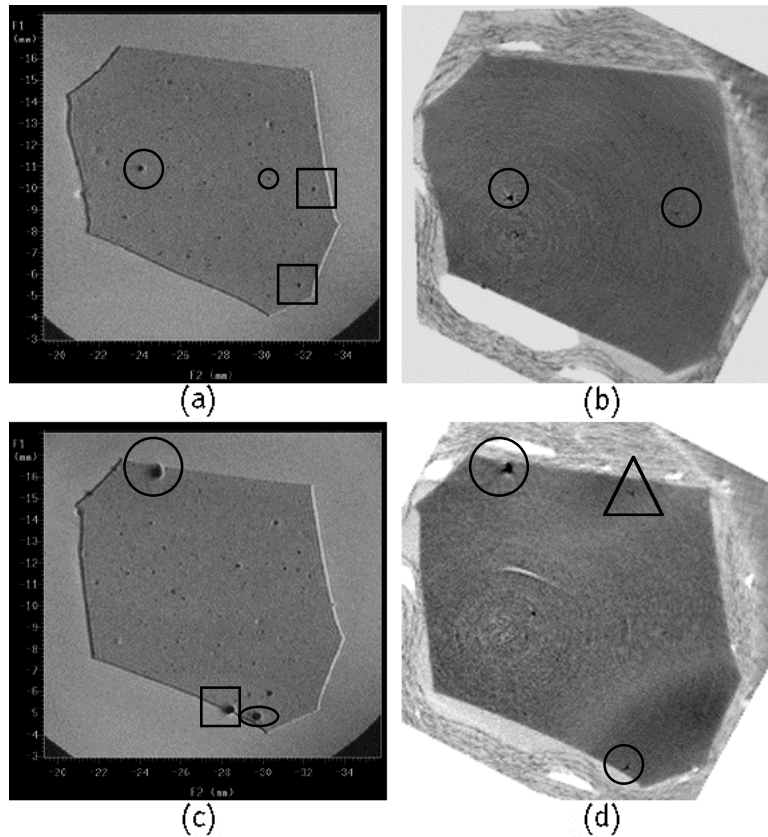


Figure 3.31: Comparison between MRI images (a and c) and XRMT tomographs (b and d) of the CB-330 elastomer. Spots marked with a circle appear in both MRI and XRMT pictures, spots marked by a triangle are only visible in the X-ray images while spots marked with a rectangle only appear in the MRI images.

3.6.6. Conclusions

The above presented experiments demonstrate that the black circular spots, observed in the MRI images, can be attributed to the presence of voids in the rubber matrix. The results and arguments can be summarized as follows:

- the spots are not due to the filler since they also appear in unfilled elastomers;
- the spots do not originate from an inhomogeneous dispersion of curative/catalyst because of their regular spherical shape and because the amount of

Chapter 3

curative/catalyst is too small to account for the area occupied by the black spots;

- the spots are not caused by local regions of higher cross-link density because:
 - ✓ MRI images, recorded at higher temperature and with a short echo time still reveal the black spots;
 - ✓ a three-dimensional analysis visualizes the voids as very regular and spherically shaped;
 - ✓ a solid state NMR relaxation time analysis excludes higher cured polymer regions;
- the spots also appear in the dry unswollen rubber, showing that they are not induced by the swelling solvent but are inherent to the rubber matrix;
- MRI experiments performed on a rubber at different stages of the production process, indicate that the voids are not induced during the vulcanization process but that they are already present in the rubber matrix after mixing and before curing;
- after sectioning, the largest voids can be visualized by using optical microscopy and SEM micrographs.

3.7. MRI study of commercial carbon-black filled PIB elastomers with a different number of voids

3.7.1. Introduction

As already demonstrated in the previous section, isobutylene-based elastomers contain several microvoids as a direct result of entrapped air, resulting from the low inherent diffusivity of gases in PIB. The presence of several of these voids can have a large influence on the physical and mechanical performance of elastomers. In contrast with section 3.4., where a detailed MRI analysis of unfilled PIB elastomers with a different cross-link density is presented, this section will focus on commercial carbon-black filled PIB elastomers with a comparable cross-link density but with a different number of voids. In their practical use in tires, PIB-PMS/BrPMS elastomers are filled with carbon-black. The use of carbon-black as filler in elastomeric networks is a mature technology to improve durability and mechanical properties.

In the first section, a statistical void density analysis and a correlation with the mechanical performance is presented. In the second and third part, the influence of carbon-black loading and voids on the molecular chain mobility and on the diffusion parameters, respectively, is described. In the last part, an MRI study of stress-strain experiments on carbon-black filled PIB elastomers with a different number of voids is presented.

3.7.2. Correlation of the mechanical properties of PIB elastomers with the number of voids: a statistical approach *

3.7.2.1. Introduction

It is already indicated in literature that the presence of voids in elastomers (and other materials) can have an important influence on the mechanical

* A part of this section has been published: Adriaensens, P.; Pollaris, A.; Vanderzande, D.; Gelan, J.; White, J.L.; Kelchtermans, M. *Macromolecules* **2000**, *33*, 7116.

performance of the material.⁷⁶ Therefore a statistical void analysis was performed on six different commercial carbon-black filled PIB-PMS/BrPMS elastomers, all having similar cross-link density but different mechanical performance. So besides the detection of the size and location of voids, MRI will be used to evaluate the distribution of the number and size of the voids over a large sample volume.

3.7.2.2. Comparison of commercial carbon-black filled PIB elastomers with different mechanical performances

The elastomers used in this study are six commercial PIB-based elastomers, which are cross-linked in the presence of ZnO and all filled with a comparable amount of carbon-black. The number-average molecular weight between the effective cross-links ($M_{n,eff}^b$), determined by using the Flory-Rehner equation (section 3.4.1.2.), are rather similar and are presented in Table 3.12.

Table 3.12: Cross-link density and mechanical performance of the six commercial carbon-black loaded PIB elastomers under study.

	$M_{n,eff}^b$ (g/mole)	No. of mechanical stress-heat cycles after which failure occurred
CB-330	2510	330
CB-318	2590	318
CB-211	3180	211
CB-142	3230	142
CB-89	3210	89
CB-30	3150	30

The criterion used to evaluate the mechanical performance is a standard test in which a balloon-type bladder is prepared from the compound and which is pressurized to 1.38 MPa at a temperature of 180 to 200 °C for a hold time of 11 minutes. The bladder balloon was then decompressed to ambient pressure for ca. 1 minute. Some cooling occurs during this time. The number of times this sequence can be carried out before failure is observed is the number of

mechanical stress-heat cycles. Failure is defined as the point at which the bladder compound no longer retains pressure due to air leaks. The mechanical test results for the six different PIB elastomers are also presented in Table 3.12.

Despite the more or less comparable cross-link density, the elastomers clearly perform very differently. Moreover, MRI rubber images of these elastomers demonstrate a very homogeneous network structure (MRI images presented later). This was the starting point to study the influence of voids on the macroscopic performance.

3.7.2.3. Solvent MRI images

A first indication of the relevance of a void density analysis is demonstrated in the NMR images shown in Figure 3.32. Figure 3.32a shows an MRI slice (1 mm thickness) of the elastomer that underwent 330 stress-heat cycles before failure occurred (CB-330). Only a few rather small voids are observed in the image. The slice shown in Figure 3.32b, on the other hand, originates from the elastomer that underwent only 30 cycles before failing (CB-30). The presence of several voids, of which some are quite large, is observed.

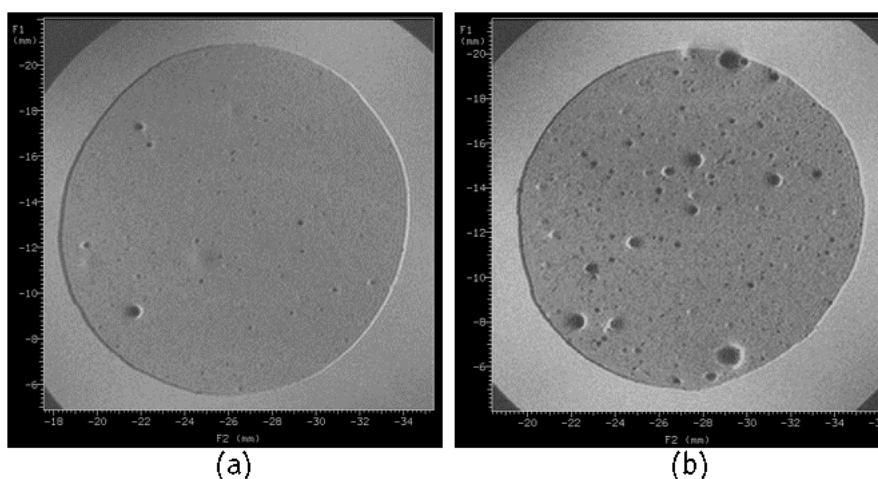


Figure 3.32: Solvent MRI images of carbon-black filled PIB elastomers swollen in cyclohexane. The polymers could resist (a) 330 and (b) 30 mechanical stress-heat cycles before failure occurred.

Visual inspection of these images already indicates that void density seems to correlate with the mechanical performance of these elastomers. It is conceivable that stress/strain forces will concentrate near the voids, leading to (premature) failure of the compound. Previous work by Young et al.⁷⁷ has already indicated that the nucleation of voids is the decisive stage for crack growth in natural rubber/EPDM blends. Therefore a detailed statistical void density analysis was carried out.

3.7.2.4. Statistical image analysis

a) Experimental set-up: MRI imaging of large sample volumes and the statistical analysis of the data

To eliminate local differences in the rubber and to obtain reproducible volume-averaged void density information, the statistical analyses were performed on a large number of slices. For this purpose, three cylindrical samples (with a diameter of 15 mm) of each elastomer type were swollen in cyclohexane and scanned by MRI. For each cylinder, about 25 slices with a slice thickness of 200 μm were recorded by using a multi-slice pulse sequence. So a sample volume of about 2.7 cm^3 was investigated for each rubber type. Such a large sample volume ensures that the statistical conclusions are representative for the bulk material.

The statistical void density analysis was performed on a Macintosh computer by means of a flexible imaging analysis program obtained from the National Institute of Health ('NIH-image'). Several variables were determined for each slice: the number of voids, the diameter of the voids, the number of neighboring voids within an action-radius of 1 mm around each void and the relative area taken by voids. The number of voids per slice was recalculated toward the number of voids per cm^2 to eliminate small differences in sample diameter. These results are finally averaged over all slices of the same rubber type to obtain reproducible, volume-averaged void density information.

b). Results and discussion

The results of the statistical analysis, after averaging over all slices, are presented in Table 3.13 for the six elastomers under study.

Table 3.13: Results of the statistical void density analysis for the six carbon-black filled PIB elastomers under study.^a

no. of stress-heat test cycles before failure	no. of voids per cm ²	diameter of the voids (mm)		no. neighbors within a radius of 1 mm	% area taken by voids
		average	median		
330	38	0.122	0.100	1.612	0.798
	± 14	± 0.092		± 1.573	± 0.397
318	65	0.146	0.110	2.424	2.479
	± 6	± 0.137		± 1.753	± 0.881
211	80	0.143	0.117	3.112	2.432
	± 18	± 0.122		± 2.746	± 0.883
142	110	0.127	0.098	3.302	2.274
	± 8	± 0.100		± 1.992	± 0.524
89	128	0.123	0.102	4.062	2.419
	± 12	± 0.094		± 2.371	± 0.552
30	135	0.131	0.101	4.072	2.850
	± 17	± 0.101		± 2.275	± 0.520

^a Values presented are the arithmetic mean and standard deviation, except for the diameter of the voids where also the median is presented.

The number of voids per cm² shows a quasi normal (Gaussian) distribution with a rather small skewness (< 0.3). This is demonstrated in Figure 3.33a, showing the histogram obtained for the elastomer which underwent 142 stress-heat test cycles. From Figure 3.33b, one can notice a linear relation (correlation coefficient R = 0.972) between the average number of voids per cm² and the number of resisted mechanical stress-heat cycles before failure occurred for the six elastomers under study. While the standard deviation is rather similar for all

elastomers, the coefficient of variation (the ratio between the standard deviation and mean, being a measure of the relative dispersion of the voids over the sample⁷⁸), decreases significantly toward specimens with a high void density. This means that the voids are distributed rather inhomogeneously in samples with superior mechanical properties (small amount of voids). Although a 2-D analysis of 3-D properties has some limitations, e.g. large voids will be detected in several consecutive slices and will be counted more than once, while small voids having similar x-y coordinates in the same slice will be counted only once, a linear correlation is obtained between the number of voids per cm² and the mechanical performance of the elastomers. Since stress/strain forces can concentrate near a void, the presence of a large number of elastomer imperfections will lead to premature failure of the compound.

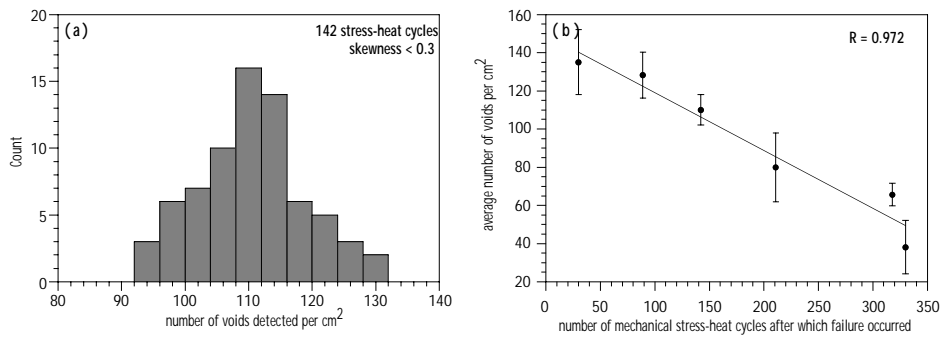


Figure 3.33: Results of the statistical void analysis: (a) histogram of the number of voids detected per cm² for the elastomer CB-142 and (b) average number of voids per cm² as a function of the number of mechanical stress-heat cycle before failure (standard deviation is indicated by error bars).

A similar correlation (correlation coefficient $R = 0.95$) is observed between the mechanical performance and the average number of neighboring voids within a radius of 1 mm, a parameter closely related to the average number of voids per unit area. One notes that the distribution of this parameter exhibit skewness, which increases as a function of decreasing average number of neighbors as already indicated by the coefficient of variation. This is demonstrated in Figure 3.34a and 3.34b, showing the histograms for the elastomers, which underwent 30 and 211 stress-heat cycles, respectively. In addition to a more inhomogeneous distribution of voids in elastomers with superior performance, the skewness of

the histograms also explains the relatively higher standard deviation for the average number of neighbors.

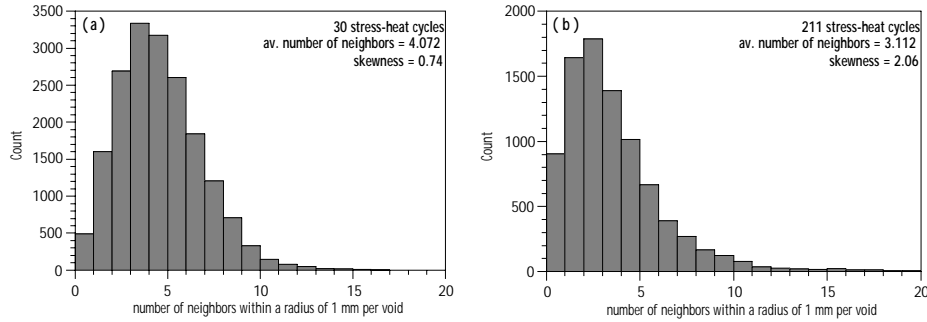


Figure 3.34: Histograms of the number of neighboring voids within a radius of 1 mm for the PIB elastomers (a) CB-30 and (b) CB-211.

Also the distribution of the diameter of the voids shows a rather high degree of positive skewness as can be seen in the histograms of Figure 3.35a and 3.35b. Because of the rather high skewness of this parameter, the average value as well as the median are presented in Table 3.13. Table 3.13 indicates that the diameter of the voids clearly is less decisive in terms of mechanical performance.

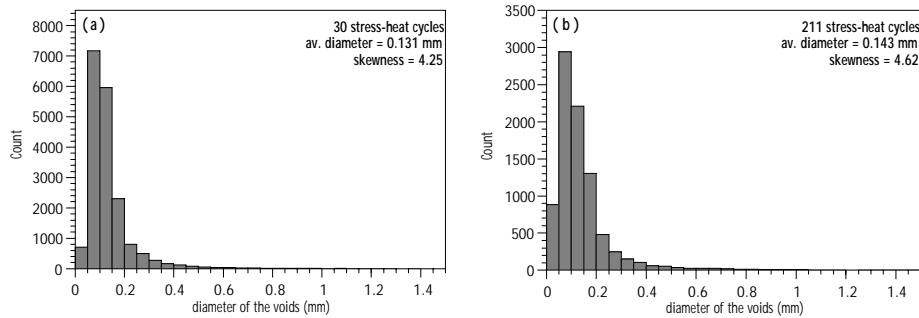


Figure 3.35: Histograms of the diameter of the voids for the PIB elastomers (a) CB-30 and (b) CB-211.

The fourth parameter presented in Table 3.13 is the average area of the slice (in percent) taken by voids, a variable being controlled by the size as well as by the number of voids. Because of severe fluctuations in the void diameter, only a weak correlation with the mechanical performance of the compounds is observed. Notice that the average dimension of the voids in the elastomers which

underwent 211 and 318 stress-heat cycles exceeds the 'normal' void dimension and results in the deviation from linearity in the plot of the average area taken by voids vs. the mechanical performance.

These data show that the number of voids per cm^2 rather than the diameter of the voids strongly determines the mechanical performance of the investigated PIB elastomers and that the presence of a large number of imperfections influences the crack growth.

3.7.2.5. Conclusion

A detailed statistical void density analysis is performed on MRI images of six carbon-black filled PIB elastomers swollen in cyclohexane. All six elastomers have a comparable effective cross-link density. The statistical analysis shows that the average number of microvoids per cm^2 nicely correlates with the mechanical performance of the elastomers: a large number of voids induces a premature failure of the compound. Also the average number of neighboring voids within a radius of 1 mm from the voids is an important parameter, while the diameter of the voids seems to be less decisive.

So these results demonstrate that NMR imaging is an effective and non-destructive method for obtaining void density information.

3.7.3. Determination of the volume-averaged relaxation times for filled PIB elastomers with different number of voids

In order to obtain information on the influence of filler and voids on the molecular chain mobility of the carbon-black filled PIB elastomers, some volume-averaged relaxation time measurements were performed. Only the two extreme samples were studied: the CB-30 elastomer containing the highest number of voids and CB-330 that possesses only a few voids. The samples were swollen in CCl_4 and MRI projections and images of the rubber polymer matrix were recorded. The MRI images of the CCl_4 -swollen samples are displayed in Figure 3.36.

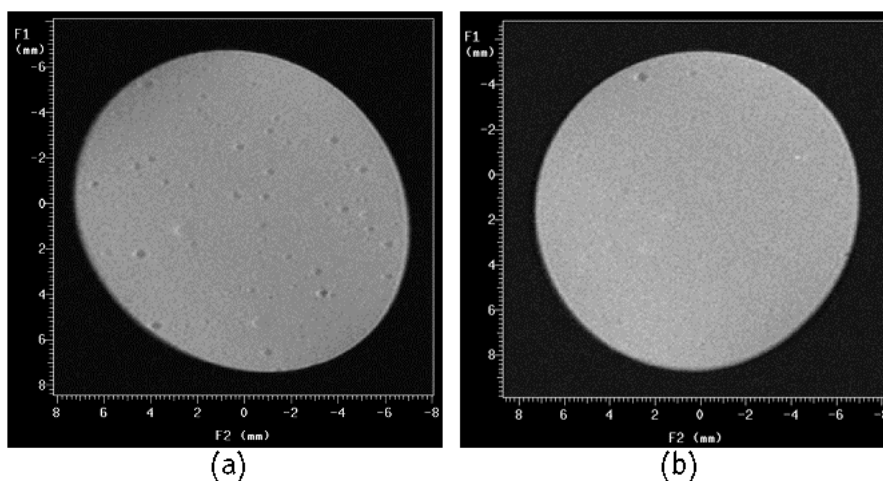


Figure 3.36: MRI rubber images of the CCl_4 -swollen carbon-black filled PIB elastomers (a) CB-30 (135 voids per cm^2) and (b) CB-330 (38 voids per cm^2).

Although rubber images are not optimal to visualize voids, the largest voids do become visible in the rubber images and a clear difference can be noticed concerning the number of voids between CB-30 (Figure 3.36a) and CB-330 (Figure 3.36b). Solvent images of these samples, swollen in cyclohexane, clearly display all voids. These rubber images demonstrate that the network cross-linking of both elastomers is very homogeneous. Although the samples are filled with carbon-black, a good image quality is obtained.

Information on the volume-averaged molecular chain mobility is obtained from T_1 and T_2 relaxation experiments. The T_1 relaxation time was determined by analyzing the 1-D projection intensity versus a variable repetition delay TR according to equation 3.4, while the volume-averaged T_2 relaxation time was obtained by analyzing the spin-echo amplitude of the 1-D spin-echo projections as a function of echo time TE. A bi-exponential analysis (eq. 3.5) results in a short and a long T_2 component ($T_{2,s}$ and $T_{2,l}$ respectively). The short component arises from network chain segments that are constrained by surrounding cross-links and entanglements, while the long T_2 component originates from the more mobile network chains, further removed from the cross-links and entanglements.⁴⁹ By using these bi-exponential results, the molar fraction weighted volume-averaged T_2 relaxation time $T_{2,mfw}$ can be calculated (cf. 3.4.1.3.).

Table 3.14: Volume-averaged T_1 and T_2 relaxation times for the PIB elastomers CB-30 and CB-330 swollen in CCl_4 .

	CB-30	CB-330
T_1 (s)	0.20	0.20
$T_{2,s}$ (ms)	10.09 (59.1%)	9.97 (58.0%)
$T_{2,l}$ (ms)	30.02 (40.9%)	33.06 (42.0%)
$T_{2,mfw}$ (ms)	18.24	19.67
av. no. voids per cm^2	135	38
$M_{n,eff}^b$ (g/mole)	3150	2510

The results in Table 3.14 show almost no differences in the spin-lattice (T_1) and spin-spin (T_2) relaxation times for the two PIB elastomers. So the molecular chain mobility of both elastomers is almost equivalent as expected from the comparable bulk cross-link density and is not influenced by the different number of voids per cm^2 . Although the bulk number-average molecular weight between the effective cross-links is much lower compared to the unfilled PIB elastomers (Table 3.2), the T_2 relaxation times are still rather large. An explanation of this can be found in the Flory-Rehner equation by which $M_{n,eff}^b$ is determined and which does not take the filler into account (e.g. in ρ_r , χ , ...).

3.7.4. Determination of the diffusion parameters n and D for the diffusion of cyclohexane in filled PIB elastomers with different number of voids

The study of the diffusion of solvent molecules in polymers can provide important information on the diffusion regime, inhomogeneity of the polymer matrix, ... MRI has already been established in literature (and in section 3.4.2.2.) to be a superior technique to monitor these diffusion processes.⁶¹ In this section, the influence of filler and voids on the diffusion behavior of cyclohexane in carbon-black filled PIB elastomers is investigated. For this purpose, cylindrical samples with a diameter of 15 mm and a thickness of about 7 mm were cut out of a rubber sheet of the PIB elastomers CB-30 and CB-330. The samples were placed in the MRI tube and immersed in cyclohexane while a Teflon stopper was placed

on top of the cylinder to avoid longitudinal diffusion. The diffusion distance was determined by means of the image analysis program 'NIH-image' and was used to determine the diffusion coefficient D (experimental method is described in section 3.4.2.2.b)). A plot of the logarithm of the diffusion distance as a function of the logarithm of time results in the diffusion parameter n (equation 3.15). The results are presented in Table 3.15, together with some other properties of the two compounds.

Table 3.15: Diffusion characteristics for the diffusion of cyclohexane in the PIB elastomers CB-30 and CB-330.

	CB-30	CB-330
$M_{n,eff}^b$ (g/mole)	3150	2510
av. no. voids per cm^2	135	38
no. stress-heat cycles before failure	30	330
n	0.76	0.73
D (cm^2/s) ^a	7.73×10^{-7}	4.86×10^{-7}

^a The diffusion coefficient D is determined by means of equation 3.12.

As can be seen in Table 3.15, the parameter n is almost comparable for both elastomers, but is larger than the values found for the unfilled PIB elastomers (Table 3.7). The observed n values of around 0.74 indicate the transport to be of the anomalous type, but not deviating too far from Fickian mode for which the value of n equals 0.5. The presence of carbon-black seems to have a crucial effect on the diffusion characteristics and causes a larger value of n .⁷⁹

Although the diffusion tends to be of the anomalous type, equation 3.12 is still used to calculate the diffusion coefficient for the diffusion of cyclohexane in the carbon-black filled PIB elastomers. The results in Table 3.15 indicate a faster diffusion for the elastomer CB-30 as compared to CB-330. This is also shown in Figure 3.37, displaying the diffusion distance as a function of time for both PIB elastomers. Since the determined effective bulk cross-link density of both elastomers is comparable, this difference in sorption behavior must be due to the difference in the number of voids. As already indicated in literature,⁸⁰ a large

number of voids seems to enhance the diffusion rate of the penetrating solvent. When the diffusion front reaches the void, the penetrant molecules quickly contour the entire surface of the void and the diffusion front propagates from the void.

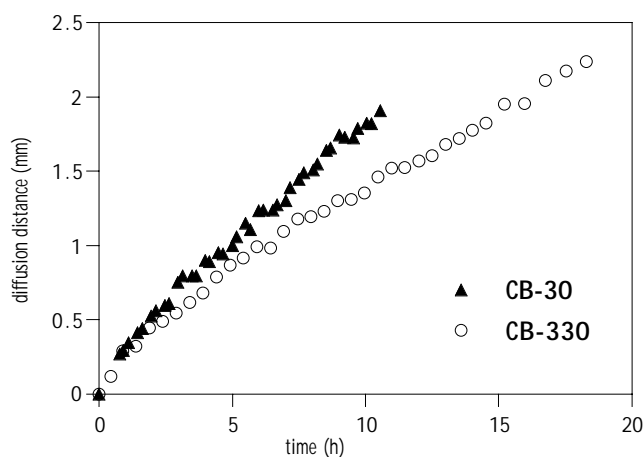


Figure 3.37: Diffusion distance as a function of time for the carbon-black filled PIB elastomers CB-30 and CB-330.

These results clearly demonstrate that the diffusion of cyclohexane in these commercial PIB elastomers is influenced by the presence of the carbon-black loading and the amount of voids. Carbon-black generates polymer-filler interactions, resulting in an anomalous type of diffusion with an increase in the value of n to 0.74. Furthermore, the presence of voids will increase the diffusion rate of the ingressing solvent.

3.7.5. Stress-strain experiments on commercial carbon-black filled PIB elastomers with different number of voids: an MRI study

3.7.5.1. Introduction

Numerous reports have already been published on the mechanical response and strength of elastomers,⁸¹ which postulate that their mechanical behavior is influenced by different parameters such as molecular weight, temperature, the environment (e.g. presence of oxygen), filler and other heterogeneities. Only few papers mention the influence of voids on the failure behavior of rubbery polymers.⁷⁶ Voids, which are often developed during synthesis and processing, can be regarded as inhomogeneities, which can initiate failure in materials. It is proposed that microvoids can grow to some critical size, accompanied by the formation of cracks under further loading.⁸² Thus the presence of voids can cause severe problems concerning the reliability of the mechanical performance of elastomers such as toughness, modulus and yield strength.

The relationship between the presence of microvoids and the mechanical performance of isobutylene-based elastomers was already presumed in section 3.7.2.. In this section, we will look further into detail on the stress resistance of PIB elastomers with different number of voids.

3.7.5.2. Introduction of stress-heat cycles

A dedicated home-built stretching device (Figure 3.38a) was used to perform the fatigue stress-heat cycles. Rectangular pieces were cut from the elastomers (12 × 23 mm) and four holes were made at the corners (Figure 3.38b) in order to fix the elastomer in the top and bottom clamps of the stretching device. While the glass tube fixed the bottom piece, the top piece could be pulled up by a screw bar resulting in elongation of the elastomer.⁸³ Although the stretching device was made from copper, the image distortions were still too large to obtain a good quality rubber image of the specimen under load in the stretching device. Consequently, all MRI images had to be recorded without the device and the sample was no longer under stress in the magnet.

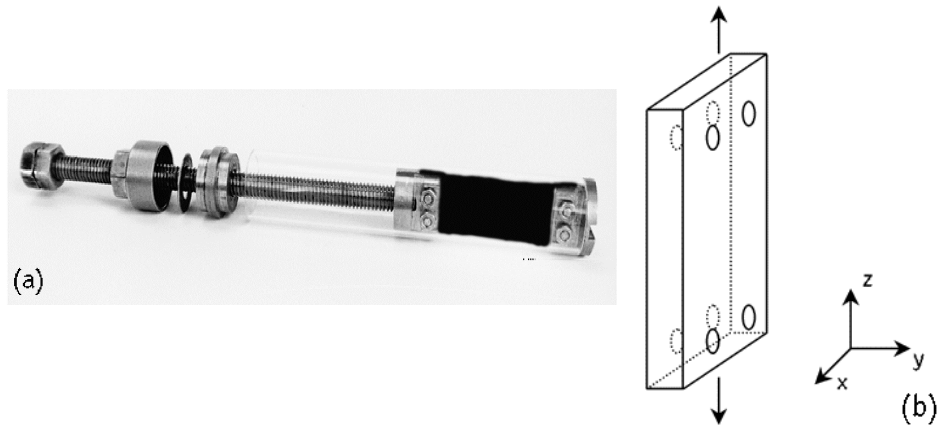


Figure 3.38: (a) The dedicated home-built stretching device and (b) experimental set-up for the elastomer.

A comparison was performed between the two PIB elastomers CB-30 and CB-330. Both elastomers display an extreme difference in the number of voids and in mechanical performance, but have a comparable cross-link density and filler load. The rectangular native samples, swollen in cyclohexane, were placed in the MRI tube parallel to the static magnetic field B_0 by using a special Teflon holder and MRI images were recorded in the transverse (xy) and longitudinal (xz) direction. Afterwards, the samples were dried carefully in order to remove all the swelling solvent and then subjected to a number of mechanical stress-heat cycles.

In order to approach the fatigue experiments described in section 3.7.1.2. as closely as possible, the following experimental procedure was used. The dry elastomers were fixed in the stretching device and a strain of about 80-100% was applied (the strain $\lambda = (L-L_0)/L_0$ is the relative change of length⁸⁴). The stretched samples were then placed in an oven at 190 °C for 11 minutes. After unloading (out of the oven), the samples were stretched again and replaced in the oven at 190 °C. These stress-heat experiments induce a gradual weakening of the elastomers and eventually fracture by repeated deformations much lower than the breaking strain.⁸⁵ After repeating these stress-heat cycles for a number of times, the specimens were reswollen and imaged to look for possible crack growth.

3.7.5.3. MRI images of a solvent-swollen 'void-rich' PIB elastomer as a function of stress-heat cycles

The PIB elastomer CB-30, used in these stretching experiments, displays a rather weak mechanical performance (about 30 mechanical stress-heat cycles before failure) and contains a large number of voids (an average of 135 voids per cm^2). The transverse MRI images (xy -plane) of the cyclohexane-swollen native elastomer are presented in Figure 3.39a and 3.39b and clearly show the presence of several spherical voids.

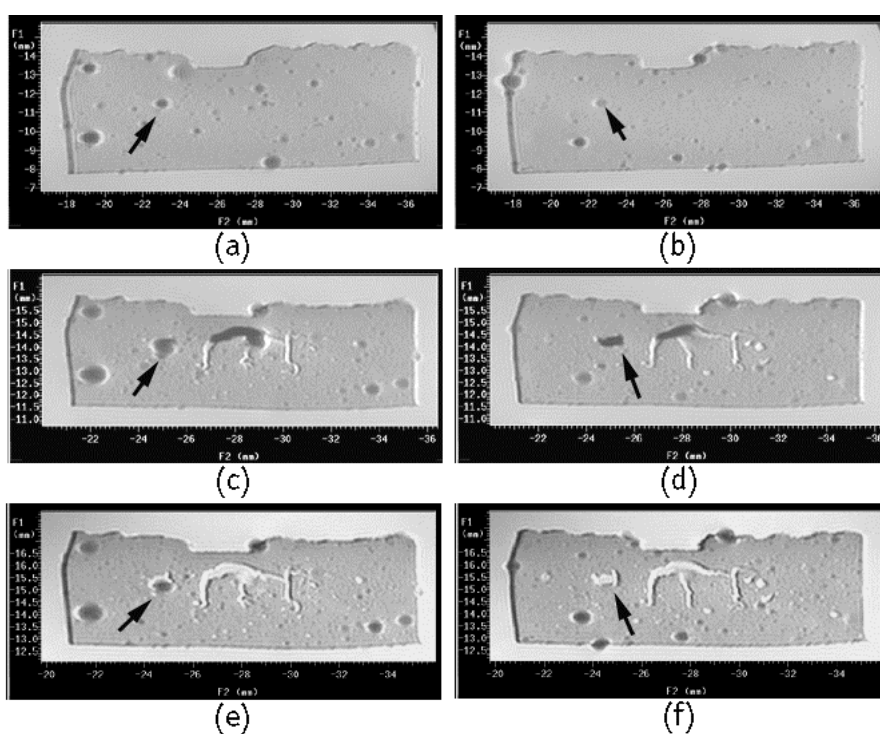


Figure 3.39: Transverse MRI images of the cyclohexane-swollen CB-30 elastomer: (a) and (b) represent two consecutive slices of the native unstretched rubber, (c) and (d) are the same slices after the rubber is subjected to 61 stress-heat cycles and (e) and (f) are the slices after the tested elastomer was placed under vacuum for 1.5 hour.

After drying the elastomer, it was subjected to 35 stress-heat cycles as previously described. Although the elastomer already displayed some cracks, the number of stress-heat cycles was still increased to further damage the sample.

Finally, the elastomer underwent 61 mechanical stress-heat cycles before it was torn out of the screws on the top clamp of the stretching device.

Figure 3.39c and 3.39d show the MRI images after 61 stress-heat cycles and after the sample was reswollen in cyclohexane. Localization of the identical slices as shown in Figure 3.39a and 3.39b was difficult because of the elongation of the elastomer during the stress-strain experiments. At the center part of the elastomer, some cracks are clearly visible which are not completely filled with solvent. The arrows indicate voids, which have become larger and irregularly shaped, but not filled with solvent. The cracks are probably also filled with air and surface tension prevents the solvent from entering the crack. To try to fill up these cracks with solvent, the swollen rubber was placed under vacuum (about 80 mbar) for about 1.5 hour. The MRI images after degassing (Figure 3.39e and 3.39f) demonstrate that the cracks are now filled with solvent. Also the grown voids (arrows) became filled with solvent.

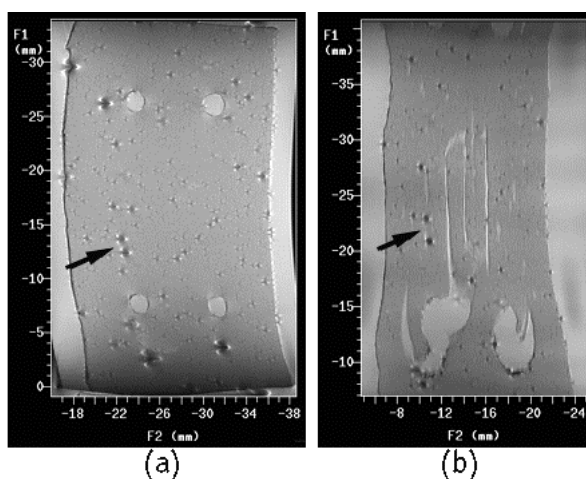


Figure 3.40: Longitudinal MRI images of the cyclohexane-swollen CB-30 elastomer: (a) represents a slice of the native unstretched rubber and (b) shows the same slice after the rubber is subjected to 61 stress-heat cycles and degassed for 1.5 under vacuum.

Figure 3.40 displays some longitudinal (xz-plane) MRI slices of the swollen CB-30 elastomer before (Figure 3.40a) and after (Figure 3.40b) the 61 stress-heat cycles. The elongation of the rubber due to the stress-strain cycles is clearly demonstrated by the indicated voids, which appear further apart from each other. Also the cracks are clearly visible in Figure 3.40b. They are parallel to the

stretching direction and became filled up with solvent. Remark that damage also appears at the holes for the screws at the bottom clamp.

3.7.5.4. MRI images of a solvent-swollen 'void-poor' PIB elastomer as a function of stress-heat cycles

Similar experiments were performed on the PIB elastomer CB-330 that displays a good mechanical performance (about 330 mechanical stress-heat cycles before failure) and contains only few voids (an average of 38 voids per cm^2). Some longitudinal MRI images of the cyclohexane-swollen CB-330 elastomer before and after loading cycles are shown in Figure 3.41.

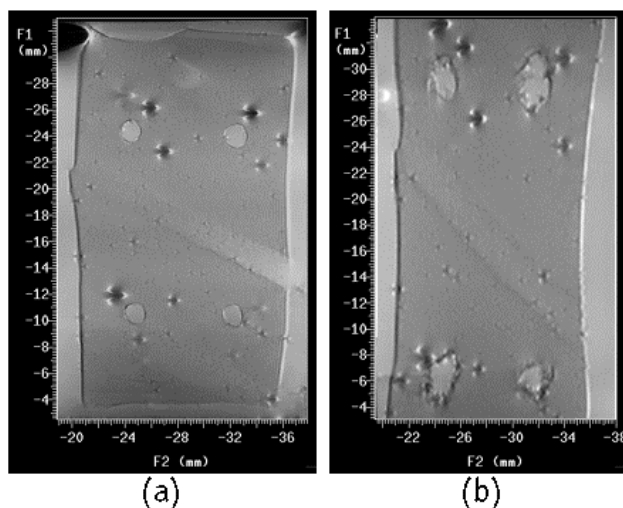


Figure 3.41: Longitudinal MRI images of the cyclohexane-swollen CB-330 elastomer: (a) represents a slice of the native unstretched rubber and (b) shows the same slice after the rubber is subjected to 61 stress-heat cycles.

The MRI image of the native unstretched CB-330 elastomer (Figure 3.41a) clearly displays the presence of a few voids. After subjecting this elastomer to 61 stress-heat cycles (similar as for the CB-30 elastomer), almost no visible deterioration or cracks could be observed (Figure 3.41b). Only a certain elongation of the elastomer is noticed. Also after degassing this rubber for 1 hour under vacuum (80 mbar), no differences are observed.

Chapter 3

The above results clearly confirm the previously stated relationship between the number of voids and the mechanical performance of elastomers.

3.7.5.5. Conclusion

The statistical void density analysis already indicated a relationship between the mechanical performance of the carbon-black filled PIB elastomers and the presence of voids. The presence of a large number of voids can lead to early failure of the compound. Although no void-to-void cracking is observed in the MRI images, failure appears earlier for rubbers having a large number of voids compared to rubbers with only a small amount of voids. So instead of void-to-void crack growth, it is possible that the lower density of the rubber matrix leads to stress concentration in the remaining rubber network and induces premature failure.

3.8. General conclusions and summary

The presented results clearly demonstrate that the NMR imaging technique is a very useful method to study defects and network inhomogeneities in PIB-based elastomers. Because the ^1H T_2 relaxation time is too short to directly image the PIB elastomers at room temperature, image acquisition is facilitated by increasing the temperature or by solvent swelling. Local inhomogeneities in cure state are visualized in the rubber images of the elastomers swollen in benzene or CCl_4 : weakly cured regions display a higher molecular chain mobility and appear clear in the rubber images. Also different patterns of network heterogeneity are observed depending on curative mixing. On the basis of a linear relation between the Flory-Rehner bulk number-average molecular weight between effective cross-links ($M_{n,\text{eff}}^b$) and the volume-averaged T_2 decay times, MRI allows the determination of the local cross-link density in unfilled 1,6-hexamethylene-diamine-cured PIB elastomers by means of the spatially dependent T_2 decay times. MRI solvent diffusion experiments reveal that the ingress kinetics of cyclohexane in unfilled PIB elastomers is Fickian and depends on the cure state.

Imaging of the swelling solvent is proven to be superior towards the detection of microvoids in the PIB elastomers. The voids are 'air-bubbles', already present in the rubber matrix before (or induced during) the mixing. It is demonstrated that *i*) voids are inherent to the rubber matrix and are not induced by the swelling solvent, *ii*) they are spherically shaped and *iii*) a solid state NMR relaxation time study excludes that they might be assigned to regions of higher cross-link density. A statistical void density analysis of six carbon-black filled PIB elastomers with a comparable cross-link density but with a different number of voids, indicates a strong linear correlation between the mechanical performance and the average number of voids per unit area. The experimental results indicate that high void density in cured elastomers leads to a premature failure of the compound.

So it is generally demonstrated that NMR imaging provides an attractive approach to obtain network and microvoid information on bulk volume scales in rubber materials.

3.9. Experimental part

3.9.1. Materials

The PIB-PMS/BrPMS elastomers (Scheme 3.1) contain 90 – 98 mole % PIB and 2 – 10 mole % PMS of which 0.5 – 2 % is brominated. As such, the molecular chain dynamics and relaxation properties are quite similar to neat PIB. Cross-linking occurs through the BrPMS functionality in the presence of ZnO or by the bi-functional organic curative 1,6-hexamethylenediamine. The unfilled 1,6-hexamethylenediamine cured specimens 1 to 4 used in section 3.4., were taken from four different batches. The degree of cross-linking increases from specimen 1 to specimen 4. The other experiments were performed on commercial carbon-black filled (about 55 phr) PIB-based elastomers. The blend of PIB and BR (section 3.5.) is also filled with carbon-black.

3.9.2. NMR imaging

The MRI images were acquired at room temperature (unless otherwise noted) on Varian Inova 400 and 300 MHz vertical bore spectrometers, equipped with an imaging probe with an inner diameter of 25 mm. Images were obtained in a field of view of 25 × 25 mm with an in-plane pixel resolution of 100 × 100 μm. Images of samples swollen in CCl₄ and C₆H₁₂ were obtained with a classical spin-warp pulse sequence in which slice selective 90° and 180° sinc pulses were used. Images of samples swollen in C₆H₆ were obtained by using a chemical shift selective 90° Gaussian pulse, followed by a slice selective 180° sinc pulse.

Images of the polymers spins in a swollen sample (CCl₄ or C₆H₆) were obtained with a repetition time TR = 1 s and an echo time TE = 11 - 13 ms or TE = 25 ms ('T₂-weighted' images). For the blend PIB/BR, swollen in CCl₄, the non-chemical shift selective images were recorded with TR = 2.5 s and the chemical shift selective images with TR = 1.5 s or 2.5 s for respectively the aliphatic or olefinic image.

For images of the swelling solvent only, TR = 3 s and TE = 11 – 13 ms were used (unless otherwise noted). Since solvents in general have a longer T_1 than the polymer, a longer repetition time is required.

Usually, images were acquired with a slice thickness of 1 mm except for the rubber images in section 3.4. (2 mm), for the 3-D analysis in section 3.6.2.3. (150 μm) and for the statistical void density analysis in section 3.7.2. (200 μm).

For the determination of the volume-averaged T_1 and T_2 relaxation times of the unfilled 1,6-hexamethylenediamine cured samples (section 3.4.), the 1-D projection signal intensity was analyzed vs. a variable TR and TE, respectively. TR was varied from 0.1 to 3 s (TE was fixed to 7.2 ms), while TE was varied from 7.2 to 250 ms (TR = 1 s). To determine the local T_2 relaxation decay times, rubber images of the CCl_4 -swollen samples were recorded as a function of TE with TE values ranging between 7.2 and 200 ms and with a fixed TR of 1 s. Regions of interest were only selected in the inner part of the specimens where the B_1 field is highly homogeneous.

For the determination of the volume-averaged T_1 and T_2 relaxation times of the carbon-black filled PIB elastomers (section 3.7.), TR was varied between 0.1 and 2 s (TE = 7.2 ms) and TE between 7.2 and 200 ms (TR = 1 s), respectively.

To study the diffusion kinetics of cyclohexane ingress in the filled and unfilled specimens, MRI images with a slice thickness of 0.75 mm, TE = 16 ms and TR = 0.5 s were recorded as a function of time

In the stretching experiments, MRI images were recorded from the cyclohexane-swollen carbon-black filled PIB elastomers with a slice thickness of 1 mm, TE = 16 ms and TE = 3 s. Images were recorded in the transverse plane (xy) and in the longitudinal direction (xz).

Direct polymer images of the dry unswollen elastomer were obtained by using a 16 mm coil with a spin-warp pulse sequence, a slice thickness of 1.5 mm, TE = 2.15 ms (or 1.5 ms), TR = 1 s and at a temperature of 60 °C (or 70 °C).

3.9.3. Solid state NMR relaxometry

Solid state CP/MAS NMR experiments were performed at room temperature on an Inova 400 spectrometer, operating at a static magnetic field of 9.4 T. Magic angle spinning was performed at 4 kHz by using Si_3N_4 rotors. Other spectral parameters were a 90° pulse length of 5.3 μs and a spectral width of 50 kHz.

^1H wideline NMR measurements were performed on a Varian Unity 400 spectrometer with a static transverse 5 mm coil. A sweep width of 2 MHz was used.

The non-linear least squares analyses were performed on a Macintosh computer by using the program KaleidaGraph 3.0.

3.9.4. Scanning electron microscopy

Specimens for scanning electron microscopy were prepared from cyclohexane-swollen PIB samples used for the MRI experiments. After the solvent was removed by drying, the surface was coated with carbon and examined in a Philips XL30-FEG/EDX scanning electron microscope.

3.10. References

1. Mullens S. *'Mogelijkheden en beperkingen van AP-TPR'*, PhD dissertation, LUC Diepenbeek, 2000.
2. Hofmann, W. *'Rubber Technology Handbook'*, Hanser Publ., New York, 1988.
3. Hosler, D.; Burkett, S.; Tarkanian, M. *Science* **1999**, *284*, 1988.
4. Cowie, J.M.G. *'Polymers: Chemistry and Physics of Modern Materials'*, Blackie Academic & Professional, Glasgow, 1991.
5. Nagdi, K. *'Rubber as an Engineering Material: Guideline for Users'*, Hanser Publishers, Munich, 1993.
6. Schouten, A.E.; van der Vegt, A.K. *'Plastics'*, Delta Press B.V., Overberg, 1987.
7. a) Merrill, N.A.; Powers, K.W.; Wang, H.C. *Polym. Prepr.* **1992**, *33*, 962. b) Müller-Plathe, F.; Rogers, S.C.; Van Gunsteren, W.F. *J. Chem. Phys.* **1993**, *98*, 9895. c) Cao, X.; Sipos, L.; Faust, R. *Polym. Bull.* **2000**, *45*, 121. d) Ashbaugh, J.R.; Ruff, C.R.; Shaffer, T.D. *J. Polym. Sci. A: Polym. Chem.* **2000**, *38*, 1680.
8. McElrath, K.O.; Tisler, A.L.; Tse, M.F. *'New developments in Exxpro elastomer based sidewalls'*, Paper presented at ITEC, Akron, Ohio, 1998.
9. a) Bielski, R.; Fréchet, J.M.J.; Fusco, J.V.; Powers, K.W.; Wang, H.C. *J. Polym. Sci. A: Polym. Chem.* **1993**, *31*, 755. b) Jayaraman, M.; Fréchet, J.M.J.; Dias, A.J.; Wang, H.C. *J. Appl. Polym. Sci.* **2001**, *80*, 680.
10. Fülber, C.; Blümich, B.; Unseld, K.; Herrmann, V. *Kautsch. Gummi. Kunstst.* **1995**, *48*, 254.
11. a) Sheng, E.; Bradley, R.H.; Sutherland, I.; Freakley, P.K.; Ismail, H. *Surf. Interface Anal.* **1994**, *22*, 491. b) Fond, C.; Kiefer, J.; Mendels, D.; Ferrer, J.B.; Kausch, H.H.; Hilborn, J.G. *J. Mater. Sci.* **1998**, *33*, 3975. c) Wang, G.; Li, M.; Chen, X. *J. Appl. Polym. Sci.* **1999**, *72*, 577.
12. a) Eisenbach, C.D.; Ribbe, R. *Kautsch. Gummi. Kunstst.* **1994**, *47*, 477. b) DiFoggio, R.; McElrath, K.O.; Tisler, A.L.; Ball, J.W. *'Microscopic Image Analysis of Elastomers Can Infer Physical Properties'*, Paper presented at a meeting of the Rubber Division ACS, Indianapolis, Indiana, 1998. c) Tse, M.F.; Wang, H.C.; Shaffer, T.D.; McElrath, K.O.; Modi, M.A.; Krishnamoorti, R. *Polym. Eng. Sci.* **2000**, *40*, 2182.
13. a) Roychoudhury, A.; De, P.P. *J. Appl. Polym. Sci.* **1995**, *55*, 9. b) Rana, S.K.; Chandra, R. *J. Appl. Polym. Sci.* **2000**, *78*, 25. c) Prado, P.J.; Gasper, L.; Fink, G.; Blümich, B.; Herrmann, V.; Unseld, K.; Fuchs, H.; Möhler, H.; Rühl, M. *Macromol. Mat. Eng.* **2000**, *274*, 13.

14. Dias, A.J.; Galuska, A.A. *Rubber Chem. Technol.* **1996**, *69*, 615.
15. a) Maas, S.; Gronski, W. *Kautsch. Gummi. Kunstst.* **1994**, *47*, 409. b) Maas, S.; Lay, R.; Gronski, W. *Kautsch. Gummi. Kunstst.* **1996**, *49*, 166. c) Mareanukroh, M.; Eby, R.K.; Scavuzzo, R.J.; Hamed, G.R. *Rubber Chem. Technol.* **2000**, *73*, 912.
16. a) Persson, S.; Ostman, E. *Appl. Optics* **1985**, *24*, 4095. b) Persson, S. *Polymer*, **1988**, *29*, 802. c) Listerud, J.M.; Sinton, S.W.; Drobny, G.P. *Anal. Chem.* **1989**, *61*, 23A. d) Dunsmuir, J.H.; Dias, A.J.; Peiffer, D.G.; Kolb, R.; Jones, G. 'Microtomography of Elastomers for Tire Manufacture', in Developments in X-Ray Tomography II, Ulrich Bonse, Proceedings of SPIE, vol. 3772, 87, 1999.
17. a) Komoroski, R.A. *Rubber Chem. Technol.* **1983**, *56*, 959. b) Zaper, A.M.; Koenig, J.L. *Rubber Chem. Technol.* **1987**, *60*, 252. c) Andreis, M.; Koenig, J.L. *Adv. Polym. Sci.* **1989**, *89*, 69. d) Blümich, B.; Hagemeyer, A.; Schaefer, D.; Schmidt-Rohr, K.; Spiess, H.W. *Adv. Mater.* **1990**, *2*, 72. e) Gronski, W.; Hoffmann, U.; Simon, G.; Wutzler, A.; Straube, E. *Rubber Chem. Technol.* **1992**, *65*, 63. f) Apple, T.M. *Appl. Spectrosc.* **1995**, *49*, 12A. g) Van der Velden, G.; Beulen, J. *Polym. Prepr.* **1997**, *38*, 865. h) Mori, M.; Koenig, J.L. *J. Appl. Polym. Sci.* **1998**, *70*, 1391. i) Pelliccioli, S.K.; Mowdood, S.K.; Negrone, F. *Rubber Chem. Technol.* **2002**, *75*, 65.
18. Buzaré, J.Y.; Silly, G.; Emery, J.; Boccaccio, G.; Rouault, E. *Eur. Polym. J.* **2001**, *37*, 85.
19. Somers, A.E.; Bastow, T.J.; Burgar, M.I.; Forsyth, M.; Hill, A.J. *Polym. Degrad. Stabil.* **2000**, *70*, 31.
20. a) White, J.L.; Mirau, P. *Macromolecules* **1993**, *26*, 3049. b) Sotta, P.; Fülber, C.; Demco, D.E.; Blümich, B.; Spiess, W.H. *Macromolecules* **1996**, *29*, 6222. c) White, J.L.; Dias, A.J.; Ashbaugh, J.R. *Macromolecules* **1998**, *31*, 1880. d) White, J.L.; Brant, P. *Macromolecules* **1998**, *31*, 5424. e) Menge, H.; Hotopf, S.; Heuert, U.; Schneider, H. *Polymer* **2000**, *41*, 3019. f) Ricardo, N.M.P.S.; Lahtinen, M.; Price, C.; Heatley, F. *Polym. Int.* **2002**, *51*, 627.
21. a) White, J.L.; Dias, A.J. *Polym. Prepr.* **1997**, *38*, 890. b) Menge, H.; Kühn, H.; Blümich, B.; Blümmler, P.; Schneider, H. *Macromol. Mater. Eng.* **2000**, *282*, 1.
22. a) Simon, G.; Schneider, H. *Makromol. Chem., Macromol. Symp.* **1991**, *52*, 233. b) Ries, M.E.; Brereton, M.G.; Klein, P.G.; Ward, I.M.; Ekanayake, P.; Menge, H.; Schneider, H. *Macromolecules* **1999**, *32*, 4961. c) Menge, H.; Hotopf, S.; Schneider, H. *Polymer* **2000**, *41*, 4189. d) Litvinov, V.M.; van Duin, M. *Kautsch. Gummi. Kunstst.* **2002**, *55*, 460.

23. a) Litvinov, V.M.; Steeman, P.A.M. *Macromolecules* **1999**, *32*, 8476. b) Ekanayake, P.; Menge, H.; Schneider, H.; Ries, M.E.; Brereton, M.G.; Klein, P.G. *Macromolecules* **2000**, *33*, 1807. c) Mansencal, R.; Haidar, B.; Vidal, A.; Delmotte, L.; Chezeau, J. *Polym. Int.* **2001**, *50*, 387.
24. Lauterbur, P. *Nature* **1973**, *242*, 190.
25. a) Komoroski, R.A. *Anal. Chem.* **1993**, *65*, 1068A. b) Blümich, B.; Blümmler, P. *Macromol. Symp.* **1994**, *87*, 187. c) Narasimhan, B.; Snaar, J.E.M.; Bowtell, R.W.; Morgan, S.; Melia, C.D.; Peppas, N.A. *Macromolecules* **1999**, *32*, 704.
26. a) Koenig, J.L. *Macromol. Symp.* **1994**, *86*, 283. b) Ritchey, W.M.; Maylish-Kogovsek, L.; Wallner, A.S. *Appl. Spectrosc. Rev.* **1994**, *29*, 233. c) Kuhn, W.; Barth, P.; Denner, P.; Müller, R. *Solid State NMR* **1996**, *6*, 295. d) Blümmler, P.; Blümich, B. *Rubber Chem. Technol.* **1997**, *70*, 468.
27. a) Smith, S.R.; Koenig, J.L. *Macromolecules* **1991**, *24*, 3496. b) Zhao, X.; She, Y.M.; Du, Y.R.; Ye, C.H. *Appl. Magn. Reson.* **1993**, *5*, 39. c) Halse, M.R.; Rahman, H.J.; Strange, J.H. *Physica B* **1994**, *203*, 169. d) Mori, M.; Koenig, J.L. *J. Appl. Polym. Sci.* **1998**, *70*, 1385.
28. a) Webb, A.G.; Jezzard, P.; Hall, L.D.; Ng, S. *Polym. Comm.* **1989**, *30*, 363. b) Webb, A.G.; Hall, L.D. *Polym. Comm.* **1990**, *31*, 422. c) Halse, M.R.; Rahman, H.J.; Strange, J.H. *Physica B* **1994**, *203*, 169. d) Adriaensens, P.; Pollaris, A.; Vanderzande D.; Gelan, J.; Kelchtermans, M. *Macromolecules* **2003**, *36*, 706.
29. a) Hore, P.J. *J. Magn. Reson.* **1983**, *55*, 283. b) Webb, A.G.; Hall, L.D. *Polym. Comm.* **1990**, *31*, 425. c) De Crespigny, A.J.S.; Carpenter, T.A.; Hall, A.D.; Webb, A.G. *Polym. Comm.* **1991**, *32*, 36. d) Webb, A.G.; Hall, L.D. *Polymer* **1991**, *32*, 2926.
30. a) Clough, R.S.; Koenig, J.L. *J. Polym. Sci. Part C: Polym. Lett.* **1989**, *27*, 451. b) Smith, S.R.; Koenig, J.L. *Macromolecules* **1991**, *24*, 3496. c) Rana, M.A.; Koenig, J.L. *Macromolecules* **1994**, *27*, 3727. d) Kuhn, W.; Barth, P.; Denner, P.; Müller, R. *Solid State NMR* **1996**, *6*, 295. e) Barth, P.; Hafner, S.; Denner, P. *Macromolecules*, **1996**, *29*, 1655. f) Blümmler, P.; Blümich, B. *Rubber Chem. Technol.* **1997**, *70*, 468. g) Klei, B.; Koenig, J.L. *Acta Polymer.* **1997**, *48*, 199. h) Mori, M.; Koenig, J.L. *J. Appl. Polym. Sci.* **1998**, *70*, 1385. i) Adriaensens, P.; Pollaris, A.; Vanderzande, D.; Gelan, J.; White, J.L.; Dias, A.J.; Kelchtermans, M. *Macromolecules* **1999**, *32*, 4692. j) Blümich, B.; Blümmler, P.; Gasper, L.; Guthausen, A.; Göbbels, V.; Laukemper-Ostendorf, S.; Unseld, K.; Zimmer, G. *Macromol. Symp.* **1999**, *141*, 83. k) Prado, P.J.; Gasper, L.; Fink, G.; Blümich, B. *Appl. Magn. Reson.* **2000**, *18*, 177.

31. a) Fukumori, K.; Kurauchi, T.; Kamigaito, O. *Polymer* **1990**, *31*, 713. b) Krejsa, M.R.; Koenig, J.L. *Rubber Chem. Technol.* **1991**, *64*, 635. c) Koenig, J.L. *Macromol. Symp.* **1994**, *86*, 283. d) Knörger, M.; Heuert, U.; Schneider, H.; Kuckling, D.; Richter, S.; Arndt, K.F. *Macromol. Symp.* **1999**, *145*, 83.
32. a) Blümmler, P.; Blümich, B. *Macromolecules* **1991**, *24*, 2183. b) Blümich, B.; Blümmler, P.; Günther, E.; Schauss, G.; Spiess, H.W. *Makromol. Chem., Macromol. Symp.* **1991**, *44*, 37. c) Chudek, J.A.; Hunter, G. *J. Mater. Sci. Lett.* **1992**, *11*, 222. d) Blümmler, P.; Blümich, B.; Dumler, H. *Kautsch. Gummi. Kunstst.* **1992**, *45*, 699. e) Blümich, B.; Kuhn, W. 'Magnetic Resonance Microscopy', VCH, Weinheim, 1992. f) Blümmler, P.; Blümich, B. *Magn. Reson. Imag.* **1992**, *10*, 779. g) Kuhn, W.; Barth, P.; Hafner, S.; Simon, G.; Schneider, H. *Macromolecules* **1994**, *27*, 5773. h) Fülber, C.; Blümich, B.; Unseld, K.; Herrmann, V. *Kautsch. Gummi. Kunstst.* **1995**, *48*, 254. i) Hafner, S.; Barth, P. *Magn. Reson. Imag.* **1995**, *13*, 739. j) Knörger, M.; Heuert, U.; Schneider, H.; Barth, P.; Kuhn, W. *Polym. Bull.* **1997**, *38*, 101. k) Knörger, M.; Heuert, U.; Menge, H.; Schneider, H. *Angew. Makromol. Chem.* **1998**, *261/262*, 123. l) Knörger, M.; Heuert, U.; Schneider, H.; Heinrich, G. *J. Macromol. Sci. Phys.* **1999**, *B38*, 1009.
33. a) Chang, C.; Komoroski, R.A. *Macromolecules* **1989**, *22*, 600. b) Krejsa, M.R.; Koenig, J.L. *Rubber Chem. Technol.* **1991**, *64*, 635. c) Jezzard, P.; Wiggings, C.J.; Carpenter, T.A.; Hall, L.D.; Jackson, P.; Clayden, N.J.; Walton, N.J. *Adv. Mater.* **1992**, *4*, 82. d) Sarkar, S.N.; Komoroski, R.A. *Macromolecules* **1992**, *25*, 1420. e) Matsui, S.; Ogasawara, Y.; Inouye, T. *J. Magn. Reson. A* **1993**, *105*, 215. f) Koenig, J.L. *Macromol. Symp.* **1994**, *86*, 283. g) Klei, B.; Koenig, J.L. *Acta Polymer.* **1997**, *48*, 199. h) Adriaensens, P.; Pollaris, A.; Vanderzande, D.; Gelan, J.; White, J.L.; Dias, A.J.; Kelchtermans, M. *Macromolecules* **1999**, *32*, 4692. i) Adriaensens, P.; Pollaris, A.; Vanderzande, D.; Gelan, J.; White, J.L.; Kelchtermans, M. *Macromolecules* **2000**, *33*, 7116.
34. Blümmler, P.; Blümich, B. *Acta Polymer.* **1993**, *44*, 125.
35. a) Günther, E.; Blümich, B.; Spiess, H.W. *Molec. Phys.* **1990**, *71*, 477. b) Klinkenberg, M.; Blümmler, P.; Blümich, B. *J. Magn. Reson. A* **1996**, *119*, 197. c) Klinkenberg, M.; Blümmler, P.; Blümich, B. *Macromolecules* **1997**, *30*, 1038.
36. Schneider, M.; Demco, D.E.; Blümich, B. *Macromolecules* **2001**, *34*, 4019.
37. a) Cory, D.C.; Van Os, J.W.M.; Veeman, W.S. *J. Magn. Reson.* **1988**, *76*, 543. b) Cory, D.G.; de Boer, J.C.; Veeman, W.S. *Macromolecules* **1989**, *22*, 1218. c) Blümich, B.; Blümmler, P.; Günther, E.; Schauss, G.; Spiess, H.W. *Makromol. Chem., Macromol.*

- Symp.* **1991**, *44*, 37. d) Schauss, G.; Blümich, B.; Spiess, H.W. *J. Magn. Reson.* **1991**, *95*, 437. e) Matsui, S.; Ogasawara, Y.; Inouye, T. *J. Magn. Reson. A* **1993**, *105*, 215.
38. a) Chingas, G.C.; Miller, J.B.; Garroway, A.N. *J. Magn. Reson.* **1986**, *66*, 530. b) Miller, J.B.; Garroway, A.N. *J. Magn. Reson.* **1988**, *77*, 187. c) Cottrell, S.P.; Halse, M.R.; Strange, J.H. *Meas. Sci. Technol.* **1990**, *1*, 624. d) Prado, P.J.; Gasper, L.; Fink, G.; Blümich, B. *Appl. Magn. Reson.* **2000**, *18*, 177.
39. Donnet, J.B.; Voet, A. *'Carbon-Black'*, Marcel Dekker, New York, 1976.
40. a) Chang, C.; Komoroski, R.A. *Macromolecules* **1989**, *22*, 600. b) Blümmler, P.; Blümich, B. *Macromolecules* **1991**, *24*, 2183. c) Kuhn, W.; Barth, P.; Hafner, S.; Simon, G.; Schneider, H. *Macromolecules* **1994**, *27*, 5773. d) Knörngen, M.; Heuert, U.; Menge, H.; Schneider, H. *Angew. Makromol. Chem.* **1998**, *261/262*, 123.
41. a) Boyd, R.H.; Pant, P.V.K. *Macromolecules* **1991**, *24*, 6325. b) White, J.L.; Dias, A.J.; Ashbaugh, J.R. *Macromolecules* **1998**, *31*, 1880.
42. a) Lüdeke, K.M.; Röschmann, P.; Tischler, R. *Magn. Reson. Imag.* **1985**, *3*, 329. b) Liu, J.; Nieminen, A.O.K.; Koenig, J.L. *J. Magn. Reson.* **1989**, *85*, 95. c) Chang, C.; Komoroski, R.A. *Macromolecules* **1989**, *22*, 600. d) Callaghan, P.T. *J. Magn. Reson.* **1990**, *87*, 304. e) Posse, S.; Aue, W.P. *J. Magn. Reson.* **1990**, *88*, 473. f) Komoroski, R.A.; Sarkar, S.N. *Mat. Res. Soc. Symp. Proc.* **1991**, *217*, 3. g) Gussoni, M.; Greco, F.; Mapelli, M.; Vezzoli, A.; Ranucci, E.; Ferruti, P.; Zetta, L. *Macromolecules* **2002**, *35*, 1714.
43. a) Menge, H.; Hotopf, S.; Pönitzsch, S.; Richter, S.; Arndt, K.; Schneider, H.; Heuert, U. *Polymer* **1999**, *40*, 5303. b) George, S.C.; Knörngen, M.; Thomas, S. *J. Membr. Sci.* **1999**, *163*, 1.
44. Parent, J.S.; White, G.D.F.; Whitney, R.A.; Hopkins, W. *Macromolecules* **2002**, *35*, 3374.
45. a) Simon, G.; Baumann, K.; Gronski, W. *Macromolecules* **1992**, *25*, 3624. b) Oh, S.J.; Koenig, J.L. *Polymer* **1999**, *40*, 4703.
46. a) Smith, S.R.; Koenig, J.L. *Macromolecules* **1991**, *24*, 3496. b) Rana, M.A.; Koenig, J.L. *Macromolecules* **1994**, *27*, 3727. c) Aminabhvi, T.M.; Phayde, H.T.S. *Polymer* **1995**, *36*, 1023. d) Mathew, A.P.; Packirisamy, A.P.M.; Kumaran, M.G.; Thomas, S. *Polymer* **1995**, *36*, 4935. e) Aminabhvi, T.M.; Munnolli, R.S. *Polym. Int.* **1995**, *36*, 353. f) Mathai, A.E.; Thomas, S. *J. Macromol. Sci. Phys.* **1996**, *B35*, 229. g) Unnikrishnan, G.; Thomas, S.; Varghese, S. *Polymer* **1996**, *37*, 2687. h) Amin, M.; Nasr, G.M.; Attia, G.; Gomaa, A.S. *Mater. Lett.* **1996**, *28*, 207. i) Unnikrishnan, G.;

- Thomas, S. *J. Polym. Sci. B: Polym. Phys.* **1997**, *35*, 725. j) Mori, M.; Koenig, J.L. *J. Appl. Polym. Sci.* **1998**, *70*, 1391. k) Desai, S.; Thakore, I.M.; Devi, S. *Polym. Int.* **1998**, *47*, 172. l) Bokobza, L. *Polym. Int.* **2000**, *49*, 743. m) Cho, K.; Jang, W.J.; Lee, D.; Chun, H.; Chang, Y.W. *Polymer* **2000**, *41*, 179.
47. a) Flory, P.J.; Rehner, J. *J. Chem. Phys.* **1943**, *11*, 521. b) Flory, P.J. *J. Chem. Phys.* **1950**, *18*, 108. c) Flory, P.J. *J. Chem. Phys.* **1950**, *18*, 112.
48. Brandrup, J.; Immergut, E.H. *'Polymer Handbook. Third Edition'*, John Wiley & Sons, New York, 1989.
49. a) Fukumori, K.; Kurauchi, T.; Kamigaito, O. *Polymer* **1990**, *31*, 713. b) Smith, S.R.; Koenig, J.L. *Macromolecules* **1991**, *24*, 3496. c) Krejsa, M.R.; Koenig, J.L. *Rubber Chem. Technol.* **1992**, *65*, 956. d) Oh, S.J.; Koenig, J.L. *Polymer* **1999**, *40*, 4703.
50. Waters, J.F.; Likavec, W.R.; Ritchey, W.M. *J. Appl. Polym. Sci.* **1994**, *53*, 59.
51. a) Schneider, M.; Demco, D.E.; Blümich, B. *J. Magn. Reson.* **1999**, *140*, 432. b) Schneider, M.; Demco, D.E.; Blümich, B. *Macromolecules* **2001**, *34*, 4019.
52. a) Stern, S.A.; Shah, V.M.; Hardy, B.J. *J. Polym. Sci., Polym. Phys. Ed.* **1987**, *25*, 1293. b) Naylor, T. *'Comprehensive Polymer Science. Vol. 2: Polymer Properties'*, Pergamon Press, Oxford, 1989.
53. a) Frisch, H.L. *Polym. Eng. Sci.* **1980**, *20*, 2. b) Gall, T.P.; Lasky, R.C.; Kramer, E.J. *Polymer* **1990**, *31*, 1491. c) Pant, P.V.K.; Boyd, R.H. *Macromolecules* **1992**, *25*, 494. d) Vrentas, J.S.; Vrentas, C.M.; Faridi, N. *Macromolecules* **1996**, *29*, 3272.
54. Aminabhavi, T.M.; Munnolli, R.S. *Polym. Int.* **1993**, *32*, 61.
55. a) Perry, K.L.; McDonald, P.J.; Randall, E.W.; Zick, K. *Polymer* **1994**, *35*, 2744. b) Linossier, I.; Gaillard, F.; Romand, M.; Feller, J.F. *J. Appl. Polym. Sci.* **1997**, *66*, 2465. c) Ouyang, H.; Chen, C.; Lee, S.; Yang, H. *J. Polym. Sci. B: Polym. Phys.* **1998**, *36*, 163. d) Vesely, D. *Macromol. Symp.* **1999**, *138*, 215. e) Sackin, R.; Ciampi, E.; Godward, J.; Keddie, J.L.; McDonald, P.J. *Macromolecules* **2001**, *34*, 890. f) McDonald, P.J.; Godward, J.; Sackin, R.; Sear, R.P. *Macromolecules* **2001**, *34*, 1048.
56. Alfrey, A.; Gurnee, E.F.; Lloyd, W.G. *J. Polym. Sci. C* **1966**, *12*, 249.
57. a) Webb, A.G.; Hall, L.D. *Polym. Comm.* **1990**, *31*, 422. b) Ercken, M.; Adriaensens, P.; Vanderzande, D.; Gelan, J. *Macromolecules* **1995**, *28*, 8541.
58. a) Unnikrishnan, G.; Thomas, S. *Polymer* **1994**, *35*, 5504. b) Aminabhavi, T.M.; Phayde, H.T.S. *Polymer* **1995**, *36*, 1023. c) Mathew, A.P.; Packirisamy, S.; Kumaran, M.G.; Thomas, S. *Polymer* **1995**, *36*, 4935.

59. a) Richman, D.; Long, F.A. *J. Am. Chem. Soc.* **1960**, *82*, 509. b) Fieldson, G.T.; Barbari, T.A.; *Polymer* **1993**, *34*, 1146. c) Balik, C.M.; Xu, J.R. *J. Appl. Polym. Sci.* **1994**, *52*, 975. d) Hong, S.U.; Barbari, T.A.; Sloan, J.M. *J. Polym. Sci. B: Polym. Phys.* **1997**, *35*, 1261. e) Morrissey, P.; Vesely, D. *Polymer* **2000**, *41*, 1865. f) Shin, E.; Ribar, T.; Koenig, J.L.; Wright, N. *Appl. Spectrosc.* **2001**, *55*, 1573.
60. Jiang, W.H.; Han, R. *J. Appl. Polym. Sci.* **2001**, *80*, 529.
61. a) Weisenberger, L.A.; Koenig, J.L. *Appl. Spectrosc.* **1989**, *43*, 1117. b) Webb, A.G.; Hall, L.D. *Polym. Comm.* **1990**, *31*, 425. c) Weisenberger, L.A.; Koenig, J.L. *Macromolecules* **1990**, *23*, 2445. d) Webb, A.G.; Hall, L.D. *Polymer* **1991**, *32*, 2926. e) De Crespigny, A.J.S.; Carpenter, T.A.; Hall, L.D.; Webb, A.G. *Polym. Comm.* **1991**, *32*, 36. f) Asakura, T.; Demura, M.; Ogawa, H.; Matsushita, K.; Imanari, M. *Macromolecules* **1991**, *24*, 620. g) Grinsted, R.A.; Koenig, J.L. *Macromolecules* **1992**, *25*, 1229. h) Grinsted, R.A.; Clark, L.; Koenig, J.L. *Macromolecules* **1992**, *25*, 1235. i) Maffei, P.; Ki  n  , L.; Canet, D. *Macromolecules* **1992**, *25*, 7114. j) Perry, K.L.; McDonald, P.J.; Clough, A.S. *Magn. Reson. Imag.* **1994**, *12*, 217. k) Cody, G.D.; Botto, R.E. *Macromolecules* **1994**, *27*, 2607. l) Hyde, T.M.; Gladden, L.F.; Mackley, M.R.; Gao, P. *J. Polym. Sci. A: Polym. Chem.* **1995**, *33*, 1795. m) Ercken, M.; Adriaensens, P.; Reggers, G.; Carleer, R.; Vanderzande, D.; Gelan, J. *Macromolecules* **1996**, *29*, 5671. n) Laity, P.R.; Glover, P.M.; Barry, A.; Hay, J.N. *Polymer* **2001**, *42*, 7701.
62. Ercken, M. '*Kwalitatieve en kwantitatieve NMR beeldvorming bij het onderzoek van polymere materialen*', PhD dissertation, LUC Diepenbeek, 1996.
63. Crank, J. '*The mathematics of diffusion*', Second Edition, Clarendon Press, Oxford, 1975.
64. Lapcik, L.; Pan  k, J.; Kell  , V.; Polavka, J. *J. Polym. Sci.: Polym. Phys. Ed.* **1976**, *14*, 981.
65. De Candia, F.; Gargani, L.; Renzulli, A. *J. Appl. Polym. Sci.* **1990**, *41*, 955.
66. a) Meares, P. '*Polymers: Structure and Bulk Properties*', Van Nostrand, London, 1965. b) Naylor, T. '*Comprehensive Polymer Science. Vol. 2: Polymer Properties*', Pergamon Press, Oxford, 1989. c) Unnikrishnan, G.; Thomas, S. *J. Polym. Sci. B: Polym. Phys.* **1997**, *35*, 725.
67. Charlesby, A. *Radiat. Phys. Chem.* **1995**, *45*, 955.
68. a) Komoroski, R.A. '*High resolution NMR spectroscopy of synthetic polymers in bulk*', VCH, Florida, 1986. b) Rahman, A. '*Nuclear Magnetic Resonance*', Springer-Verlag, New York, 1986. c) Bovey, F.A. '*Nuclear Magnetic Resonance Spectroscopy*', Academic Press,

Chapter 3

- London, 1988. d) Friebolin, H. *'Basic One- and Two-Dimensional NMR Spectroscopy'*, VCH, Weinheim, 1991.
69. Lubnin, A.V.; Országh, I.; Kennedy, J.P. *J. Macromol. Sci. – Pure Appl. Chem.* **1995**, *A32*, 1809.
70. a) Jansen, C. *'NMR onderzoek naar de moleculaire structuur en dynamica van ethyleen-propyleen copolymeren'*, PhD dissertation, LUC Diepenbeek, 1998. b) Ottenbourgs, B. *'Phenol-formaldehyde resins: a quantitative NMR study of molecular structure and molecular dynamics'*, PhD dissertation, LUC Diepenbeek, 1998. c) Williams, K.R.; King, R.W. *J. Chem. Educ.* **1990**, *4*, A93.
71. Voelkel, R. *Angew. Chem. Int. Ed. Engl.* **1988**, *27*, 1468.
72. Powles, J.G.; Strange, J.H. *Proc. Phys. Soc.* **1963**, *82*, 6.
73. Hahn, E.L. *Phys. Rev.* **1950**, *80*, 580.
74. Meiboom, S.; Gill, D. *Rev. Sci. Instr.* **1958**, *29*, 688.
75. Information retrieved from the internet: a) <http://c1181.camd.lsu.edu/microtomography.html> b) http://srdweb2.dl.ac.uk/srs/OTHER/AN_REPORT/REP94-95/ch2/Microtomography.html c) <http://www.umeciv.maine.edu/landis/XMT/XMTbackground.html>
76. a) Fukumori, K.; Kurauchi, T.; Kamigaito, O. *J. Appl. Polym. Sci.* **1989**, *38*, 1313. b) Blümler, P.; Blümich, B. *Acta Polymer.* **1993**, *44*, 125. c) Fond, C.; Kiefer, J.; Mendels, D.; Ferrer, J.B.; Kausch, H.H.; Hilborn, J.G. *J. Mater. Sci.* **1998**, *33*, 3975.
77. Young, D.G.; Doyle, M.J. *Annu. Technol. Conf. Soc. Plast. Eng.* **1992**, 50th Vol. 1, 1211.
78. Brockett, P.; Levine, A. *'Statistics and Probability and Their Applications'*, Saunders College Publishing, Philadelphia, 1984.
79. Ouddane, M.; Rancourt, Y. *J. Appl. Polym. Sci.* **2001**, *79*, 1178.
80. a) De Candia, F.; Gargani, L.; Renzulla, A. *J. Appl. Polym. Sci.* **1990**, *41*, 955. b) Morrissey, P.; Vesely, D. *Polymer* **2000**, *41*, 1865.
81. a) Young, D.G. *Rubber Chem. Technol.* **1986**, *59*, 809. b) Gent, A.N.; Hindi, M. *Rubber Chem. Technol.* **1990**, *63*, 123. c) Neumeister, L.; Koenig, J.L. *Rubber Chem. Technol.* **1997**, *70*, 271. d) Tsunoda, K.; Busfield, J.J.S.; Davies, C.K.L.; Thomas, A.G. *J. Mater. Sci.* **2000**, *35*, 5187. e) Lake, G.J.; Lawrence, C.C.; Thomas, A.G. *Rubber Chem. Technol.* **2000**, *73*, 801. f) Schneider, M.; Demco, D.E.; Blümich, B. *Macromolecules* **2001**, *34*, 4019. g) Drozdov, A.D. *Polym. Bull.* **2001**, *46*, 215.

82. a) Fukumori, K.; Kurauchi, T. *J. Mater. Sci.* **1985**, *20*, 1725. b) Fukumori, K.; Kurauchi, T.; Kamigaito, O. *J. Appl. Polym. Sci.* **1989**, *38*, 1313.
83. a) Adriaensens, P.; Storme, L.; Carleer, R.; Vanderzande, D.; Gelan, J.; Litvinov, V.M.; Marissen, R. *Macromolecules*, **2000**, *33*, 4836. b) Storme, L. *'Looking at molecular multidomain behavior of polymer systems through NMR-relaxometry'*, PhD dissertation, LUC Diepenbeek, 2001.
84. Meissner, B. *Polymer* **2000**, *41*, 7827.
85. a) Gent, A.N.; Lindley, P.B.; Thomas, A.G. *J. Appl. Polym. Sci.* **1964**, *8*, 455. b) Hamed, G.R. *Rubber Chem. Technol.* **1994**, *67*, 529.

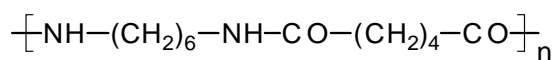
Chapter 4

NMR/MRI study of the water ingress into polyamide 46 plates

4.1. Introduction

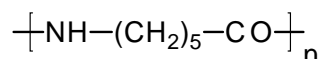
4.1.1. Nylon: a new synthetic fiber

An extensive research in the mid 1930's under the skilful management of Dr. W.H. Carothers at the company Du Pont de Nemours at Wilmington Delaware (US), resulted in the development of a new material: polyamides.¹ An excellent fiber was produced by step-growth polymerization² of a diacid and a diamine. Carothers: "By immersing a cold (glass) stirring rod in the molten mass, upon withdrawal a fine fiber filament could be obtained. It seemed to be fairly tough, not at all brittle and could be drawn to give a lustrous filament."³ The term 'nylon', originally a trade name, has now become a generic term for synthetic polyamides. The numerals that follow distinguish each polymer by designating the number of carbon atoms lying between successive nitrogen atoms of the amide groups in the chain. Thus polyamide 66 (PA66) is prepared from the two monomers hexamethylenediamine and adipic acid and has the structure:



Scheme 4.1: Structure of polyamide 66 (PA66).

with alternative sequences of six and four methylene groups between the amide groups. Polyamide 6 on the other hand, is produced from one monomer by the ring-opening polymerization of caprolactam and has the repeat formula:⁴



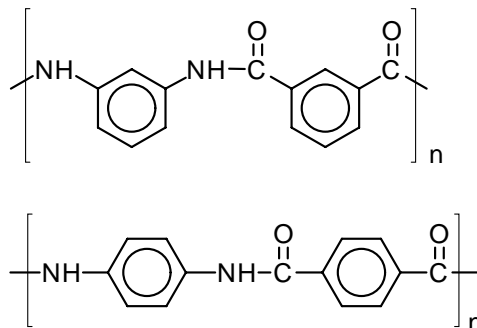
Scheme 4.2: Structure of polyamide 6 (PA6).

Polyamides have the longest history among many synthetic semi-crystalline polymers. They have good strength and toughness and excellent fatigue resistance. Polyamides are attacked by acids, but are stable to alkalis. They are resistant to hydrocarbons and esters, but are dissolved by strongly hydrogen-bonding solvents. Polyamides are extensively used in the form of textile fibers, but also find their applications as plastic mouldings, usually where toughness is a prerequisite. Some examples are: teeth in plastic zip fasteners, castors for light furniture, hopper barrels for food mincers, switch components in telephone exchanges, hose connectors for vacuum cleaners and especially in food processing equipment. They also find wide applications as car components: oil filler caps, connector harnesses in car wiring and even as radiator tank. This latter component is made of PA66, chosen in respect of its high heat distortion temperature, since a radiator tank frequently experiences temperatures above 100 °C and pressures of 90 kNm⁻².⁵

In order to reduce certain disadvantages of polyamides such as dimensional instability, low rigidity and a tendency to brittleness, the polyamides can be reinforced by the introduction of short glass fibers. Grades containing about 15 - 40 % filler show an improved rigidity but retain the capability of being processed as thermoplastics (easy moulding to complex shapes). Electrical insulation and toughness are added advantages. Examples of successful applications include: chain-saw housings, body of an electrical drill, cooling fans for vehicles, handles for garden trimming scissors and electric cooker control knobs. Polyamides also show a low impact strength. This can be overcome by the addition of rubber (frequently ethylene-propylene copolymer elastomer),

which inevitably results in a decrease in rigidity and strength. These rubber-modified polyamides have an impressive list of applications, including a vacuum-cleaner impeller, handle for rotary hammer and gear for the starter mechanism of a lawn mower.⁵

There has been much search for synthetic fiber forming polymers with an excellent stiffness and heat-resistance to make them competitive substitutes for steel wire or glass fibers. They can be used as reinforcing materials in composites or in the production of cables, hoses and coated fabrics.⁶ One of the most successful materials developed for this purpose are the aromatic polyamides, which find their applications as specialty fibers. Nomex[®], derived from m-phenylene diamine and isophthalic acid (Scheme 4.3), is used for re-entry parachutes for space vehicles and in textiles for firefighters' apparel. Kevlar[®], another condensate of p-phenylene diamine and terephthalic acid, is one of the stiffest and strongest organic fibers and provides a unique combination of toughness, extra-high modulus and exceptional thermal stability. Since this polyamide contains para-linked rings exclusively, it is symmetrical and consequently crystalline (Scheme 4.3).⁴

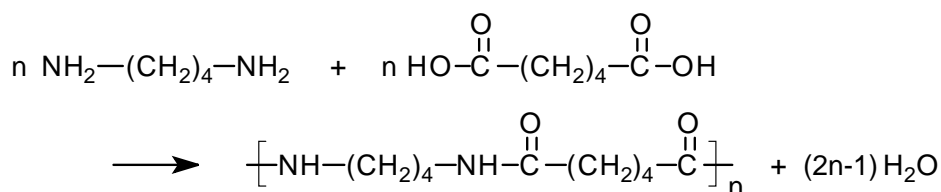


Scheme 4.3: Structure of Nomex[®] and Kevlar[®].

The processing of Kevlar[®] presents special difficulties, which have been overcome by spinning the fiber in the liquid crystal state with sulfuric acid as solvent. Their applications include heat and fragment resistant apparel, brake and transmission friction parts, gaskets, fiber optic cables, circuit board reinforcement, sporting goods and automotive belts. Kevlar[®] is often specified when requirements call for increased strength, reduced weight and/or extended wear life.

4.1.2. Polyamide 46

Polyamide 46 (tetramethylene adipamide), also denoted as nylon 46 or PA46, is an engineering plastic made from tetramethylenediamine and adipic acid (Scheme 4.4). It was first synthesized by Carothers as early as 1938.⁷ Since then, however, PA46 has lost track in contrast to the commercial success of PA6 and PA66 due to the difficulties in obtaining a sufficiently high-molecular-weight polymer while preventing discoloration. Gaymans (a staff member of the Technical University of Twente) and his team succeeded in bridging this difficulty in 1977. He described the preparation of PA46 in a two-step process: first, a low molar mass prepolymer is formed by a polycondensation of adipic acid and tetramethylenediamine at 215 °C under pressure in a steel autoclave. Afterwards, the prepolymer is postcondensed in the solid state at 290 °C or in the melt at 305 °C, resulting in a semi-crystalline material.⁸



Scheme 4.4: Synthesis of polyamide 46 (PA46).

Polyamide 46 is currently marketed by DSM under the trade name Stanyl[®]. Because of the large number of amide groups per unit length of chain compared with other polyamides and the high symmetrical chain structure, a high crystallization rate, higher amount of crystallinity and high melting point (290 °C) and crystallization temperature (260 °C) are obtained.⁸ This results in improved high-temperature physical and mechanical properties such as: high stiffness, good toughness, high creep and fatigue resistance, high resistance against peak temperatures and high thermal and dimensional stability.⁹ The higher crystallization rate of PA46, indicated by the smaller value of ΔT ($= T_m - T_c$), offers the possibility to achieve shorter cycle times with respect to PA6 and PA66 for injection moulded applications. Some characteristics of PA46, compared with the other frequently used polyamides 6 and 66 are presented in Table 4.1.

Table 4.1: Characteristics of PA46, PA66 and PA6.¹⁰

	PA46	PA66	PA6
% crystallinity ^a	60 – 70	50	50 - 60
wt% water uptake ^b	12.4	8.6	9.5
T _g (°C)	80	65	60
T _c (°C)	260	230	180
T _m (°C)	280 - 290	265	220
crystallization rate at 200 °C/min ^c	> 15	6	0.2

^a % crystallinity as determined by WAXS.¹⁰

^b Mass percentage of the water uptake by injection moulded plates at 35 °C.

^c Obtained with DSC: from cooling curves at different scanning speeds can the correlation between crystallization rate (= reciprocal time period at half of the maximal height in the crystallization curve) and crystallization temperature be determined.

These excellent properties make the material suitable for modern electronic and automotive applications.¹¹ The high thermal and dimensional stability and the resistance against peak temperatures make PA46 very well qualified for applications in the close vicinity of an engine where very high temperatures can be reached for a short period. An example is their use as pilot valves in a thermostat, but also as armature protection in an electro-motor. The high temperature properties make the material also suitable for applications where the durability against brazing processes (such as ultrasonic soldering) becomes important. This is the case with the production of spacer sleeves for the electronic printed circuit board. A 30 % glass fiber reinforced PA46 grade is applied for the production of a clutch ring which helps to reduce clutch maintenance in vehicles with a life expectancy of over 150 000 km.

4.1.3. Water absorption by polyamides

All polyamides, however, absorb water because of the amide functionality.¹² The polyamides are 'cross-linked' by hydrogen bonds between the NH and CO groups. In the presence of water, some of these hydrogen bonds are broken and replaced by water molecules, leading to an increasing mobility of the polymer chains and consequently a dimensional change and lowering of the glass

transition temperature (T_g).¹³ A high level of water absorption results in a large drop of T_g . A water absorption of 12.4 % in PA46 results in a drop of T_g from 80 °C down to -40 °C. When T_g drops below room temperature, being the usual test temperature, the polyamides show lower stiffness, higher toughness and lower electrical resistivity¹⁴ since the amorphous phase has been softened by the plasticizing effect of the absorbed water molecules (water is only absorbed by the amorphous phase¹⁵).

In comparison with PA6 and PA66, a lower level of water absorption is expected for PA46 from a fundamental point of view:

- ✓ it is assumed that the amide groups in the polyamides under study have the same affinity to water molecules;
- ✓ the content of amide groups in PA46 is somewhat higher, which is expected to result in a slightly higher water absorption;
- ✓ the crystallinity of PA46 is significantly higher, which is expected to cause a lower water absorption.

Based on calculations that take the two latter differences into account, a lower water absorption was expected for PA46 as indicated in Table 4.2. But surprisingly, gravimetric experiments demonstrate that PA46 absorbs remarkably more water than PA6 and PA66.

Table 4.2: Equilibrium water absorption of injection moulded polyamide plates after immersion in water at 35 °C.¹⁶

	wt% water uptake at 25 °C	% crystallinity	number of mole H ₂ O molecules per 2 mole amide groups in the amorphous phase ^a
PA6	9.5 (measured)	60	3.0
PA66	8.6 (measured)	50	2.2
PA46	7.1 (calculated) ^a	70	2.6
PA46	12.4 (measured)	70	4.5

^a Calculations are presented in the appendix.

4.1.4. Aim and outline of this chapter

Despite the attractive properties of PA46, only a limited number of articles have been published on this polyamide when compared with its direct analogs PA6 and PA66.¹⁷ Few investigations have been carried out on the synthesis and improvements of the mechanical properties,¹⁸ on the study of the lamellar structure and morphology of PA46 crystals¹⁹ and on mass transfer processes during membrane formation.²⁰ In this chapter, we would like to focus on the water ingress into PA46 plates.

As already presented, PA46 absorbs an amount of water that almost doubles the expected amount. More knowledge about the mechanism of water uptake in PA46 plates is of considerable interest because the absorbed water reduces the excellent properties. A second notable feature of the water absorption by PA46 plates is shown in Figure 4.1b. Although the plate is completely saturated with water (as can be concluded from gravimetric experiments), the 1-D projection on top of this water image clearly shows a horn shaped distribution profile in stead of the expected rectangular or block shape. This horn shaped intensity profile even remains after a period of two months in water.

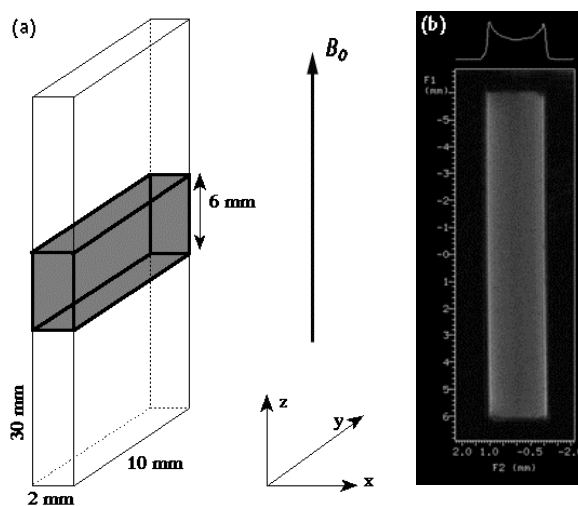


Figure 4.1: (a) Size and position of the PA46 plate with respect to the B_0 field (z-direction) of the magnet. (b) MRI image of a water saturated PA46 plate.

This striking feature insinuates large local differences between the surface and the center of the plates, not only in the amount of absorbed water but also in the molecular mobility of the ingressed water molecules (resembled by the T_2 relaxation time). This can be attributed to various physico-chemical properties, which all have their influence on the water uptake of polyamides: the amount of crystallinity, the crystallization rate, the ordering or density of the amorphous phase, the processing conditions, ... The aim of this study is to look for possible relationships between the physico-chemical properties and the unexpected intensity profile and high amount of water uptake of the PA46 plates. Knowledge about the ingress and distribution of water in the PA46 matrix is of considerable interest to the manufacturers, especially for applications in countries with a climate of high humidity.

The mechanism of water sorption by PA46 is studied by means of gravimetry, MRI imaging and NMR and MRI relaxometry (study of the relaxation decay times). In the first part, a gravimetric study of the water ingress is presented that provides more information on the diffusion mechanism of water into PA46. In the next part, a combined NMR and MRI study of PA46 is presented to obtain more information on the state of water in swollen PA46 plates and to explain the horn shaped MRI intensity projection. In the following part, a model is proposed to explain the unexpected high amount of water sorption by PA46.

The last part of this chapter presents a set of new PA46-co-PA4n copolymers, which have been synthesized in order to retain the excellent properties of PA46 but to reduce the rather large water uptake. In this study, a combination of thermal analysis, gravimetric experiments and MRI and NMR relaxometry is applied to study the water amount, ingress rate and water molecular mobility as a function of the length of the incorporated comonomer.

4.2. A gravimetric study of the water ingress into PA46 plates

4.2.1. Introduction

Processes involving the diffusion of small solvent molecules in polymers occur in nearly every situation wherein polymers are involved.²¹ The presence of small solvent molecules in polymers can have an unwanted effect on their physical and mechanical properties such as tensile strength and fatigue resistance. When solvents come into contact with polymers, the solvent molecules may enter the material and move through the solid matrix by molecular diffusion. The one-dimensional Fickian diffusion process is usually described by using Fick's second law of diffusion:²²

$$\frac{\partial C}{\partial t} = D \frac{\partial^2 C}{\partial x^2} \quad (4.1)$$

where C is the concentration and D is the diffusion coefficient. When the mass of the absorbed solvent is measured as a function of time, a possible solution of equation 4.1 for a plane sheet of thickness l, placed in an infinite bath of solvent, is given by:

$$\frac{\Delta W(t)}{\Delta W_{\infty}} = 1 - \frac{8}{\pi^2} \sum_{m=0}^{\infty} \frac{1}{(2m+1)^2} \times \exp\left[-\frac{D(2m+1)^2 \pi^2 t}{l^2}\right] \quad (4.2)$$

with $\Delta W(t)$ the solvent mass uptake at time t and ΔW_{∞} the absorbed mass at equilibrium.²³

For short periods (small values of t), equation 4.2 can be reduced to:²⁴

$$\frac{\Delta W(t)}{\Delta W_{\infty}} = \frac{4}{l} \left[\frac{D}{\pi} \right]^{1/2} t^{1/2} \quad (4.3)$$

In this case, the diffusion coefficient can be determined from the slope of the plot of $\Delta W(t)/\Delta W_\infty$ as a function of \sqrt{t} . This 'short-time' method can be applied up to a normalized mass uptake $\Delta W(t)/\Delta W_\infty \leq 0.5$ with negligible deviations from the exact solution of Fick's second law.

At long sorption times, all the exponential terms except the first one can be neglected in equation 4.2 and by applying the natural logarithm, equation 4.4 is obtained:²⁵

$$\ln\left(1 - \frac{\Delta W(t)}{\Delta W_\infty}\right) = \ln\left(\frac{8}{\pi^2}\right) - \left(\frac{D\pi^2}{l^2}\right)t \quad (4.4)$$

This equation shows that for longer sorption times ($\Delta W(t)/\Delta W_\infty \geq 0.5$), a plot of $\ln(1-\Delta W(t)/\Delta W_\infty)$ as a function of time gives a straight line and D can be calculated from the slope. This is called the 'long-time' method.²⁶

In studies of the molecular transport of liquids into polymers, diffusion has been classified as Fickian or non-Fickian.²⁷ The diffusion processes that follow equations 4.3 and 4.4 are called Fickian. For the non-Fickian diffusion, the mass uptake is proportional to t^n , where the value of n equals 1 for Case II diffusion or lays in between 0.5 and 1 for anomalous diffusion. Values for n equal to 0.5 thus corresponds to Fickian diffusion.

4.2.2. Gravimetric study of the water ingress into native PA46 plates

Gravimetric sorption is a rather simple and versatile technique to obtain information on the diffusion characteristics of a certain polymer-solvent system. It involves exposing the specimen to solvent and monitoring the change in specimen mass with time. For this purpose, PA46 plates were immersed in distilled water at a constant temperature and the water absorption was followed as a function of time. The mass percentage water uptake (wt%) was calculated according to equation 4.5:²⁸

$$\% \text{ water uptake} = \text{wt}\% = \frac{W_t - W_0}{W_0} \times 100 = \frac{\Delta W(t)}{W_0} \times 100 \quad (4.5)$$

Figure 4.2a shows the % water uptake against the square root of time for a 2 mm plate immersed in water at 35 and 45 °C and for a 4 mm plate at 35 °C. The initial water uptake increases linearly versus square root of time, being indicative for Fickian diffusion.²⁹ The water uptake levels off at about 12.4 %. There is an indication that the water sorption is somewhat reduced at 45 °C but since the difference is rather small in this temperature range, we will not go further into this. Figure 4.2b displays the normalized water uptake curves, obtained by plotting $\Delta W(t)/\Delta W_\infty$ versus $t^{1/2}/l$ for the 2 mm and 4 mm PA46 plate at 35 °C. It is clear that the sorption curves coincide regardless of plate thickness, which points to a similar diffusion coefficient for the 2 mm and 4 mm plate and furthermore confirms Fickian diffusion.²⁹

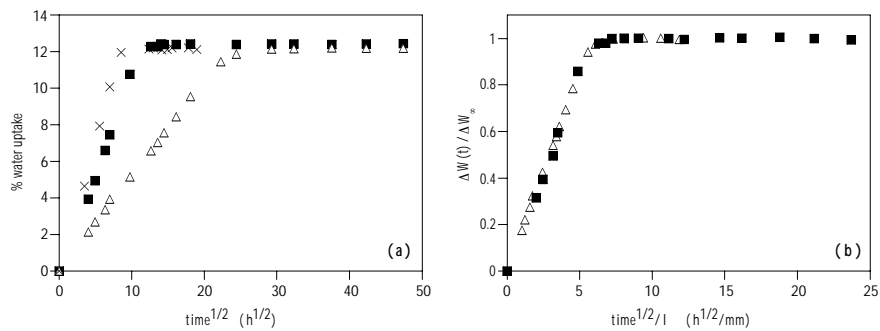


Figure 4.2: (a) Water uptake (in wt%) for PA46 plates as a function of square root of time for a 2 mm plate at (■) 35 °C and (×) 45 °C and (△) for a 4 mm plate at 35 °C. (b) Relative water uptake ($\Delta W(t)/\Delta W_\infty$) versus $t^{1/2}/l$ for (■) a 2 mm plate and (△) a 4 mm plate at 35 °C.

The average diffusion coefficients, calculated by means of equation 4.3, are $1.63 \times 10^{-6} \text{ mm}^2/\text{s}$ and $2.72 \times 10^{-6} \text{ mm}^2/\text{s}$ for the water ingress in PA46 plates at 35 and 45 °C, respectively. On the other hand, the 'long-time' method (equation 4.4) results in a diffusion coefficient of $1.78 \times 10^{-6} \text{ mm}^2/\text{s}$ for the diffusion at 35 °C. At 45 °C, not enough experimental points were available to obtain a good fit.

Figure 4.2a also demonstrates that the rate of water sorption increases with increasing temperature and the activation energy for the diffusion of water in PA46, E_D , can be calculated by using the Arrhenius relation:³⁰

$$D = D_0 \exp\left(\frac{-E_D}{RT}\right) \quad (4.6)$$

in which D_0 is a constant term, R is the gas constant (8.31 J/mole K) and T is the temperature in degree Kelvin. A plot of $\ln(D)$ as a function of $1/T$ results in a value of E_D of 42.6 kJ/mole. This is in the same range as the values found in literature for PA6 (30 kJ/mole)³¹ and PA66 (60 kJ/mole)³².

4.2.3. Gravimetric study of the water ingress into annealed PA46 plates

Since it is generally assumed that water absorption by PA46 only takes place in the amorphous phase¹⁵ and that annealing may influence the organization of the chain fragments in the amorphous phase, it is expected that annealing will affect the amount and ingress kinetics of the water uptake. To study this phenomenon, PA46 plates were annealed (see experimental part 4.6.1.) for different time periods, varying from 15 minutes to 12.5 hour before immersing them in distilled water at 35 °C.

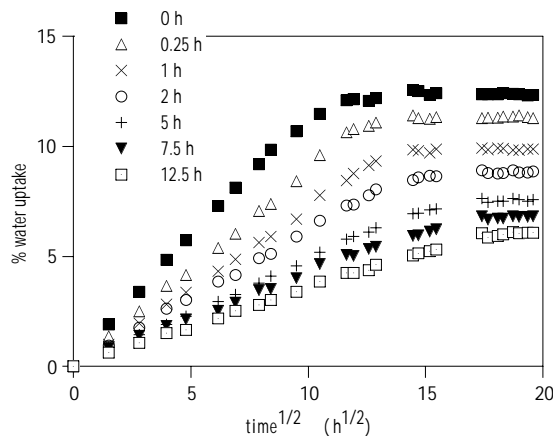


Figure 4.3: Water uptake (in wt%) as a function of square root of time for annealed PA46 plates (2 mm thickness) after different annealing times.

The sorption results in Figure 4.3 clearly show a reduced water uptake with increasing annealing time. The ingress kinetics of water in annealed PA46 still follows a Fickian diffusion regime. Not only the amount of absorbed water decreases but also the rate of water uptake as demonstrated in Table 4.3 by the decreasing diffusion coefficients (D is determined by using the 'short-time' method). The decreased water sorption of polyamides after thermal treatment is also stated in literature³³ and two explanations are possible. Annealing can cause an increase of the crystallinity and the reduced amount of amorphous phase results in a decreased water uptake. As a second interpretation, it can be assumed that the thermal treatment results in a closer coupling of the amide groups in the amorphous regions (or an increased density of the amorphous phase) and as a consequence reduces the tendency to absorb water (see later).

Table 4.3: Equilibrium mass uptake and diffusion coefficients of annealed PA46 as a function of annealing time.

annealing time	wt%	D (mm ² /s)
0 h	12.4 %	1.63×10^{-6}
0.25 h	11.3 %	1.29×10^{-6}
1 h	9.9 %	1.14×10^{-6}
2 h	8.8 %	1.02×10^{-6}
5 h	7.6 %	0.822×10^{-6}
7.5 h	6.9 %	0.718×10^{-6}
12.5 h	6.2 %	0.690×10^{-6}

4.2.4. Conclusion

Gravimetric experiments reveal that the ingress kinetics of water in PA46 plates is Fickian and that the equilibrium mass uptake is about 12.4 %. Annealing tests demonstrate a reduced sorption rate and amount of ingressed water with increasing annealing time. These preliminary results already indicate the important influence of the amorphous phase on the water sorption performance of PA46.

4.3. Quantitative MRI and NMR study of the water uptake by PA46 plates *

4.3.1. Introduction

In order to obtain more information on *a*) the unexpected high amount of water uptake by PA46 and *b*) the conspicuous water distribution profile (Figure 4.1b), there is need for more fundamental knowledge about the various physico-chemical molecular properties which all influence the water uptake.

Nuclear magnetic resonance (NMR) relaxometry has already been proven to be a suitable technique to obtain more information on molecular motions in polymers.³⁴ In this section, the water sorption process in PA46 plates is described by a combination of MRI and NMR relaxation experiments. The ¹H volume-averaged relaxation times of the absorbed water molecules in the water saturated plates are determined by using the CPMG pulse sequence. A deuterium relaxometry study of D₂O saturated plates and a ¹H wideline relaxation time study of dry PA46 are also presented. Spatially resolved information on the concentration and molecular mobility of the ingressed water molecules is obtained by means of MRI relaxation experiments.

4.3.2. Determination of the state of water in swollen PA46 plates

4.3.2.1. Measurement of the volume-averaged ¹H T₂ relaxation times of the absorbed water molecules in saturated PA46 plates

In order to have a good estimate of the T₂ spin-spin decay times of the mobile and semi-rigid molecules like absorbed water and plasticized polyamide, CPMG (Carr Purcell Meiboom Gill)³⁵ experiments were performed on water saturated PA46 at 20 °C. The spectrum, as shown in Figure 4.4, consists of a relatively narrow line, superimposed on a broad resonance. The former is

* Parts of this section have been published: Adriaensens, P.; Pollaris, A.; Carleer, R.; Vanderzande, D.; Gelan, J.; Litvinov, V.M.; Tijssen, J. *Polymer* **2001**, *42*, 7943.

associated with mobile (absorbed) water molecules, while the latter originates from the relatively rigid protons in the plasticized polymer backbone.³⁶

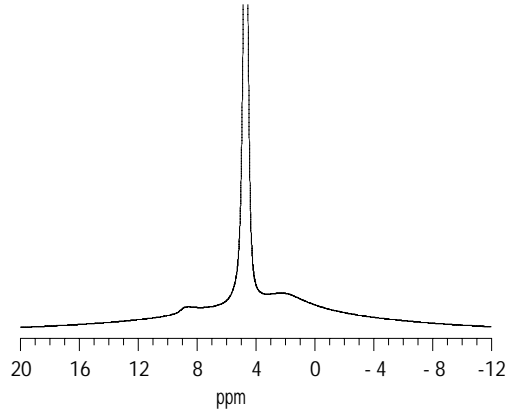


Figure 4.4: ¹H NMR spectrum of water saturated PA46.

A bi-exponential analysis of the experimental data by means of equation 4.7 resulted in a long decay time $T_{2,l}$ of 4 ms and a short one of 1.1 ms ($T_{2,s}$). These experiments were performed at 20 °C, which is 60 °C above the T_g of water saturated PA46 ($T_g = -40$ °C). A similar T_2 experiment on dry PA46 at 140 °C, being also 60 °C above the glass transition temperature of dry PA46 ($T_g = 80$ °C), resulted in only the short T_2 decay time. These experiments allow assigning $T_{2,l}$ to absorbed water and $T_{2,s}$ to plasticized polyamide chains in the amorphous domains.

$$M_t = M_{0,s} \exp\left(-\frac{t}{T_{2,s}}\right) + M_{0,l} \exp\left(-\frac{t}{T_{2,l}}\right) \quad (4.7)$$

Concerning the nature of water in polyamides, some authors propose a two-phase model for the mechanism of water sorption, where they make a distinction between loosely (or free) and strongly bound water molecules.³² On the other hand, Le Huy et al.³⁷ proposed that all water molecules can be regarded as bound in the same way to the amide groups or that fast local exchange takes place between unbound and bound water molecules. In order to obtain more

information on the state of the absorbed water molecules in PA46 and to study if all absorbed water molecules are detected (if strongly bound water is present, it is possible that it is not detected by CPMG), some additional NMR experiments were performed.

4.3.2.2. Quantitative determination of the amount of water in saturated PA46 plates

A straightforward method to judge if all absorbed water molecules are represented by the single decay time $T_{2,1}$, is to compare the amount of water determined by weighing with this derived from slice selective MRI projections in the presence of an internal standard. This was accomplished by acquiring MRI projections of a set-up of a water saturated PA46 plate and a 5 mm NMR tube filled with doped water as a function of TE. The quantitative signal intensities (spin density or M_0) were obtained by extrapolating the projection intensities of both the plate and the tube to TE = 0 by means of equation 4.8:

$$M_t = M_0 \exp\left(-TE/T_2\right) \quad (4.8)$$

The spin density in the slice of the plate was then transformed to mass units on the basis of the known mass (volume) and spin density of water in the slice of the tube. Extrapolating to the total height of the plate resulted in the quantitative amount of water in the plate, measured by NMR. The resulting amount of water is almost equal to that derived by weighing. Any contribution of plasticized PA46 to the water spin density in the plate is avoided by analyzing only signal intensities starting from TE = 6 ms. Reproducible results were obtained in a duplo experiment. This method proves that all absorbed water molecules are measured in the CPMG experiment and that they are represented by the volume-averaged $T_{2,1}$ decay time of 4 ms. So we can conclude that there is only one type of water present, which means that fast local exchange takes place between free and bound water molecules.

4.3.2.3. Volume-averaged solid state deuterium NMR relaxation experiments

In order to obtain extra information on the molecular state of the absorbed water molecules in PA46, some deuterium NMR relaxation experiments were performed. Solid state deuterium NMR has already proven to be a very powerful technique to probe the molecular motions in polymers in general³⁸ and to study the segmental dynamics of polyamides in particular.³⁹ Nuclei with a spin $I \geq 1$ possess an electrical quadrupole moment. The averaging of the quadrupolar interaction of ^2H (or D) nuclei, present in liquid $^2\text{H}_2\text{O}$ (or D_2O), is caused by the fast and isotropic rotation of the D_2O molecules. As a result, the deuterium NMR spectrum consists of an isotropic signal with a narrow Lorentzian line shape. In the case of oriented systems, the D_2O molecules interacting with these systems show an anisotropic motion. This will prevent the complete averaging of the quadrupolar interaction and will cause a splitting of the isotropic signal: the quadrupole splitting.⁴⁰ So D_2O can be used as an indirect probe to study the molecular dynamics, since its deuterium NMR relaxation and spectral features will be dominated by the remaining quadrupolar interaction and thus provides valuable information on the type of motions of the absorbed solvent molecules.

The deuterium quadrupolar wide-line spectra recorded on small pieces of D_2O saturated polyamides, are shown in Figure 4.5. The spectrum of D_2O saturated PA46 recorded with a spectral width of 2 MHz (Figure 4.5a), consists of a sharp line superimposed on a broad Pake pattern. In agreement with Loo et al.⁴¹, the broad Pake pattern arises from N-D moieties which are formed by the exchange of N-H protons of the amide groups in the amorphous phase⁴² and only appears in quadrupolar echo wide-line spectra acquired with a short dwell time ($= 1/\text{sw}$). However, in the longer dwell time FID (Figure 4.5d, $\text{sw} = 40$ kHz) is the broad component no longer detected. The single narrow Lorentzian line indicates a fast isotropic motion and confirms the presence of only one type of water molecules.

The integral intensity ratio of the narrow line to the Pake pattern is 4.4 to 1 in Figure 4.5a, which means that the narrow line represents all water. Indeed, a D_2O mass uptake of 13.6 % and an amorphous PA46 content of 30 % should give a molar ratio D_2O to N-D of 2.27 to 1 (two mole N-D moieties per mole repetition

unit of PA46) or a deuterium integral intensity ratio of 4.5 to 1 (calculation is presented in appendix).

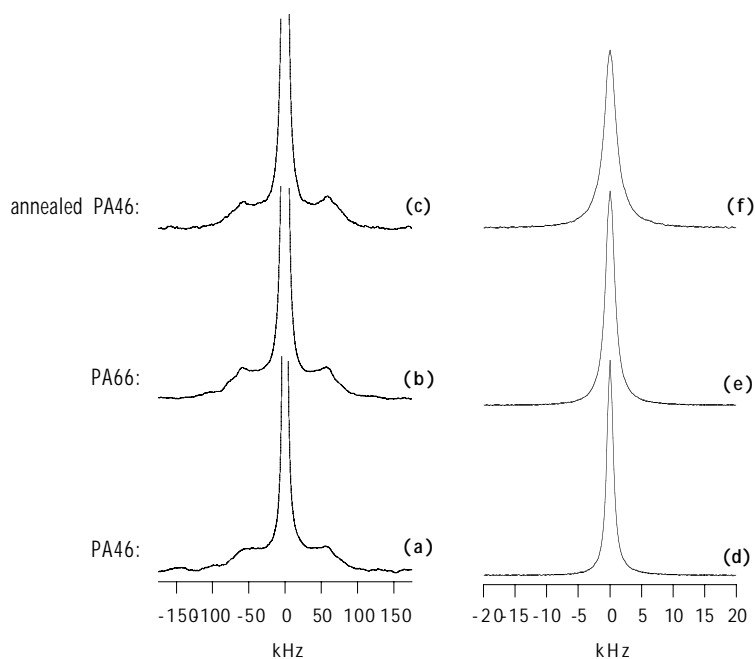


Figure 4.5: Deuterium quadrupolar echo spectra recorded with a spectral width of 2 MHz, of D_2O saturated (a) PA46, (b) PA66 and (c) annealed PA46; and with a spectral width of 40 kHz for (d) PA46, (e) PA66 and (f) annealed PA46.

Hutchison et al.⁴³ performed deuterium NMR studies on PA6 fibers saturated with D_2O . By using a spectral width of 40 kHz, which only selects the semi-rigid and mobile molecules, they did discriminate between a narrow line with a long deuterium T_1 value of 200 ms and a signal showing a remaining quadrupolar splitting of about 3.5 kHz with a short deuterium T_1 value of 3 ms. They assigned both signals to loosely and strongly bound water molecules, respectively. Figure 4.5d shows the quadrupolar echo spectrum of PA46 saturated with D_2O and also recorded with a spectral width of 40 kHz. However, no signal showing a remaining quadrupolar splitting is observed, only the motionally narrowed D_2O line.

Data from the inversion recovery experiments are well described by a mono-exponential decay (equation 4.9, Figure 4.6a), resulting in just a single deuterium T_1 value of 5.5 ms. This is in the same range as the data presented by Loo et al. for PA6 rods saturated with D_2O .⁴¹ The T_1 relaxation time of pure D_2O is measured to be 370 ms (Loo⁴¹: 340ms). This means that the long T_1 component observed by Hutchison et al.⁴³ probably originated from remaining free D_2O which was trapped between the PA6 fibers and which could not be removed by simple drying as was already described by Loo et al.⁴¹. In this study, the D_2O saturated plate was shortly rinsed with water to remove D_2O that is adsorbed at the surface.

$$M_t = M_0 \left(1 - 2 \exp\left(-t/T_1\right) \right) \quad (4.9)$$

The single T_1 relaxation component implies that either the strongly and loosely bound water molecules have a similar T_1 relaxation behavior or that there is only one type of absorbed water in the polymer matrix.^{37a} If a D_2O molecule should be strongly bound between two amide groups, a deuterium NMR spectrum showing a tent-like pattern would be expected. That such a spectrum is not observed suggests that the D_2O molecule is able to exchange fast on the NMR time scale between the bounded and unbounded state.

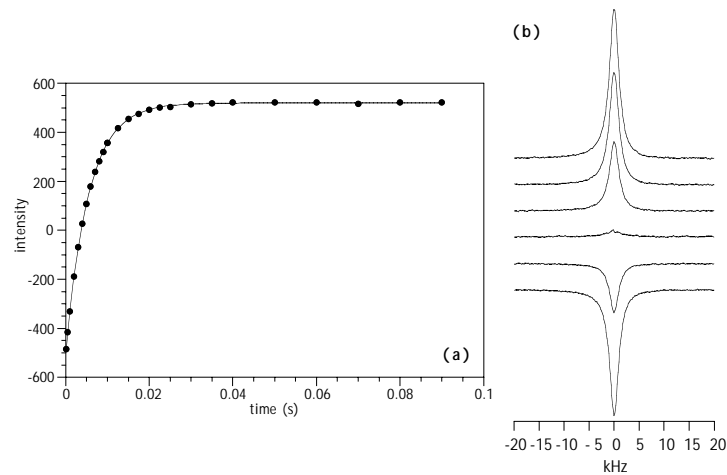


Figure 4.6: (a) The mono-exponential T_1 analysis and (b) deuterium quadrupolar echo inversion recovery experiment of D_2O saturated PA46 (spectral width of 40 kHz).

Besides, in the inversion recovery quadrupolar echo spectra, no indication for multiple relaxation is observed in the proximity of the inversion point as shown in Figure 4.6b. This further confirms that fast local exchange takes place between free water and water molecules associated via hydrogen bonds to the amide groups, which is in agreement with the findings of Mansfield et al.³² and Loo et al.⁴¹ for PA66 and PA6, respectively.

Similar results are observed for PA66 (Figure 4.5b and 4.5e) and for annealed PA46 (Figure 4.5c and 4.5f), all saturated with D₂O.

4.3.2.4. Conclusions

NMR relaxation experiments provide an answer about the physical nature of the absorbed water molecules in PA46 plates. A quantitative analysis demonstrates that all the absorbed water is designated by the single volume-averaged $T_{2,1}$ decay time of 4 ms. Since in the deuterium quadrupolar solid echo spectra, no quadrupole splitting is observed in the D₂O signal and only a mono-exponential D₂O T_1 relaxation behavior is displayed, we can conclude that there is only one averaged state of absorbed water molecules in the PA46 plates and that fast local exchange of water molecules takes place between the bound and the unbound state. This is in contrast to the large-scale molecular diffusion of water molecules, which is of course slow on the NMR time scale.

4.3.3. Explanation of the horn shaped MRI intensity projection

4.3.3.1. MRI morphology of saturated PA46 plates

Magnetic resonance imaging or MRI is an NMR imaging technique that was first proposed by Lauterbur et al. in 1973.⁴⁴ The technique has become very important in materials' research over the last 10 to 20 years since it provides spatial information on various molecular properties. Besides, it enables the production of a map showing the spatial distribution of NMR properties such as spin density or relaxation times.⁴⁵ MRI has proven to be particularly suitable for the research into polymer materials in general⁴⁶ and for the study of solvent

ingress into polymers in particular.⁴⁷ Also a number of MRI studies on the water ingress into polyamide 6 and 66 were already presented.⁴⁸

Spatially resolved MRI experiments were performed in order to study if the water concentration and water molecular mobility are distributed homogeneously throughout the PA46 plates. Figure 4.7a shows the MRI image and 1-D projection of a water saturated PA46 plate. Although the plate is saturated to equilibrium, the intensity of the 1-D projection gradually decreases towards the center of the plate. When the ingress of water is studied as a function of time (Figure 4.8), the reconstructed 1-D projections (see experimental part) clearly show a horn shaped intensity distribution, which appears immediately and remains present even after a period of months in water. The width of these horns is in the order of several tenths of millimeter.

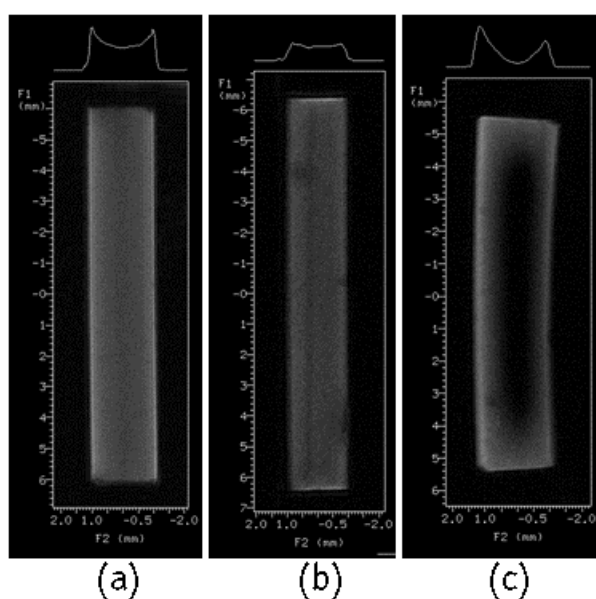


Figure 4.7: MRI images of (a) a saturated PA46 plate, (b) a saturated two-sided polished PA46 plate and (c) a partially saturated one-side polished PA46 plate (right side is polished).

That the horns are intrinsic to the material and not due to magnetic artifacts is demonstrated by interchanging the read and phase direction: the horns clearly remain present. Moreover, Figure 4.7b shows the MRI image of a

water saturated two-sided polished PA46 plate. The horns completely disappear upon polishing and an almost rectangular shaped 1-D projection is obtained. This is further presented in Figure 4.7c, displaying the ingress of water in a one-side polished PA46 plate. The non-polished side (left side) not only shows the high intensity horn but the water ingress is also slower along the polished side (right side). Moreover, the plate bends due to a larger degree of swelling of the original side as compared to the polished side.

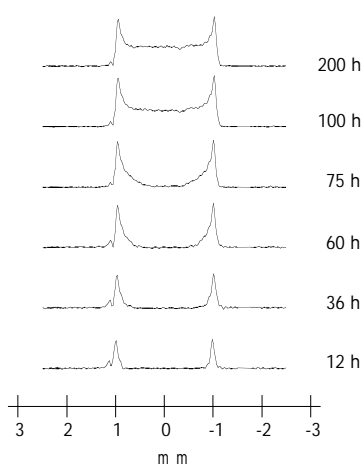


Figure 4.8: 1-D reconstructed projections of MRI images of a 2 mm PA46 plate immersed in water at 35 °C as a function of time. The surrounding free water is suppressed by using the inversion recovery technique.

4.3.3.2. A spatially resolved MRI relaxation analysis of saturated PA46 plates

Image intensity can be a rather complex function of local concentration of water (and plasticized polyamide) and of T_1 and T_2 relaxation times, which are largely affected by molecular motions. To determine whether the previously described horn shaped image intensity distribution is due to concentration and/or relaxation effects and if it can explain the unexpected high amount of water absorption by PA46, a more detailed spatially resolved MRI relaxation study was carried out (see experimental part, section 4.6.4.).

The spatially resolved values of M_0 , T_1 and T_2 for a water saturated PA46 plate are presented in Table 4.4. The T_1 relaxation time is obtained by analyzing the signal intensity as a function of TR by means of equation 4.10.⁴⁹ The T_2 relaxation time is clearly spatially dependent. The high intensity horns at the outer layers of the plate show a bi-exponential T_2 decay (equation 4.11) with a slow and a fast component of respectively 4.5 and 1.2 ms. These can be assigned to absorbed water and plasticized PA46, respectively (cf. section 4.3.2.1.). A gradual decrease of the T_2 value of water is observed in moving from the surface towards the core of the plate (see experimental part). At the core, the data cannot be analyzed bi-exponentially and equation 4.8 results in only a single T_2 value of 3.5 ms.

$$M_t = M_0 \left[1 - \exp\left(-\frac{TR}{T_1}\right) \right] \quad (4.10)$$

$$M_t = M_{0,s} \exp\left(-\frac{TE}{T_{2,s}}\right) + M_{0,l} \exp\left(-\frac{TE}{T_{2,l}}\right) \quad (4.11)$$

Table 4.4: Spatially resolved T_1 , T_2 and M_0 values of water saturated PA46 plates.

	T_1 (s)	T_2 (ms)	M_0^a
horn	0.95	4.5	100
		1.2	32
core	1.17	3.5	85
total projection	1.07	4.0	
		1.2	

^a M_0 values are normalized to 100 for the long T_2 component in the horn.

Analyzing the intensity of the total reconstructed projection also yields two T_2 decay times: $T_{2,s}$ of 1.2 ms and $T_{2,l}$ of 4 ms. The latter is intermediate between the value obtained in the outer layer and core part of the plate and represents the volume-averaged T_2 decay time (cf. section 4.3.2.1.). This means that, although the local exchange between unbound and bounded water molecules is fast on the NMR time scale, the water molecules in the core are more strongly bounded as compared to those at the outer part of the plates.

As far as the spin density of water is concerned (Table 4.4), an excess of about 18 % is observed in the horn ($M_0 = 100$) with respect to the core part ($M_0 = 85$). This excess of water results in an enlarged plasticizing effect on the polymer chains of the amorphous phase in the outer part of the plate and explains why the short T_2 decay time of 1.2 ms is only observed in the outer part of the plate. The protons of the plasticized amorphous phase will, however, only contribute to the signal intensity of images acquired with a short echo time ($TE \ll 5$ ms). For $TE > 5$ ms, the protons of the plasticized matrix will be completely relaxed (see eq. 4.8).

As shown previously in Figure 4.7b, almost no horns appear in the image of a two-sided polished PA46 plate. Besides, a reduced water uptake of about 11.4 % is observed for the two-sided polished plate as shown in Figure 4.9. Since an original 4 mm plate absorbs about 12.4 % water (Figure 4.2a), the outer 1 mm layer of an original plate has to absorb 13.4 % water or about 18 % more than the core part, to give an average water absorption of 12.4 %. So we can conclude that the horns in the MRI images of an original PA46 plate do not only originate from local differences in T_2 , but that there is also a large influence of the higher amount of water in the outer layer of the plate.

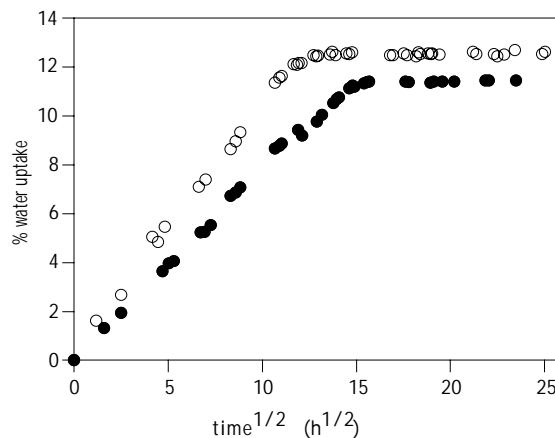


Figure 4.9: Water uptake (in wt%) as a function of square root of time for (○) a native 2 mm PA46 plate and (●) a two-sided polished PA46 plate immersed in water at 35 °C.

In conclusion, it can be stated that the MRI images of a water saturated PA46 plate clearly display a horn shaped intensity distribution with higher intensity regions at the outer layers. A spatially resolved relaxation time study indicates that this profile is engendered by local differences in the water concentration and water molecular mobility. In other words, the horn shaped intensity distribution of water in the MRI images of saturated PA46 plates can be understood by local differences in M_0 and T_2 . These results strongly indicate a difference in morphology of the amorphous phase between the outer layer and core part of the PA46 plates (since water is only absorbed in the amorphous phase).

4.3.3.3. ^1H wideline solid state relaxation time study of different locations of a dry PA46 plate

Proton wideline NMR relaxometry is a very useful technique to study polymer materials. Although the broad proton signal (no line narrowing techniques are used) does not provide chemical shift information, this technique is very sensitive towards the detection of multiphase behavior and molecular mobility.⁵⁰ It is a rather fast technique, which even offers the ability to quantify the percentage of amorphous and crystalline components in polymers.⁵¹

The results of proton solid echo wideline experiments, carried out on the core material and on a 100 and a 350 μm scraped outer layer of a dry native PA46 plate are presented in Table 4.5. The T_2 decay time results at ambient temperature, determined by analyzing the FID to an Abragam function (equation 4.12),⁵² show that below the glass transition no differences in molecular mobility are observed between the three specimens. A similar T_2 decay time of about 15 μs is observed for all specimens and is characteristic for a rigid crystalline or glassy amorphous phase. At 170 $^\circ\text{C}$, being almost 100 $^\circ\text{C}$ above T_g , the solid echo decay has to be analyzed by the sum of a rigid (Weibullian)⁵³ and a more mobile (exponential) component (equation 4.13). The short component ($T_{2,s}$) can be attributed to the crystalline phase while the pure exponential decay ($T_{2,l}$) denotes the amorphous component. The fraction of the rigid component ($M_{0,s}$) is in the same range as the amount of crystallinity (ca. 60-70 %) for PA46 as determined by WAXS (Table 4.1). The differences in the amount of crystallinity between core

and surface layer are small and cannot explain the excess of 18 % more water in the horn (section 4.3.3.2.).

$$M_t = M_0 \exp\left[-0.5*a\left(\frac{t}{T_2}\right)^2\right] * \frac{\sin\left[b\left(\frac{t}{T_2}\right)\right]}{b\left(\frac{t}{T_2}\right)} \quad (4.12)$$

with a and b constants

$$M_t = M_{0,s} \exp\left[-\left(\frac{t}{T_{2,s}}\right)^\alpha\right] + M_{0,l} \exp\left(-\frac{t}{T_{2,l}}\right) \quad (4.13)$$

where $\alpha = 1.9 \pm 0.11$

Table 4.5: Solid echo 1H T_1 and T_2 values at 20 and 170 °C for different parts of a dry native PA46 plate.^a

	20 °C	170 °C	
core	$T_1 = 2.28$ s	$T_1 = 1.52$ s	
	$T_2 = 14$ μ s	$T_{2,s} = 19$ μ s	(66 %)
		$T_{2,l} = 96$ μ s	(34 %)
350 μm surface layer	$T_1 = 1.98$ s	$T_1 = 1.47$ s	
	$T_2 = 17$ μ s	$T_{2,s} = 20$ μ s	(64 %)
		$T_{2,l} = 75$ μ s	(36 %)
100 μm surface layer	$T_1 = 1.80$ s	$T_1 = 1.24$ s	
	$T_2 = 14$ μ s	$T_{2,s} = 20$ μ s	(64 %)
		$T_{2,l} = 66$ μ s	(36 %)

^a Errors indicate the 95 % confidence interval of the non-linear least squares fits and the average values are 0.02 s for T_1 at 20 and 170 °C, 0.05 μ s for T_2 at 20 °C, 0.1 μ s for $T_{2,s}$ and 2 μ s for $T_{2,l}$ at 170 °C and about 1 % for their relative fractions.

The T_1 relaxation times, measured by using the inversion recovery solid echo sequence, are analyzed mono-exponentially (eq. 4.9) at ambient temperature as well as at 170 °C. At temperatures below T_g , a single exponential proton T_1 relaxation time is often observed in heterogeneous materials because of efficient spin-diffusion.⁵⁴ The T_1 value of the core always exceeds the T_1 value of

the 100 μm surface layer, while the T_1 value of the 350 μm surface layer is intermediate. These experiments confirm the difference in morphology between the outer layer and core part of the PA46 plates.

4.3.3.4. Gravimetric and differential scanning calorimetry experiments

Further indications of the difference in morphology between the core and outer part of PA46 plates are given by gravimetric analysis and DSC. The previously presented Figure 4.9 displayed the water uptake against the square root of time for an original 2 mm plate and a two-sided polished PA46 plate. Besides a lower equilibrium mass uptake, the rate of water sorption for the polished plate is roughly half that of an original plate: $0.8 \times 10^{-6} \text{ mm}^2/\text{s}$ versus $1.63 \times 10^{-6} \text{ mm}^2/\text{s}$ at 35 °C (determined by using the 'short-time' method). However, the difference in morphology between horn and core is not caused by a difference in the amount of crystallinity. DSC measurements on the core part and the 100 μm scraped surface layer show no difference in the amount of crystallinity as can be concluded from an identical melting enthalpy (94 J/g) and melting temperature (282 °C). Also the solid state ^1H wideline experiments at 170 °C were pointing in this direction.

Since sorption of water only takes place in the amorphous regions¹⁵ and the amount of amorphous phase is supposed to be constant over the total cross-section of the plate, the differences in water content and sorption rate between an original and a two-sided polished plate again indicate a difference in morphology between the amorphous phase of the horn and core part of the PA46 plates. It is suggested that the mean distance between the amide groups in the amorphous phase is different in the outer and core part of the plates. This affects the strength of the hydrogen bonds between the amide groups and results in a gradual increase of water amount (M_0) and water molecular mobility (T_2) from the core to the surface part of the PA46 plate.

4.3.3.5. Intensity calibrated MRI images and projections

The difference in morphology between horn and core is further demonstrated by intensity calibrated MRI images (calibrated by means of a reference capillary, see experimental part). Figure 4.10 presents the reconstructed 1-D projections, recorded with TE = 1.25 ms and 5 ms, of an original, a two-sided polished and an annealed PA46 plate and an original PA66 plate, all saturated with water.

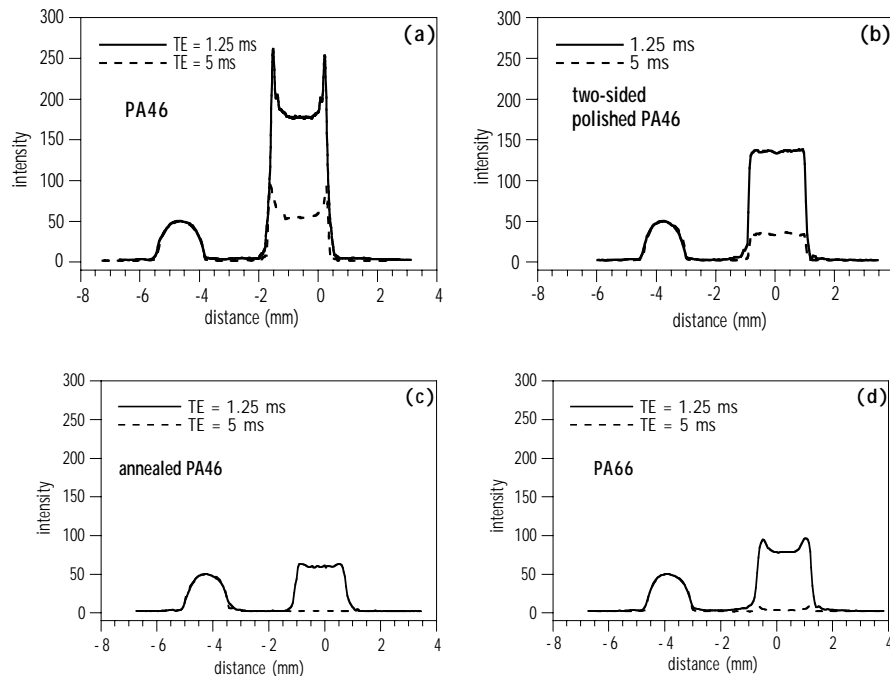


Figure 4.10: 1-D reconstructed projections of MRI images, recorded with TE = 1.25 ms and 5 ms, of (a) an original 2 mm PA46 plate, (b) a two-sided polished PA46 plate, (c) an annealed PA46 plate and (d) an original PA66 plate, all after immersion in water for one month. The reference capillary is displayed on the left side of the projections.

The volume-averaged T_1 and T_2 relaxation times are presented in Table 4.6. By means of the water mass uptake (Table 4.6) and the (local) T_2 values presented in Tables 4.4 and 4.6, the intensities of the 1-D projections shown in Figure 4.10 can be explained by means of equation 4.8. For native PA46 is the

intensity of the horns in the projection acquired with TE = 1.25 ms (Figure 4.10a) higher than its value calculated from the water content and T_2 relaxation time (calculations in the appendix). This can be explained easily, since with a short TE of 1.25 ms, also a fraction of the plasticized polyamide with $T_2 = 1.2$ ms is observed in the horn. As mentioned before, the two-sided polished plate (Figure 4.10b) displays an almost rectangular profile.

Table 4.6: Water content and volume-averaged T_1 and T_2 relaxation times for different polyamides saturated with water.

	wt% water at equilibrium	T_1 (s)	T_2 (ms)
original PA46	12.4	1.07	4.0 1.2
two-sided polished PA46	11.4	1.28	2.8
annealed PA46	6.2	2.22	1.4
PA66	8.6	1.36	1.4

Annealing the PA46 plates has a drastic influence on the image intensity as demonstrated in Figure 4.10c. Although an annealed PA46 plate contains about 6.2 % water and the amount of crystallinity remains almost constant upon annealing,¹⁰ almost no image intensity is observed in images recorded with TE = 5 ms. Signal intensity is only detected with a shorter echo time of 1.25 ms. Although fast local exchange of water molecules still takes place after annealing (Figure 4.5c and f), the average T_2 relaxation time of the absorbed water molecules decreases to such an extent ($T_2 = 1.4$ ms) that no signal is observed at TE = 5 ms. This confirms that chain arrangement in the amorphous phase rather than the amount of amorphous phase determines the observed signal intensity since it affects the average molecular mobility and amount of absorbed water molecules. Furthermore, the horns are quasi absent in the MRI projection of the annealed PA46 plate. Also in saturated PA66 plates, containing 8.5 % water and having a crystallinity of 50 %, almost no signal intensity is observed in images recorded with TE = 5 ms (Figure 4.10d). This in contrast to images acquired with TE = 1.25 ms that also tend to show the horn shaped intensity distribution, but to a lesser extent as for PA46.

4.3.4. Proposed model to explain the unexpected high amount of water sorption by PA46 and confirmation by density measurements

The higher water absorption and water mobility in PA46 as compared to PA6 and PA66 is explained by the very high crystallization rate of PA46 (Table 4.1), together with the fast cooling from the melt to the temperature of the mould. This prevents a mutual chain arrangement in the amorphous phase, i.e. a close coupling of amide groups in the amorphous phase, resulting in a gradual decrease of the amorphous density from the core towards the outer parts of the plates. This difference in amorphous density is especially observed at the outer part of the plate due to the faster cooling in the mould. It is suggested that the average distance between the amide groups in the amorphous phase of PA46 is somewhat larger as compared to PA6 and PA66, resulting in an increased water absorption and a higher molecular mobility of the absorbed water molecules. This explains the presence of the high intensity horns at the outer layer of the PA46 plates. Local fluctuations in the average density and orientation of the amorphous phase of polyamides, varying with the processing conditions, have also been postulated in literature.⁵⁵

The concept of the relationship between water absorption and density of the amorphous phase in PA46 is confirmed by WAXS (wide-angle X-ray scattering) and density measurements.¹⁰ Figure 4.11 shows the density of the crystalline phase ρ_c (determined by WAXS) and the overall density ρ (determined via gradient column) for PA46 as a function of annealing time. The density of the amorphous phase, ρ_a , can be calculated from the overall density, the crystalline density and an average crystallinity of 70 % for PA46. This figure clearly presents that the amorphous density increases significantly as a function of the annealing time. The amount of crystallinity and the density of the crystalline phase on the other hand, remain almost constant upon annealing.

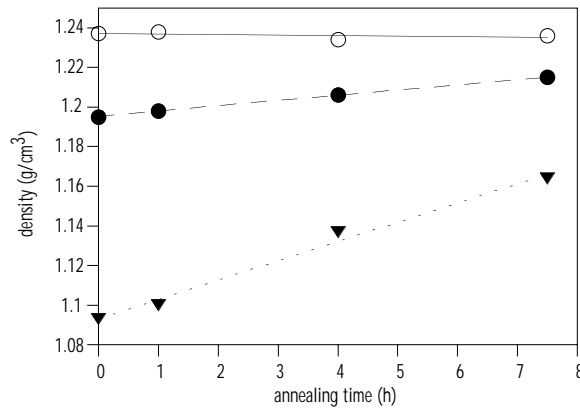


Figure 4.11: Density of (▼) the amorphous phase ρ_a , (○) the crystalline phase ρ_c and (●) the overall density ρ (in g/cm³) of PA46 plates as a function of the annealing time.

The concept furthermore explains the reduced water uptake after annealing. During annealing at 260 °C, the amorphous phase can rearrange into a more structured dense state, resulting in a substantial decrease of the water uptake and molecular mobility of the absorbed water molecules. This rearrangement is especially pronounced at the surface layers of the PA46 plates and consequently, the high intensity horns at the outer layers almost disappear after annealing (Figure 4.10c). Because of the higher crystallinity of annealed PA46, the total water uptake after annealing is substantially lower than for PA66 as shown in Table 4.7. When related to the amorphous phase, however, the water uptake of PA66 and annealed PA46 are comparable.

Table 4.7: Water absorption by native PA46, annealed PA46 and native PA66 plates.

	wt% water at equilibrium	% amorphous phase	water content in the amorphous phase (wt%)
original PA46	12.4	30	41
annealed PA46	6.2	30	21
PA66	8.6	50	17

The gradient in the amorphous density further explains the disappearance of the horns for the two-sided polished plate. By removing 1 mm from each side

of a 4 mm plate, only the central core with a higher amorphous density remains. However, Table 4.6 shows a reduced T_2 relaxation time for the absorbed water molecules in the two-sided polished plate as compared to the water in the core of an original PA46 plate (Table 4.4). Also the MRI signal intensity of the two-sided polished plate is smaller compared to this of the core of the original plate (Figure 4.10b and a respectively). Also this can be explained by the thermal gradient in the mould: the core of a thicker 4 mm plate is cooled more slowly and allows a better rearrangement of the polymer chains in the amorphous phase as compared to the chains in the core of an original 2 mm plate.

4.3.5. Conclusions

MRI and volume-averaged ^1H and ^2H NMR relaxation experiments are performed to study the water absorption in injection moulded PA46 plates. Proton and deuterium relaxation results suggest a fast local exchange (on the NMR time scale) between free water and water molecules bound via hydrogen bonds to the amide groups. MRI results reveal a horn shaped intensity distribution with a gradual decrease in the amount and molecular mobility of the absorbed water molecules from the surface towards the core part of the PA46 plates. This can be explained by the substantially higher crystallization rate of PA46 compared to the other polyamides, hampering the close coupling of amide groups in the amorphous phase and resulting in a larger mean distance between the amide groups in the amorphous phase of PA46. PA46 therefore absorbs a significantly higher amount of water and the absorbed water molecules have a higher molecular mobility (T_2) as compared to PA66.

These differences are noticeably larger in the outer parts of the PA46 plates, due to the faster cooling to the temperature of the mould. Annealing of PA46 causes an increase of the amorphous density (confirmed by WAXS and gradient column), resulting in a strongly reduced water molecular mobility and amount of water uptake. In comparison with PA66, annealed PA46 shows an almost equivalent water uptake when related to the amorphous phase, but the total water uptake is significantly lower because of the higher amount of crystallinity.

4.4. Polyamide 46-based copolymers: reduction of the water absorption

4.4.1. Introduction

As previously presented, PA46 is a versatile synthetic engineering plastic with high tensile strength, toughness and good processable. However, the results above already demonstrated that PA46 is very sensitive to water absorption, which causes plasticizing.¹³ This has a profound effect on the mechanical properties of the polymer¹⁴ and limits its applications in many areas. So it would be advantageous to reduce the water uptake of PA46 while the excellent properties are retained.

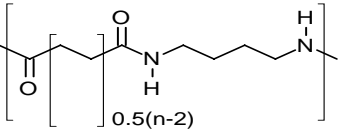
In literature, several methods were already presented to reduce the moisture uptake of polyamides. Chapman et al.⁵⁶ modified the polyamide main chains by the introduction of fluorinated components but this also influences the bulk properties of the polymer. Zhang and coworkers⁵⁷ used surface graft copolymerization on PA66 films to reduce the moisture sorption. The key advantage of this technique is that the polymer surface can be modified toward different properties through the choice of different monomers while the bulk properties of the polymer remain intact. Various other studies have been published describing a number of copolymers of polyamide with PET, polyethers and polyimides.⁵⁸ Pae et al. demonstrated that the moisture resistance of polyimide/polyamide 6 triblock copolymers is better than that of pure PA6, due to the hydrophobic nature of polyimides.⁵⁹

Gaymans et al.⁶⁰ already described a copolyamide of polyamide 46 and polyamide 4T (terephthalamide), which displayed a reduced water absorption with increasing PA4T content. Recently, copolymers of PA46 and PA4n with 4 mole % of $n = 8, 12$ and 16 (PA46-co-PA4n) have been developed by DSM Research Geleen. In this section, a study of these copolymers by means of thermal analysis, gravimetry, NMR and MRI relaxometry is presented. The main goal is to obtain more information on the impact of the chain length of the incorporated linear aliphatic dicarboxylic acid comonomers on the phase composition and water uptake of the PA46 copolymers.

4.4.2. The PA46-co-PA4n copolymer samples

The PA46-co-PA4n copolymers with 4 mole % of $n = 8, 12$ and 16 are presented in Table 4.8.

Table 4.8: Description of the PA46-co-PA4n copolymers.

		
[CH ₂]/[amide] ratio		
PA46	100 % $n = 6$	4.00
PA46-co-PA48	96 % $n=6$; 4 % $n=8$	4.04
PA46-co-PA412	96 % $n=6$; 4 % $n=12$	4.12
PA46-co-PA416	96 % $n=6$; 4 % $n=16$	4.20

The thermal analysis results of these copolymers are presented in Table 4.9. With respect to PA46, the melting temperatures (T_m) of the copolymers are all 5 °C lower, indicating that the molar concentration of the comonomer determines the decrease of the melting temperature. There seems to be a slight increase in crystallization temperature (T_c) of the copolymers with increasing comonomer length, suggesting that an increase of n results in an increased crystallization rate. A possible explanation is that an enhanced mobility of the PA46 segments is realized in the melt since the longer aliphatic units will disturb the hydrogen bond arrangement. The melting enthalpies (ΔH_m) are comparable for all copolymers within experimental error.

Table 4.9: Thermal characteristics of PA46 and PA46-co-PA4n copolymers.

	T_m (°C)	T_c (°C)	ΔH_m (J/g)
PA46	290	268	91
PA46-co-PA48	285	262	89
PA46-co-PA412	285	263	91
PA46-co-PA416	285	264	87

4.4.3. Study of the water ingress into PA46-co-PA4n by gravimetry

A gravimetric analysis of the water uptake by native and annealed PA46 and PA46-co-PA4n copolymers was performed at 50 °C. To study the influence of temperature on the ingress kinetics, native PA46 was also saturated at 30 °C and 70 °C. The sorption curves in Figure 4.12a-c show the normalized water uptake = $(W_t - W_0)/(W_{eq} - W_0)$ as a function of square root of time. The equilibrium water uptake (wt%) (eq. 4.5) and the 'short-time' diffusion coefficient D (eq. 4.3) are presented in Table 4.10 and 4.11, respectively, for the native and the annealed specimens and in Table 4.12 for PA46 as a function of temperature.

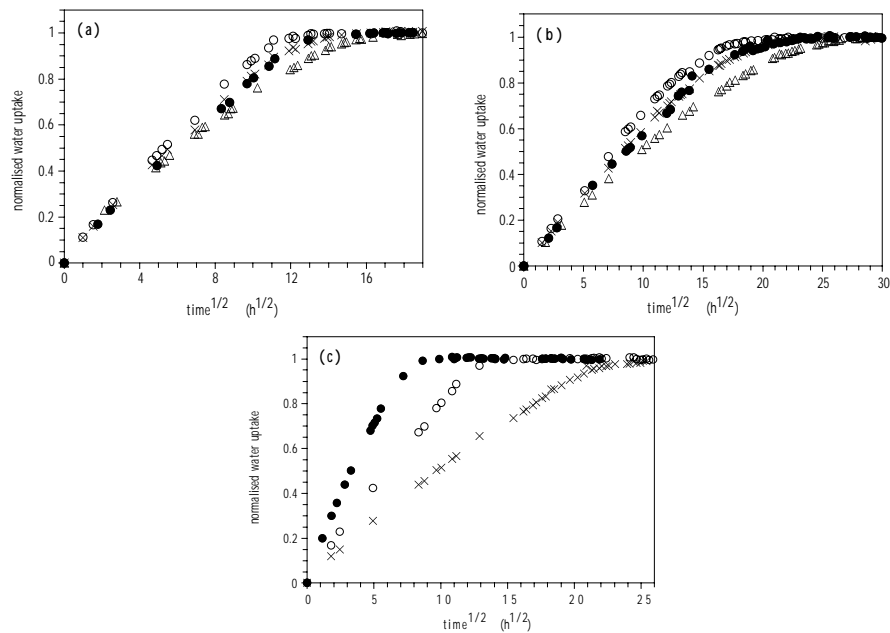


Figure 4.12: Normalized water uptake at 50 °C as a function of square root of time for (a) native and (b) annealed specimens: PA46 (●) and the PA46-co-PA4n copolymers with $n = 8$ (○), $n = 12$ (×) and $n = 16$ (△). Figure (c) represents the normalized water uptake at (×) 30 °C, (○) 50 °C and (●) 70 °C for PA46 as a function of square root of time.

The results in Table 4.10 show a clear difference in equilibrium water uptake and rate of water sorption for the different native polyamides. The

linearity of the initial stage of the water uptake in Figure 4.12a indicates a Fickian diffusion²⁹ and allows determining the average diffusion coefficient. The amount of water absorption and the diffusion coefficient clearly decrease with increasing chain length of the comonomer in the copolyamide series. This is also observed by Kiyotsukuri et al. for copolymers of PA66 with 2,2-dialkyl-1,3-propanediols: the water absorption decreases with increasing length of the alkyl side chain in the comonomer.⁶¹ Compared to PA46, only the copolyamide PA46-co-PA416 shows a clear reduction in water uptake and diffusion coefficient. It should further be remarked that there is a slight difference in the amount of water uptake at equilibrium between the reference PA46 used in this section (Table 4.10) and the PA46 used in the previous sections. This is probably due to a small difference in the production procedure: while the plates used in sections 4.1 to 4.3 are from a commercial bath, the plates used here are prepared on lab scale. Also a small contribution due to the difference in plate thickness (2 mm vs. 3.4 mm) cannot be excluded.

Table 4.10: Gravimetric results for native water saturated PA46 and PA46-co-PA4n plates.

	n = 6 (PA46)	n = 8	n = 12	n = 16
wt%	11.7 %	12.5 %	10.8 %	9.6 %
D (mm ² /s)	4.1 × 10 ⁻⁶	4.8 × 10 ⁻⁶	4.1 × 10 ⁻⁶	3.4 × 10 ⁻⁶

A big change in water sorption is observed upon annealing as demonstrated in Table 4.11. Annealing strongly reduces the water uptake and the water ingress rate (Figure 4.12b) as compared to the native injection moulded plates. Also for the annealed plates, the water amount and water ingress rate decrease with increasing chain length of the incorporated comonomer. However, compared to the very large reduction in water uptake of PA46 upon annealing (factor 3.1), the copolyamides show a somewhat less pronounced drop in water uptake (factor 2.5).

Table 4.11: Gravimetric results for annealed water saturated PA46 and PA46-co-PA4n plates.

	n = 6 (PA46)	n = 8	n = 12	n = 16
wt%	3.8 %	5.3 %	4.0 %	3.8 %
D (mm ² /s)	2.1 × 10 ⁻⁶	2.9 × 10 ⁻⁶	2.1 × 10 ⁻⁶	1.9 × 10 ⁻⁶

Figure 4.12c demonstrates the influence of temperature on the water ingress in PA46. As expected, the water ingress rate becomes higher upon raising the temperature as demonstrated by the diffusion coefficients presented in Table 4.12. Analyzing the diffusion coefficients according to the Arrhenius equation (eq. 4.6) results in an activation energy of diffusion E_D of 46.8 kJ/mole. In agreement with literature,⁶² the equilibrium amount of absorbed water drops slightly with higher temperature, which is an indication of a thermal dependency of the polymer/solvent interactions. Within the 40 °C temperature range used in this study, the temperature dependence of the solubility coefficient S (in g water/g polymer) follows an Arrhenius-type relationship (equation 4.14):

$$S = S_0 \exp\left(\frac{-\Delta H_s}{RT}\right) \quad (4.14)$$

A plot of the logarithm of the solubility as a function of reciprocal temperature yields the partial molar heat of solution $\Delta H_s = -1.5$ kJ/mole. This exothermic sorption explains the decrease in solubility with increasing temperature.⁶³

Table 4.12: Gravimetric results for water saturated PA46 as a function of temperature.

	T = 30 °C	T = 50 °C	T = 70 °C
wt%	12.2 %	11.7 %	11.4 %
D (mm ² /s)	1.5 × 10 ⁻⁶	4.1 × 10 ⁻⁶	12.7 × 10 ⁻⁶

4.4.4. NMR relaxometry of the native PA46-co-PA4n copolymers

As already presented, solid state proton wide-line NMR provides a sensitive probe to study the microphase structure and molecular motions in semi-crystalline polymers. Different phases, having different molecular chain mobilities and their relative fractions can be directly estimated from the analysis of the spin-spin relaxation decay time curve.⁶⁴

¹H wide-line T₂ relaxation experiments were performed by Dr. V.M. Litvinov at DSM Research Geleen. The data were analyzed by using (a) a Weibull function at temperatures below 80 °C (equation 4.15), (b) a linear combination of a Weibull and exponential function at temperatures between 80 and 120 °C (equation 4.13) and (c) a linear combination of a Weibull and two exponential functions at temperatures above 120 °C (equation 4.16).⁵³

$$M_t = M_{0,s} \exp\left[-\left(\frac{t}{T_{2,s}}\right)^\alpha\right] \quad (4.15)$$

$$M_t = M_{0,s} \exp\left[-\left(\frac{t}{T_{2,s}}\right)^\alpha\right] + M_{0,i} \exp\left(-\frac{t}{T_{2,i}}\right) + M_{0,l} \exp\left(-\frac{t}{T_{2,l}}\right) \quad (4.16)$$

$$\text{where } \alpha = 1.9 \pm 0.05$$

The relative fraction of the relaxation components, as designated in the text by %T_{2,index} = (M_{0,index} / (M_{0,s} + M_{0,i} + M_{0,l})) × 100, represents the fraction of hydrogen atoms in phases with different molecular mobility, where subscripts 's', 'i' and 'l' stand for short, intermediate and long component.

To find out the most suitable temperature for the characterization of the phase composition of PA46 and its copolymers, the ¹H T₂ relaxation behavior was measured as a function of temperature for PA46 and the results are presented in Figure 4.13. The FID below 80 °C can be described by a single decay time T_{2,s} of about 13 μs, a value typically for crystalline and glassy amorphous material. A second relaxation component with a longer decay time appears at 80 °C. Upon increasing the temperature, the fraction of rigid material that is composed of crystalline and rigid amorphous phase, decreases at the expense of the semi-rigid amorphous phase.

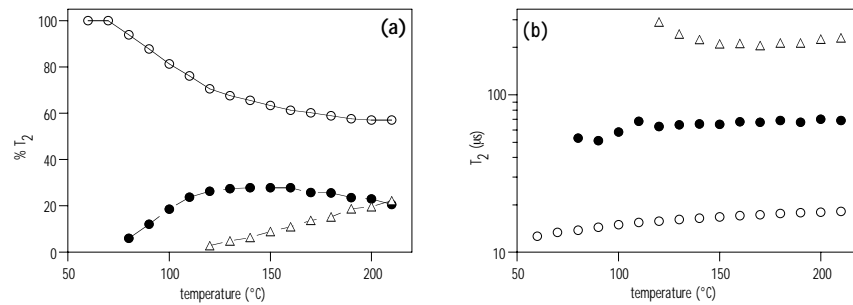


Figure 4.13: (a) Temperature dependence of the T_2 fractions representing the different molecular chain mobility in PA46 and (b) the T_2 decay times corresponding to these fractions. The different decay times are denoted as (O) short, (●) intermediate and (Δ) long.

Above 120 °C, the FID can be described by three distinct components. The T_2 value of the third component ($T_{2,l}$) is significantly longer as compared to $T_{2,i}$ and is assigned to the mobile amorphous phase. Upon further temperature increase, the fraction of $T_{2,l}$ increases at the expense of the semi-rigid amorphous phase, whereas the rigid fraction of PA46 reaches nearly a constant value above 180 °C. It appears that above this temperature, the $T_{2,s}$, $T_{2,i}$ and $T_{2,l}$ decay times originate from the relaxation of the crystalline phase, the semi-rigid crystal-amorphous interface and the soft amorphous phase, respectively. The relative fractions $\%T_{2,s}$, $\%T_{2,i}$ and $\%T_{2,l}$, represent the hydrogen content of these phases. As an example, the T_2 decay at 200 °C for PA46-co-PA48 is shown in Figure 4.14.

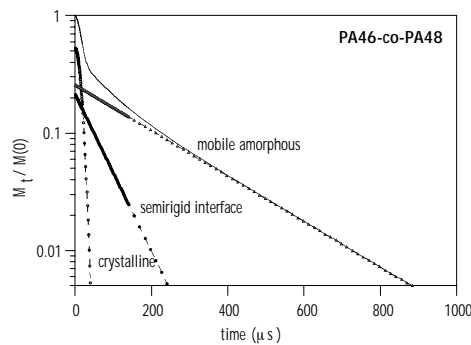


Figure 4.14: The transverse magnetization decay for PA46-co-PA48 at 200 °C, as measured with the solid echo method.

The T_2 relaxation characteristics at 200 °C are presented in Table 4.13 for all specimens. No large differences in molecular mobilities are observed between the samples. As previously mentioned, this NMR relaxation method provides a value of the crystallinity, which is usually in good agreement with that measured by other techniques. For PA46, a crystallinity of about 57% is determined by proton wideline NMR, which is comparable with a value of 60-70 % as determined by WAXS.¹⁰ Table 4.13 also demonstrates that the amount of crystalline phase of the copolyamides is a few percents lower as compared to PA46 and that no variation with the chain length is observed within experimental error. This slight decrease of crystallinity ($\%T_{2,s}$) suggests that the comonomer chain units are rejected from the crystalline phase. As a result, the fraction of the most mobile amorphous phase ($\%T_{2,i}$) seems to be slightly larger for the copolyamides as compared to PA46.

Table 4.13: The 1H T_2 relaxation characteristics for the specimens under study at 200 °C.^a

	n = 6 (PA46)	n = 8	n = 12	n = 16
$T_{2,s}$ (μ s)	18.0	18.0	18.1	18.0
$T_{2,i}$ (μ s)	72	65	73	66
$T_{2,l}$ (μ s)	244	224	263	250
$\%T_{2,s}$	56.7	52.8	54.3	53.0
$\%T_{2,i}$	23.1	21.4	23.5	22.0
$\%T_{2,l}$	20.2	25.8	22.2	25.0

^a The average errors of the non-linear least squares fit are 0.1 μ s for $T_{2,s}$, 4 μ s for $T_{2,i}$, 7-9 μ s for $T_{2,l}$ and 1 % for the relative fractions.

4.4.5. Spatially resolved MRI relaxometry of the water saturated PA46-co-PA4n copolymers

MRI experiments on water saturated plates were performed to obtain information on the spatial distribution of the water molecules and the water molecular mobility. MRI images and 1-D projections were recorded in the presence of a reference capillary to normalize the signal intensities. The volume-averaged T_1 relaxation times, determined by analyzing the 1-D signal intensity as

a function of TR (eq. 4.10), are approximately the same for all polymer specimens (about 1.2 s). Consequently, its value is not further discussed.

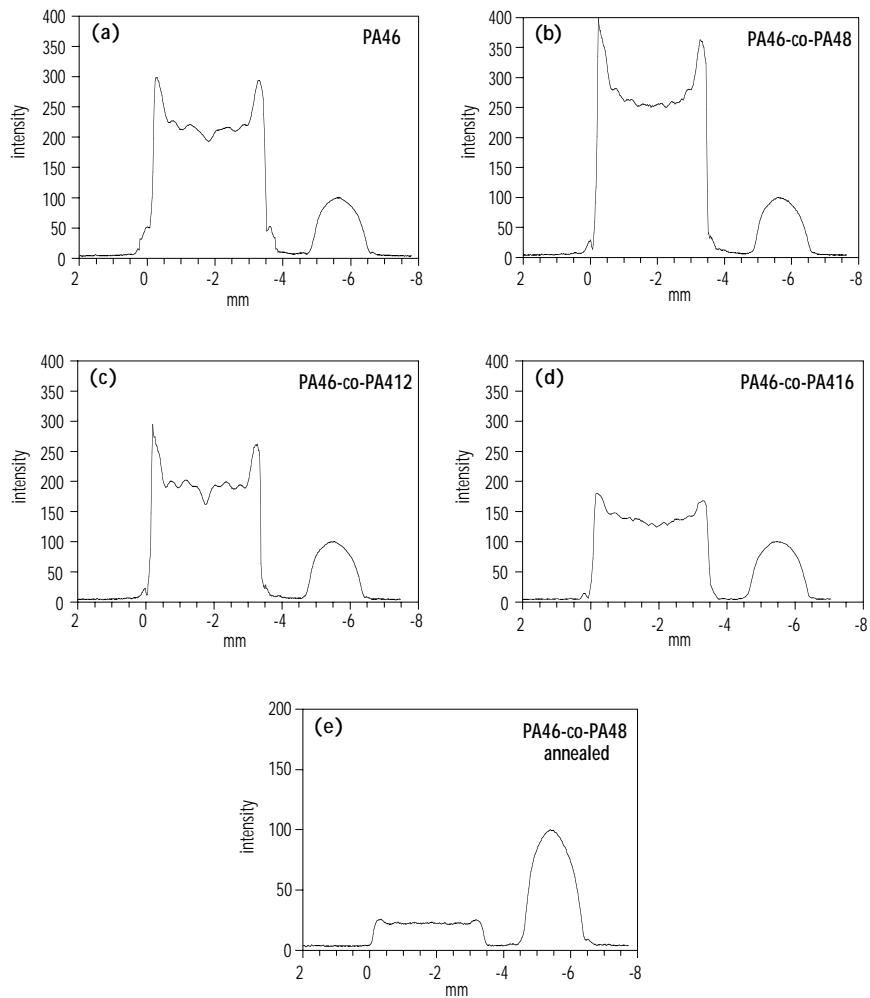


Figure 4.15: 1-D projections of the images ($TE = 1.3$ ms) of water saturated (a) PA46 and PA46-co-PA4n plates: (b) $n = 8$, (c) $n = 12$, (d) $n = 16$ and (e) for $n = 8$ after annealing. The signal of doped water in the reference capillary is shown on the right side of the projections.

Although the plates are saturated to equilibrium, the MRI images (not shown) and reconstructed 1-D projections (Figure 4.15a-d) also reveal a horn shaped intensity projection with a gradual decrease of the signal intensity

Chapter 4

towards the center of the plate. Table 4.14 presents the volume-averaged (determined over the total width of the 1-D projection) and the spatially resolved (determined in the horn and in the core part for a width of 0.3 mm) spin density values (M_0) and T_2 decay times (eq. 4.8), being proportional to the amount of water and the molecular mobility of water molecules, respectively.

Table 4.14: MRI relaxometry results for water saturated PA46 and PA46-co-PA4n plates.^a

	n = 6 (PA46)	n = 8	n = 12	n = 16
$\langle T_2 \rangle$ (ms) ^b	2.8	3.1	2.2	1.9
$\langle M_0 \rangle$ ^c	92	100	87	77
T_2 horn (ms) ^b	3.2	3.6	2.4	2.0
M_0 horn ^c	78	100	73	46
T_2 core (ms) ^b	2.5	2.7	2.0	1.8
M_0 core ^c	87	100	79	55
T_2 horn/core	1.28	1.33	1.20	1.11
M_0 horn/core	0.90	1	0.92	0.84

^a Errors indicate the 95 % confidence interval of the non-linear least squares fits and the average values are 0.1 ms for the T_2 relaxation times and 2-3 % for the M_0 values.

^b $\langle T_2 \rangle$ represents the volume-averaged T_2 decay time, while T_2 horn and T_2 core are determined in a layer of 0.3 mm thickness at the surface and in the middle part of the plates, respectively.

^c Spin density values (M_0) are all normalized to 100 for the copolymer PA46-co-PA48.

Both the volume-averaged water molecular mobility and water concentration of PA46 are lower than those of the copolymer with $n = 8$. But within the copolymer series, both parameters clearly decrease with increasing chain length of the comonomer. The volume-averaged M_0 values correlate well with the amount of water uptake as determined by gravimetry. The spatially dependent M_0 and T_2 values demonstrate a similar behavior. Comparing the projections for the copolymers (Figure 4.15b-d), the overall signal intensity decreases with increasing chain length of the comonomer and the differentiation between horns and core becomes less pronounced. This is also demonstrated by the decrease in the relative intensity ratios between horn and core in the different copolymers (Table 4.14). It appears that in the copolymer with $n = 16$,

the water molecular mobility is quasi spatially independent as can be concluded from the rather comparable T_2 values in the horn and core part.

Annealing the polyamide plates results in a large decrease of the MRI signal as shown in Figure 4.15e. The profile of the projection is no longer horn shaped but becomes almost rectangular. The volume-averaged T_2 relaxation time of the annealed polyamides is strongly reduced to about 0.64 ms. Because of the very low MRI signal intensity, a comparison between the different copolymers was not performed.

MRI relaxation results as a function of temperature are presented in Table 4.15 for PA46. With increasing temperature, a slight increase in the molecular mobility of the absorbed water molecules is observed. However, this only seems to be the case for the water molecules at the outer part of the plates. The T_2 values measured at the inner core seem to be more or less independent on temperature. Again, this points out that the water molecules in the inner core are more strongly bound as compared to those at the outer layer of the plates.

Table 4.15: MRI relaxometry results for water saturated PA46 as a function of temperature.^a

	T = 30 °C	T = 50 °C	T = 70 °C
$\langle T_2 \rangle$ (ms) ^b	2.4	2.8	2.9
T_2 horn (ms) ^b	2.6	3.2	3.7
T_2 core (ms) ^b	2.2	2.5	2.3
T_2 horn/core	1.18	1.28	1.61

^a Errors indicate the 95 % confidence interval of the non-linear least squares fits and an average value of 0.1 ms is obtained for the T_2 relaxation times.

^b $\langle T_2 \rangle$ represents the volume-averaged T_2 decay time, while T_2 horn and T_2 core are determined in a layer of 0.3 mm thickness at the surface and in the middle part of the plates, respectively.

4.4.6. Discussion with regard to the different physico-chemical parameters that determine the water uptake in PA46-co-PA4n copolymers

The results presented above (section 4.4.2. to 4.4.5.) concerning the water uptake of a series of PA46 copolymers cannot be explained by a single molecular parameter. A combined approach, based on several physico-chemical parameters which all have their influence on the water uptake, is necessary.

4.4.6.1. Influence of the hydrophobicity and the amount of crystallinity

It has already been established in literature that an increase in the molar ratio $[\text{CH}_2]/[\text{amide}]$ results in a decrease of the equilibrium water uptake of polyamides.⁶⁵ Figure 4.16 shows this hydrophobic effect for different homopolymers PA x_n with x and n being even numbers⁶⁶ and for the three copolyamides PA46-co-PA4 n . Although the amide concentration has been reduced as compared to PA46, the copolymer PA46-co-PA48 absorbs more water than PA46. Moreover, the slope in Figure 4.16 for the three copolyamides is surprisingly much steeper compared to that of the homopolyamides PA x_n .

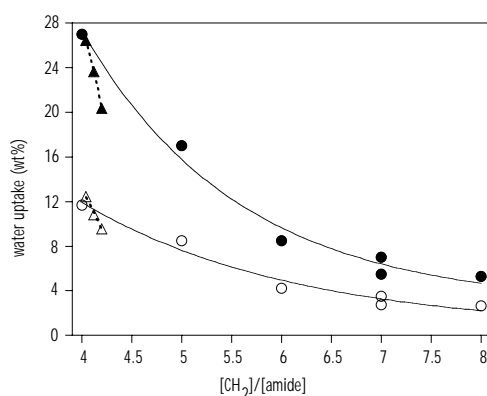


Figure 4.16: Equilibrium water uptake (wt%) of even-even homopolyamides PA x_n (○,●) and of the copolyamides PA46-co-PA4 n (△,▲). Open symbols represent the experimental equilibrium water uptake; filled symbols represent the calculated equilibrium water uptake of the amorphous phase.

Since water is only absorbed by the amorphous phase,¹⁵ differences in crystallinity between the polyamides might also effect the water uptake. This effect is not accounted for in the curve of the open symbols in Figure 4.16. The crystallinity of PA46 is known to be substantially higher than that of homopolyamides with higher $[\text{CH}_2]/[\text{amide}]$ ratios. The water uptake in the amorphous phase of PA46 and the copolyamides can be calculated by using the data of Table 4.13 and assuming that $\%T_{2,s}$ represents the fraction of the crystalline phase. In case a crystallinity of 50 % is presumed for the other PA x_n polyamides,⁶⁷ the curve represented by the filled symbols in Figure 4.16 is obtained. The water uptake in the amorphous phase seems to be reduced for all copolyamides as compared to PA46, even for the copolymer PA46-co-PA48. However, the difference in slope between the homopolyamides and the copolyamides still remains present.

So the hydrophobicity effect and the amount of crystallinity do not completely explain the water uptake in the PA46-co-PA n copolymers. This means that some additional molecular parameters, effecting the water uptake, have to be considered.

4.4.6.2. Annealing

The annealing experiments also offer important information on the water absorption of the PA46 copolymers. Annealing results in a strong decrease of the amount and the molecular mobility of the absorbed water molecules. Since it is known that water is only absorbed by the amorphous phase¹⁵ and that annealing does not effect the amount of crystallinity significantly,¹⁰ the observed decrease has to be the result of a closer coupling of the amide groups in the amorphous phase due to annealing. This will result in an increased density of the amorphous phase as already demonstrated for regular PA46.⁶⁸

This densifying effect is especially pronounced for the homopolymer PA46 where a 3.1 fold reduction of the moisture uptake is observed upon annealing. This can be explained by the highly symmetrical chain structure of PA46. For the copolyamides PA46-co-PA n , only a 2.5 fold reduction in water uptake is observed: the comonomer units obstruct the regular hydrogen bond formation and consequently reduce the ability for closer couplings upon annealing. The strong reduction of the volume-averaged T_2 decay time of the annealed

polyamides, confirms that not only the amount of amorphous phase but mainly the polymer chain arrangement (density) in the amorphous phase determines the amount, ingress rate and molecular mobility of the absorbed water molecules. These results already demonstrate the importance of the density of the amorphous phase for the water uptake by polyamides.

The following two items will handle with physico-chemical parameters that strongly determine the coupling between the amide groups in the amorphous phase, in order to explain the difference in slope between the homopolyamides and copolyamides in Figure 4.16.

4.4.6.3. Crystallization rate and temperature-time history

The high crystallization rate of PA46 compared to other polyamides lays in its high symmetry and low $[\text{CH}_2]/[\text{amide}]$ ratio.⁶⁶ Since crystallites hinder translational mobility in the amorphous phase, we already suggested for PA46 that the fast cooling (from the melt) of the outer layer in the mould (thermal gradient) results in a more kinetically controlled morphology of the amorphous phase. This hampers the hydrogen bond formation between adjacent chains, resulting in a gradual increase of the mean distance between the amide groups in the amorphous phase towards the surface of the plates.⁶⁸ This gradual decrease in the density of the amorphous phase towards the surface, results in a gradual increase in the amount of water uptake and of the mobility of the water molecules toward the surface of the plates. This is expressed by the horn shaped water distribution profiles in the 1-D MRI projections of water saturated PA46-based polyamide plates as shown in Figure 4.15.

The decrease in ΔT ($= T_m - T_c$) with increase of n for the three copolyamides (Table 4.9), suggests that the crystallization rate is increasing with increasing n . This was expected to lead to a more pronounced horn shaped water distribution profile for PA46-co-PA416. Surprisingly a decreasing ratio (M_0 horn)/(M_0 core) is found for the copolyamides with increasing n . This means that the degree of coupling of the amide groups is not only determined by T_c (as for PA46) but that a fourth parameter has to be taken into account.

4.4.6.4. Chain mobility of the copolymer segments in PA46-co-PA4n

A possible reason for the increasing value of T_c for the copolyamides with increasing n lies in an enhanced mobility of the PA46 segments in the amorphous phase, linked by the longer aliphatic comonomer units. Thus the comonomer units should be seen as a kind of spacer groups that hinder the hydrogen bond formation between adjacent chains and as a result increase the local chain mobility of the PA46 fragments in the copolymer. This kinetically allows a better chain arrangement, which can result in an improved densification in the amorphous phase. This effect is especially pronounced for the longer comonomer in PA46-co-PA416, elucidating why this copolymer is situated so much below the reference line in Figure 4.16.

This effect will decrease with decreasing length of the aliphatic comonomer and explains why the copolymer PA46-co-PA48, after correction for the hydrophobicity and the amount of amorphous phase, is situated nicely on the curve (filled symbols) in Figure 4.16. By using this assumption, we can explain the decreasing ratio $(M_0 \text{ horn})/(M_0 \text{ core})$ and the decrease in water molecular mobility (ratio $(T_2 \text{ horn})/(T_2 \text{ core})$) with increasing n value and for the larger slope of the copolyamides in Figure 4.16.

4.4.6.5. Dependency of the mobility of water molecules on temperature

As expected, an increase in the molecular mobility of the absorbed water molecules is observed with increasing temperature (Table 4.15). However, this effect is clearly more pronounced for the water molecules at the surface part of the plates as compared to these in the inner core for which the T_2 values seem to be more or less independent on temperature. These observations confirm the gradual decrease in the density of the amorphous phase towards the surface of the PA46 plates.

4.4.7. Conclusion

NMR and MRI relaxometry, DSC and gravimetric experiments are used to study the water absorption by the copolymers PA46-co-PA4n. Gravimetric results show a clear decrease of the amount of water absorbed at equilibrium and of the water ingress rate with increasing n. A similar behavior is observed for the MRI relaxation parameters M_0 and T_2 . The reduction in moisture uptake and water molecular mobility upon annealing proves that the density of the amorphous phase is an important material property with respect to the water uptake.

The hydrophobicity effect explains the decreasing water absorption with increasing n, but the copolymer PA46-co-PA48 absorbs more water than PA46. Taking the amount of crystallinity into account (determined by ^1H wideline NMR), the total water content in the amorphous phase of all copolymers becomes smaller than for PA46. However, the steep slope observed for the copolymers in the hydrophobicity plot, can only be explained by differences in morphology of the amorphous phase (strength of the hydrogen bridge coupling between the amide groups). The long methylene segments in the comonomers lead to an increase of the chain mobility of the PA46 segments in the polymer melt, allowing an improved structuring and closer coupling of the amide groups in the amorphous phase. Since this effect is most pronounced for PA46-co-PA416, the amount of water uptake and the molecular mobility of the absorbed water molecules is reduced the strongest for this copolymer.

These results demonstrate that the modification of PA46 with a hydrophobic comonomer enables the reduction of the water uptake by polyamides in a predictable way.

4.5. General conclusions

Fundamental knowledge about the unexpected high amount of water uptake by PA46 is of considerable interest since the absorbed water reduces the excellent properties of this material and limits its applications. The striking behavior of PA46 with respect to water uptake can be explained by its very high crystallization rate, preventing the close coupling of amide groups in the amorphous phase. This results in a gradual decrease of the density of the amorphous phase towards the outside of the plate, causing a higher water absorption and higher mobility (T_2) of the absorbed water molecules in this direction. During annealing, the coupling of the amide groups improves and the density of the amorphous phase increases, resulting in a substantial decrease of the water uptake and of the mobility of the absorbed water molecules.

PA46-co-PA4n copolymers are prepared by introducing longer dicarboxylic acids during synthesis, in order to reduce the water uptake of the polyamide while retaining the excellent properties of PA46. The hydrophobicity effect explains the decreasing water absorption with increasing length of the hydrophobic alkyl chain. However, also the amount of crystallinity and mainly the chain mobility of the copolymer segments and the morphology of the amorphous phase have to be taken into account to completely clarify the water absorption behavior of these PA46-co-PA4n copolymers.

These results nicely demonstrate that a combination of NMR and MRI relaxometry is the technique to study the water sorption behavior of PA46 and PA46-based copolymers from a molecular point of view. It allows retrieving essential information, not only about the volume-averaged molecular mobility of the material and of the ingressed water molecules, but also about the spatially dependent water concentration and water molecular mobility.

4.6. Experimental part

4.6.1. Materials

Injection moulded PA46 plates (80 × 80 × 2 mm and 80 × 80 × 4 mm) were prepared at a melt and mould temperature of 315 and 120 °C respectively. Plates used for MRI (30 × 10 × 2 mm) and gravimetric analysis (30 × 10 × 2 mm and 30 × 10 × 4 mm) were sawn out of the original plates. Polished 2 mm plates were obtained by removing 1 mm from both sides of an original 4 mm plate (two-sided polished) or 2 mm from one side (one-side polished) by polishing with emery paper P4000 with a grain size of 4 – 5 μm.

Proton CPMG T_2 NMR relaxation experiments were performed on small strips of PA46 (30 × 4 × 2 mm), fixed into a standard 5 mm NMR tube. For proton solid echo wideline NMR relaxation experiments, small pieces of the core part and outer layer (100 and 350 μm) of dry PA46 were packed in a short 5 mm glass tube closed with Teflon stoppers. Deuterium quadrupolar solid echo spectra were acquired by using small pieces of D_2O saturated PA46. These pieces were rinsed with water and dried of excess of water to remove all surface adsorbed D_2O .

For the copolymers PA46-co-PA4n, prepolymers were prepared first according to patent EP 0 254 367 example 1,⁶⁹ by adding the dicarboxylic acid(s) (4.95 mole) to a mixture of diaminobutane (5.04 mole) and water (94.5 g). For the copolymers PA46-co-PA4n, a mixture of adipic acid (4.752 mole) and the corresponding comonomer (0.198 mole) was used. After reaction for 25 minutes at 207 °C in a closed reactor, the content of the reactor was discharged via a spray nozzle into an area with nitrogen at atmospheric pressure. Prepolymer powder was charged into a tumble dryer and heated at 230 °C for 24 hours in an atmosphere containing 25 wt% water and 75 wt% nitrogen, ensuring a slight gas stream to maintain the right ratio between water and nitrogen over the experiment. The polymer powder was fed to a single screw extruder and injected at a temperature of 305 °C into a mould (size 63.5 × 12.7 × 3.4 mm) at 80 °C. Plates with a dimension of 30 × 12.7 × 3.4 mm were sawn out of these plates and used for MRI and gravimetrical experiments. For the proton wideline NMR experiments, rectangular pieces were used, placed in a 9 mm NMR tube.

Annealing of PA46 and PA46-co-PA4n plates was accomplished at 260 °C for 12.5 h (unless otherwise stated) under nitrogen atmosphere.

4.6.2. Gravimetric analysis

The plates were dried at 100 °C for about 14h to constant weight W_0 . Afterwards, they were immersed in distilled water in tubes and kept at a specific temperature in a thermostatically controlled water bath. The swollen samples were removed at specific time intervals, wiped off with tissue paper, quickly weighed (W_i) on an electronic balance with an accuracy of 0.1 mg and replaced into the diffusion tubes. Since the weighing was done within a very short time, the error associated with the evaporation of water is negligible.⁷⁰ The mass percentage water uptake was calculated by means of equation 4.5, while the diffusion coefficient was determined by using equation 4.3 and 4.4. The Arrhenius relation (eq. 4.6) resulted in the diffusion activation energy.

4.6.3. Volume-averaged NMR relaxation experiments

All NMR experiments were performed on an Inova 400 Varian vertical bore spectrometer operating at a static magnetic field of 9.4 T, unless otherwise noted. The CPMG pulse sequence was used to record the T_2 decay times of semi-rigid and mobile molecules. For this purpose, small strips of saturated PA46 (30 × 4 × 2 mm) were fixed into a standard 5 mm NMR tube and spectra were recorded with a spectral width of 200 kHz (5 μ s dwell time).

Deuterium wideline spectra of D₂O saturated polyamides were recorded by means of the quadrupolar echo pulse sequence with a spectral width (sw) of 2 MHz and 40 kHz and a 90° pulse width of 2.4 μ s. The inversion recovery method was used to determine the deuterium proton spin-lattice relaxation times.

Proton solid echo wideline NMR was used to measure the short T_2 decay times of rigid molecules in dry PA46. Solid echo spectra were recorded with a dedicated wideline probe by using the solid echo pulse sequence⁷¹ with an echo delay of 8 μ s and a 90° pulse width of 1.8 μ s. Spectra were acquired with a spectral width of 2 MHz (0.5 μ s dwell time) allowing an accurate determination of the echo maximum. The T_2 values were determined by analyzing the FID to an

Abragam function at room temperature (equation 4.12) and to the sum of a Weibull and exponential function at 170 °C (equation 4.13).⁵² The ^1H T_1 relaxation times were measured by using the inversion recovery solid echo sequence and the results were fit by means of equation 4.9. The non-linear least square analyses of relaxation data were performed on a Macintosh computer by using the program KaleidaGraph 3.0.

The proton wide-line NMR experiments of the PA46 copolymers were performed by Dr. V.M. Litvinov (DSM Research, Geleen) on a Bruker Minispec MQ-20 spectrometer, operating at a proton resonance frequency of 20 MHz. The length of the 90° pulse and the dead time were 2.8 μs and 7 μs , respectively. A BVT-2000 temperature controller was used for temperature regulation. The solid echo pulse sequence⁷¹ was used to record the free induction decay (FID). The T_2 relaxation times were obtained by performing a non-linear least squares fit of the data by using the equations 4.14, 4.13 and 4.16.

4.6.4. Imaging

MRI images were acquired at 9.4 T on an Inova 400 Varian vertical bore spectrometer by using a 16 mm micro-imaging coil. A dedicated Teflon holder was used to immobilize the plate with the longest dimension along the direction of the main magnetic field B_0 (z-direction) as presented in Figure 4.1a.

Standard MRI images of water saturated PA46 plates were obtained (without surrounding water) in the transverse direction (xy-plane) with an echo time (TE) of 7 ms and a repetition time (TR) of 3.5 s. By using this long TE, only protons from the absorbed water ($T_{2,1} = 4$ ms) were mapped since protons belonging to the polymer matrix have a shorter transverse relaxation time ($T_{2,s} = 1.1$ ms) and were not observed under these experimental conditions. The images had an in-plane pixel resolution of about 60 \times 60 μm , a field of view (FOV) of 16 \times 16 mm and a slice thickness of 6 mm. Only the central part of the images, being the area between the two lines A and B as demonstrated in Figure 4.17, was used to reconstruct the one-dimensional (1-D) projections to avoid the unwanted absorption from the other (small) edges.⁴⁷ⁱ

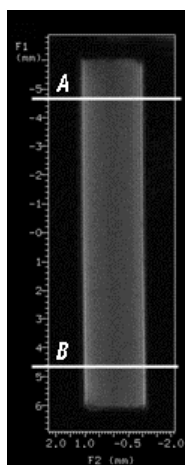


Figure 4.17: MRI image of a water saturated PA46 plate with indication of the area between the two lines A and B, used to reconstruct the 1-D projections.

To study the water diffusion process, images of the PA46 specimen were acquired as a function of time in the presence of surrounding water. The signal from the surrounding water was suppressed by using the inversion recovery (IR) technique, based on differences in the T_1 relaxation times between surrounding and ingressed water.⁷²

Spatially resolved relaxation and concentration values were obtained by acquiring images of a saturated PA46 plate as a function of TE and TR with a FOV of 15×12 mm. All images were recorded without surrounding water because suppression of the surrounding solvent by the IR technique will also suppress the ingressed water partially. For the TE series, TR was fixed to 3.5 s while TE was varied between 1.7 and 11 ms in steps of 0.5 ms. For the TR series, TE was fixed to 1.7 ms and TR was varied between 0.05 and 5 s (21 values). The spatially resolved values of M_0 (spin density), T_2 and T_1 were calculated from reconstructed 1-D projections (central part between the two lines A and B in Figure 4.17b) for consecutive slices of 0.2 mm from the core towards the outer part of the plate (Figure 4.18). The signal intensity was analyzed as a function of TE by using equation 4.11 (bi-exponential) or equation 4.8 (mono-exponential) to obtain M_0 and T_2 and as a function of TR by means of equation 4.10, resulting in the T_1 relaxation time.

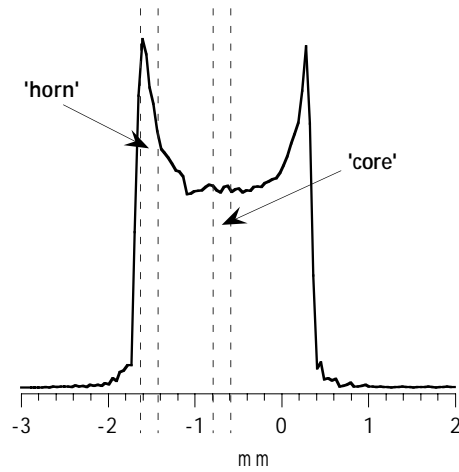


Figure 4.18: Reconstructed 1-D projection of a water saturated PA46 plate with indication of the regions used for the determination of the spatially resolved relaxation parameters.

Intensity calibrated MRI images were obtained on water saturated plates without surrounding water. They were calibrated by means of a reference capillary, filled with a 0.2 % CuCl_2 solution in $\text{H}_2\text{O}/\text{D}_2\text{O}$: 1/8 ($\text{pH} = 4.5$) having a T_1 decay time of only 0.1 s. The mixture $\text{H}_2\text{O}/\text{D}_2\text{O}$ was used to avoid too large differences in dynamic range between the water signal of the saturated plates and that of the capillary. Images were recorded with $\text{TR} = 5 \times T_1$ and $\text{TE} = 1.25$ ms and 5 ms. 1-D projections were reconstructed from the central part of the images. Volume-averaged T_1 and T_2 decay times were determined for the same specimen from direct MRI projections (not reconstructed from the images) as a function of TR and TE, respectively. For the TR series, $\text{TE} = 1.25$ ms and TR was varied between 0.1 and 7.5 s. For the TE series, TR equals $5 \times T_1$ and TE was varied between 1.25 and 7 ms.

The quantitative determination of the amount of absorbed water in saturated PA46 plates was accomplished by acquiring MRI projections (6 mm slice thickness) of a set-up of a water saturated PA46 plate and a 5 mm NMR tube (4.2 mm internal diameter) filled with doped water (0.2 % CuCl_2) as a function of TE with $\text{TR} = 5$ s. TE was varied between 3 and 300 ms (between 3 and 10 ms in steps of 0.25 ms, between 10 and 20 ms in steps of 1 ms and between 20 and 300 ms in steps of 10 ms). To avoid any contribution of plasticized PA46 ($T_2 = 1.1$ to 1.2 ms) to the quantitative water spin density, only echo time intensities

starting from TE = 6 ms were used in the analysis. For the tube, on the other hand, echo time intensities starting from 3 ms were used.

For the copolymer series, MRI images and 1-D projections were also recorded in the presence of a reference capillary. The volume-averaged T_1 relaxation times were determined by analyzing the overall signal intensity of the MRI 1-D projections, acquired as a function of the variable TR, by using equation 4.10. TR was varied between 0.1 s and 10 s while TE was fixed to 1.3 ms. The T_2 decay times were determined by acquiring MRI images as a function of TE (TE varied between 1.3 ms and 10 ms) with a fixed TR of 6 s. After reconstructing 1-D projections from the central part of the plate, the T_2 values were determined by analyzing the signal intensity as a function of TE with equation 4.8. In addition to the volume-averaged T_2 decay time $\langle T_2 \rangle$, determined by using the total width of the 1-D projection, also the spatially resolved T_2 relaxation times were determined in the horn and in the core part for a slice width of 0.3 mm.

4.6.5. DSC

The melting enthalpy (ΔH_m) and melting temperature (T_m) were measured on a Perkin-Elmer 7, provided with a thermal analysis controller TAC/DX at a heating rate of 10 °C/min under nitrogen atmosphere. For the copolymers PA46-co-PA4n, the crystallization temperature T_c was determined at sample cooling from 330 °C.

4.6.6. WAXS and density measurements

WAXS (wide angle X-ray scattering) diffractograms were recorded at DSM Geleen by using a Philips PX 1820 diffractometer system to determine the level of crystallinity and the density of the crystalline phase (ρ_c). The overall density was determined by means of a density gradient column (DSM Geleen).

4.7. Appendix

4.7.1. Water absorption data (Table 4.2)

PA6: *Water uptake: wt% = 9.5 % and 60 % crystallinity*

This means:	9.5 % H ₂ O	in	40 % amorphous phase
	↓ $M = 18 \text{ g/mole}$		↓ $M = 113 \text{ g/mole} = \text{molar mass of}$ <i>the PA6 repeating unit</i>
or:	0.528 mole H ₂ O	in	0.354 mole amorphous phase
			↓ <i>1 mole amide per mole repeating</i> <i>unit in the amorphous phase of PA6</i>
or:	2.98 mole H₂O	per	2 mole amide groups in the amorphous phase

PA66: *Water uptake: wt% = 8.6 % and 50 % crystallinity*

This means:	8.6 % H ₂ O	in	50 % amorphous phase
	↓ $M = 18 \text{ g/mole}$		↓ $M = 230 \text{ g/mole} = \text{molar mass of}$ <i>the PA66 repeating unit</i>
or:	0.478 mole H ₂ O	in	0.217 mole amorphous phase
			↓ <i>2 mole amides per mole repeating</i> <i>unit in the amorphous phase of PA66</i>
or:	2.20 mole H₂O	per	2 mole amide groups in the amorphous phase

PA46: Since it is assumed that the amide groups in PA46 have the same affinity to water molecules as in PA6 and PA66, the number of moles H₂O per 2 mole amide groups in the amorphous phase of PA46 is calculated as the average value for PA6 and PA66:

$(2.98 + 2.20)/2 = 2.59 \text{ mole H}_2\text{O per 2 mole amide groups in the amorphous phase}$

This means:	2.59 mole H ₂ O	per	2 mole amide groups in the amorphous phase
	↓ <i>M = 18 g/mole</i>		↓ <i>2 mole amides per mole repeating unit in the amorphous phase of PA46 and the molar mass of the PA46 repeating unit = M = 198 g/mole</i>
or:	46.62 g H ₂ O	in	198 g amorphous phase
			↓ <i>70 % crystallinity</i>
or:	7.1 % H₂O is expected	in	30 % amorphous phase
Measured:	12.4 % H ₂ O	in	30 % amorphous phase
	↓ <i>M = 18 g/mole</i>		↓ <i>M = 198 g/mole = molar mass of the PA46 repeating unit</i>
or:	0.689 mole H ₂ O	in	0.152 mole amorphous phase
			↓ <i>2 mole amides per mole repeating unit in the amorphous phase of PA46</i>
or:	4.53 mole H₂O	per	2 mole amide groups in the amorphous phase

4.7.2. Deuterium NMR relaxation experiments (section 4.3.2.3.)

13.6 % D ₂ O	in	30 % amorphous phase of PA46	
↓ <i>M = 20 g/mole</i>		↓ <i>M = 200 g/mole = molar mass of the deuterated PA46 repeating unit</i>	
or:	0.68 mole D ₂ O	in	
		0.15 mole amorphous phase	
		↓ <i>2 mole amides per mole repeating unit in the amorphous phase of PA46</i>	
or:	2.27 mole D ₂ O	per	mole N-D in the amorphous phase
or:	a deuterium signal intensity of 4.5 mole D (from D₂O)	per	mole D (from the amide groups in the amorphous phase)

4.7.3. Intensity calibrated MRI projections (section 4.3.3.5.)

For a native PA46 plate and by using equation 4.8:

TE = 5 ms:

core: $M_t = 85 \times \exp(-5/3.5)$
= 20.37

*intensity of the core is
⇓ referred to the intensity
of the projection*

intensity = 56 in the projection

horn: $M_t = 100 \times \exp(-5/4.5)$
= 32.92

*idem conversion as
⇓ for the core*

intensity = 90.5 (calculated)
**this corresponds nicely to the
intensity in the projection, so with
this long TE, only water is observed**

TE = 1.25 ms:

core: $M_t = 85 \times \exp(-1.25/3.5)$
= 59.47

*intensity of the core is
referred to the intensity
⇓ of the projection because
no plasticized matrix is
observed in the core*

intensity = 178 in the projection

horn: $M_t = 100 \times \exp(-1.25/4.5)$
= 75.75

*idem conversion as
⇓ for the core*

intensity = 226.7 (calculated)
**a larger intensity of 260 is observed
in the projection, indicating that in
the horn also a fraction of the
plasticized PA46 matrix is observed**

4.8. References

1. Schouten, A.E.; van der Vegt, A.K. *'Plastics'*, Delta Press BV, Overberg, 1987.
2. Young, R.J.; Lovell, P.A. *'Introduction to Polymers'*, Chapman and Hall, London, 1991.
3. Carothers, W. to Arthur P. Tanberg in *'Early History of Polyamide Fibers'*, 19 February 1936, Hagley Museum and Library Collection.
4. Cowie, J.M.G. *'Polymers: Chemistry and Physics of Modern Materials'*, Blackie Academic and Professional, Glasgow, 1991.
5. Birley, A.W.; Heath, R.J.; Scott, M.J. *'Plastic Materials: Properties and Applications'*, Blackie, Glasgow, 1988.
6. Elias, H.G. *'An introduction to plastics'*, VCH Verlagsgesellschaft mbH, Weinheim, 1993.
7. W. H. Carothers U.S. Patent 2, 130, 948, **1938**.
8. Gaymans, R.J.; Van Utteren, T.E.; Van Den Berg, J.W.A.; Schuyer, J. *J. Polym. Sci., Polym. Chem. Edn.* **1977**, *15*, 537.
9. Patwardhan, D.V. in *'Polymer Data Handbook'*, Ed. by J.E. Mark, Oxford University Press, 1999.
10. Eltink, S.; de Boer, S.; Moonen, J. *'Crystallinity studies on polyamides'*, Internal publication, DSM Research, The Netherlands, 1992.
11. a) Roerdink, E.; Warnier, J.M.M. *Polymer* **1985**, *26*, 1582. b) Creemers, H. *Engineering Plastics* **1989**, *11*, 19. c) Steeman, P.A.M.; Maurer, F.H.J. *Polymer* **1992**, *33*, 4236. d) Kudo, K.; Mochizuki, M.; Kiriya, S.; Watanabe, M.; Hiram, M. *J. Appl. Polym. Sci.* **1994**, *52*, 861. e) Suzuki, A.; Endo, A.; Kunugi, T. *J. Polym. Sci. B: Polym. Phys.* **1998**, *36*, 2737. f) Bermudez, M.; Leon, S.; Aleman, C.; Munoz-Guerra, S. *J. Polym. Sci. B: Polym. Phys.* **2000**, *38*, 41.
12. a) Kawasaki, K.; Sekita, Y. *J. Polym. Sci. A* **1964**, *2*, 2437. b) Huang, P.T.; Lee, J.L.; Chiu, S.C.; Kwei, T.K.; Pearce, E.M. *J. Appl. Polym. Sci.* **1999**, *73*, 295.
13. Dlubek, G.; Stolp, M.; Nagel, C.; Fretwell, H.M.; Alam, M.A.; Rausch, H.J. *J. Phys.: Condens. Matter* **1998**, *10*, 10443.
14. a) Rault, J.; Le Huy, H.M. *J. Macromol. Sci. Phys.* **1996**, *B35*, 89. b) Ginénez, V.; Mantecón, A.; Cádiz, V. *Acta Polymer.* **1998**, *49*, 502.
15. a) Murthy, N.S.; Stamm, M.; Sibilía, J.P.; Krimm, S. *Macromolecules* **1989**, *22*, 1261. b) Hirschinger, J.; Miura, H.; Gardner, K.H.; English, A.D. *Macromolecules*, **1990**, *23*, 2153. c) Pleštil, J.; Baldrian, J.; Ostanovich, Y.M.; Bezzabotnov, V.Y. *J. Polym. Sci. B: Polym. Phys.* **1991**, *29*, 509. d) Hanspach, J.; Pinno, F. *Acta Polymer.* **1992**, *43*, 210.